



MAR -7 2001

Final Technical Report

**CHARACTERIZATION OF INERT GAS PLASMA
THRUSTERS**

DISTRIBUTION STATEMENT A
Approved for Public Release
Distribution Unlimited

Prepared by:

Professor Mark A. Cappelli, Principal Investigator
Mechanical Engineering Department
Stanford University
Stanford, California 94305-3032
Tel: (650) 725-2020, Fax: (650) 723-1748, email: cap@leland.stanford.edu

Prepared for:

Dr. Mitat Birkan
AFOSR
Directorate of Aerospace and Materials Science
Space Power and propulsion Branch
801 North Randolph St. Rm. 732
Arlington, VA 22203-1977

20010329 059

Under AFOSR Grant No: F49620-98-1-0011-P00004

Mechanical Engineering Department
Stanford University
Stanford, California 94305

REPORT DOCUMENTATION PAGE

AFRL-SR-BL-TR-01-

Public reporting burden for this collection of information is estimated to average 1 hour per response, including the gathering and maintaining the data needed, and completing and reviewing the collection of information. Send comments regarding this burden estimate or any other aspect of this collection of information, including suggestions for reducing this burden, to Washington Headquarters Services, Directorate for Information Operations and Reports, 1215 Jefferson Davis Highway, Suite 1204, Arlington, VA 22202-4302, and to the Office of Management and Budget, Paperwork Project (0704-0188).

yes,
this
son

0200

1. AGENCY USE ONLY (Leave Blank)		2. REPORT DATE March 2, 2001		3. REPORT TYPE AND DATES COVERED Annual Technical Report 10/1/97-9/30/00	
4. TITLE AND SUBTITLE Characterization of Inert Gas Plasma Thrusters				5. FUNDING NUMBERS G - F49620-98-1-0011-P0004	
6. AUTHORS Mark Cappelli					
7. PERFORMING ORGANIZATION NAME(S) AND ADDRESS(ES) Stanford University Mechanical Engineering Department Stanford, CA 94305-3032				8. PERFORMING ORGANIZATION REPORT NUMBER	
9. SPONSORING / MONITORING AGENCY NAME(S) AND ADDRESS(ES) AFOSR/PKC 110 Duncan Ave., Room B115 Bolling AFB, DC 20332-8080				10. SPONSORING / MONITORING AGENCY REPORT NUMBER	
11. SUPPLEMENTARY NOTES					
12a. DISTRIBUTION / AVAILABILITY STATEMENT Approved for public release; distribution is unlimited				12b. DISTRIBUTION CODE	
13. ABSTRACT (Maximum 200 words)				<p>AIR FORCE OFFICE OF SCIENTIFIC RESEARCH (AFOSR) NOTICE OF TRANSMITTAL DTIC. THIS TECHNICAL REPORT HAS BEEN REVIEWED AND IS APPROVED FOR PUBLIC RELEASE LAW AFR 100-12. DISTRIBUTION IS UNLIMITED.</p>	
14. SUBJECT TERMS				15. NUMBER OF PAGES 14	
				16. PRICE CODE	
17. SECURITY CLASSIFICATION OF REPORT Unclassified	18. SECURITY CLASSIFICATION OF THIS PAGE Unclassified	19. SECURITY CLASSIFICATION OF ABSTRACT Unclassified	20. LIMITATION OF ABSTRACT UL		

NSN 7540-01-280-5500

Standard Form 298 (Rev. 2-89)
Prescribed by ANSI Std. Z39-1
298-102

Final Technical Report

CHARACTERIZATION OF INERT GAS PLASMA THRUSTERS

Prepared by:

Professor Mark A. Cappelli, Principal Investigator
Mechanical Engineering Department
Stanford University
Stanford, California 94305-3032
Tel: (650) 725-2020, Fax: (650) 723-1748, email: cap@leland.stanford.edu

Prepared for:

Dr. Mitat Birkan

Under AFOSR Grant No: F49620-98-1-0011-P00004

Final Technical Report
CHARACTERIZATION OF INERT GAS PLASMA THRUSTERS
Grant No: F49620-98-1-0011-P00004
Mark A. Cappelli
Mechanical Engineering Department
Stanford University
Stanford, California 94305-3032
Tel: (650) 725-2020, Fax: (650) 723-1748, email: cap@leland.stanford.edu

Executive Summary

Motivation The efficiency of modern Hall thrusters is impacted by the ability to maintain a high ratio of the ion to electron current density, J_i/J_e , at the exit of the acceleration channel. In principal, there is no limit to this ratio, since the electrons that are necessary to maintain the current balance at the anode can be generated within the ionization zone upstream of the channel exit. However, in practice, this metric of performance in a typical Hall thruster can range from ~ 1 -10. This is in part due to the loss of electrons and ions through recombination reactions on the channel wall, and also due to the anomalous migration of electrons from the exit plane through the region of strong magnetic fields. It is believed that this poor confinement of electrons is in part due to turbulent fluctuations in plasma properties, which give rise Bohm-like electron transport in a direction orthogonal to the applied magnetic field. The Stanford Research was aimed at understanding this transport, and any affects that wall scattering may have on also enhancing electron current flow within the discharge channel. The broader long-term objective is to develop passive and/or active control strategies to enhance or suppress electron flow in regions of the channel where such actuation is desirable. Feedback - controlled actuation methods to reduce plasma fluctuations where only marginally successful back in the mid 70's in early versions of Hall thrusters [1,2]. Using modern diagnostic and characterization strategies to obtain an improved understanding of the role that fluctuations and wall scattering plays in electron transport, it is anticipated that we can design more effective control and actuation strategies. Such strategies will require, however, the development of robust models for electron flow, and the incorporation of such models into simulators that are able to accurately capture thruster response.

Accomplishments The research funded under this grant has been extremely successful, and over the course of the two years and four months of funding, has led to 12 archival publications, 24 conference publications or abstracts, and 2 invention disclosures. Here we provide a brief description of the results, and direct the reader to the extensive publication list, where the findings are described in considerable detail. In some cases, papers are provided as attachments in the Appendix.

Using extensive measurements of the time-averaged plasma properties in the discharge channel, including laser-induced fluorescence measurements of neutral and ionized xenon velocities [3, see also Publications 8, 12, 18, and 21, and Appendix I] and various electrostatic probe diagnostics [4, see also Publications 7, 12, 15, 16, 23, 26, 31, 32, and Appendix II] we were able to determine the effective Hall parameter, $(\omega_{ce}\tau)_{\text{eff}}$, the inverse of which is a measure of the crossed-field electron mobility, when the electron cyclotron frequency is much greater than the electron collision frequency. These values are then compared to the classical (collision-driven) Hall parameters expected for a quiescent, magnetized plasma (see Fig. 1). The results indicate that in the vicinity of

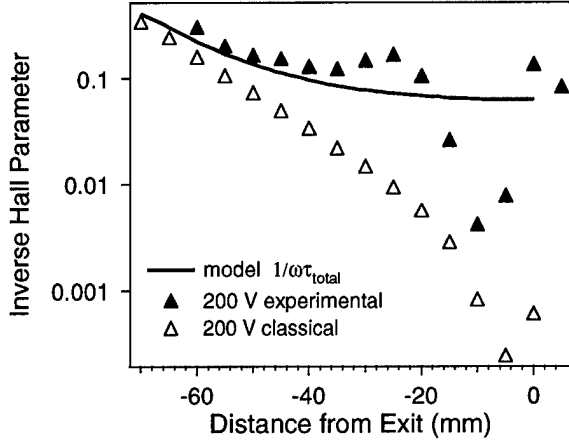


FIG. 1. Comparison of additive collision frequency model to experimental and classical inverse Hall parameter profiles at various axial locations within the discharge channel. The exit plane is at an axial location of $x = 0$ mm, and the anode is at $x = -80$ mm

the anode, where there are fewer plasma instabilities, the electron transport mechanism is found to be in agreement with a “classical” model based on elastic electron collisions with the background neutral xenon. However, we find that in the vicinity of the discharge channel exit, where the magnetic field is the strongest and where there are intense fluctuations in the plasma properties, the inferred Hall parameter departs from the classical value. Instead, it is found to be closer to the Bohm value of $(\omega_{ce}\tau)_{\text{eff}} \approx 16$ [5]. These results provided the first direct support for a simple model for the Hall parameter (and hence electron mobility or conductivity) that is based on the scalar addition of the electron collision frequencies; a model that was proposed by Boeuf and Garrigues [6]:

$$\left(\frac{1}{\omega_{ce}\tau}\right)_{\text{total}} = \left(\frac{1}{\omega_{ce}\tau}\right)_{\text{collisions}} + \left(\frac{1}{\omega_{ce}\tau}\right)_{\text{oscillations}} \quad (1)$$

The solid line in Fig. 1. is the result of this model, where the effects of wall scattering is neglected, and where the contribution to the total inverse Hall parameter due to fluctuations is modeled simply as $1/16$ in accordance with the Bohm theory [5]. While the exact mechanism for this anomalous electron mobility is still the subject of intense research, the results that we have obtained recently, draw attention to the possible role that fluctuations have on enhancing electron transport in regions where the electrons are highly magnetized. The compelling evidence for the relationship between plasma fluctuations and anomalous electron transport is the correlation between the axial location of this enhanced transport, and the location where intense plasma density fluctuations are seen to occur. Using Langmuir probes (operating in saturated ion-collection mode) inserted into the plasma channel to map out time dependent plasma density fluctuations at frequencies $f < 400$ kHz, we have

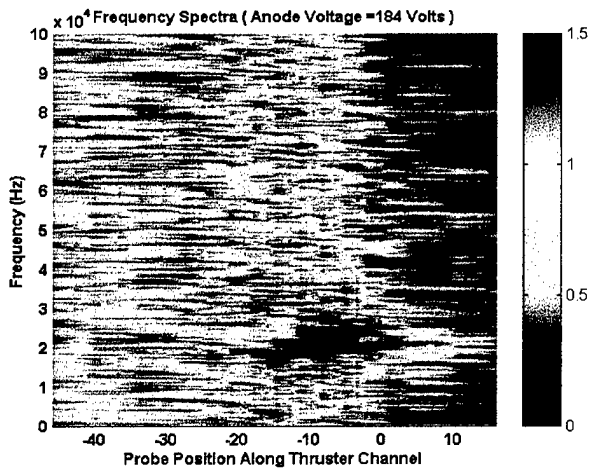


Fig. 2. Spectral map of plasma density fluctuations in the channel of a Hall thruster. The maximum color scale represents fluctuations in density that are comparable to the mean value.

extensively characterized the dynamical behavior of plasma density within the discharge channel [7, see also Publications 3, 11, 13, 14, 25, 29, 33, and Appendix III]. An example of a spectral map (frequency-position) depicting the local fluctuations in plasma density within the discharge channel is shown in Fig. 2.

A comparison (conditional cross-spectral analysis) of the signal from two Langmuir probes, located at the same axial position, but separated by some angle on the azimuth, was used to measure the azimuthal component of the phase velocity (wave dispersion). Fig. 3 shows a typical dispersion plot, rich in features, clearly showing the presence of four characteristic

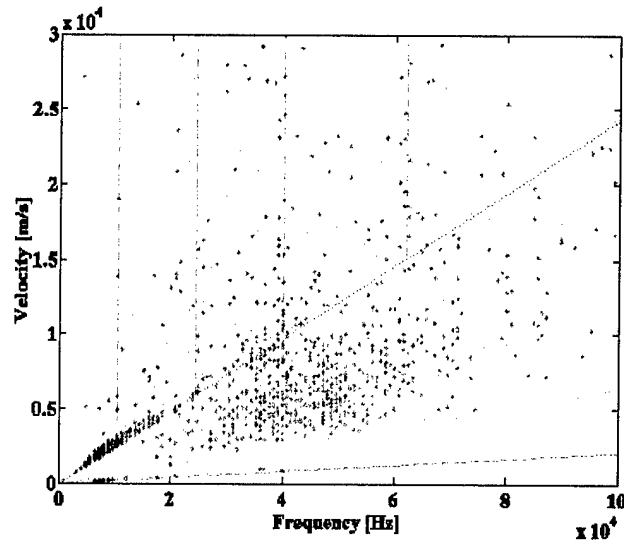


FIG. 3. Wave dispersion plots obtained from two azimuthal probes separated by 30° , for low discharge voltage conditions (100 V), and at $x = 0$ mm. The lines shown are the expected theoretical dispersion lines for azimuthal waves with mode numbers: an apparent $m = 0$ mode (vertical dot-dashed lines), $m = 1$ (dotted line), $m = 4$ (solid line), and $m = 12$ (dashed line) modes.

placement of the probes within the discharge annulus (30° separation results in a wavelength of $1/12^{\text{th}}$ the channel circumference). Finally, the fourth mode identified by the solid ($m=4$) line appears actually as a lower velocity limit to the high frequency disturbances. The appearance of this demarcation is attributed to an interaction between the axial disturbances and the four-fold azimuthal asymmetry imposed by the four equally spaced magnetic solenoids connected to the outer pole-piece [7]. It is noteworthy that the dispersion characteristics of the disturbances are seen to vary dramatically with changes in operating regimes (e.g., applied voltage), or changes in position within the discharge channel [7].

Under this grant, we have complemented these experimental studies with theoretical work on the excitation and propagation of these disturbances, including the determination of linear growth rates, so as to better understand the physical nature of these azimuthal and axial waves, and the mechanisms responsible for their growth [8, see also Publications 10, 35, and Appendix IV]. Using the extensive experimental data on the time-averaged, spatially varying plasma properties within our discharge, we have performed a theoretical study of the response of this plasma to small (linear) perturbations in its properties. As a starting point for this analysis, we assume a two-dimensional fluid description that includes a simplified equation for the electron energy, and constrain the azimuthal wave-vector such that we excite only the dominant ($m=1$) azimuthal modes. The growth rate and frequencies of predominantly axial and azimuthally propagating plasma disturbances are obtained by numerical solution of the resulting eigenvalue problem under a quasi-uniform plasma condition, along the entire discharge channel. The results identify the persistence of a relatively low frequency instability that is concentrated largely in the vicinity of the exit plane, where the magnetic field is at its maximum value, consistent with experimental observations for relatively low operating voltages ($\sim 100\text{V}$).

The results of a typical calculation are shown in Fig. 4. Here we display the determined frequencies of the unstable wave versus axial position, for various propagation angles. It is apparent

modes, the most prominent of which is that of a pure azimuthally propagating disturbance ($m=1$) with frequencies in the 5-20 kHz range, and of phase velocity $V_p \sim 1000 - 4000$ m/s. The dotted line depicts the expected dispersion for a pure azimuthal mode and a 15° tilt angle with respect to the azimuthal plane, consistent with the observation of "ionization spokes" seen in earlier Hall discharge devices [8]. A second mode is that associated with axial disturbances at higher frequencies, the strongest of which are identified on the figure by superimposing dashed-dot vertical lines. The third mode that is identifiable in Fig. 2. is that of an $m = 12$ azimuthal wave (guided by the theoretical dashed line), which has a wavelength equal to that of the separation between the two probes, and is believed to be activated by the

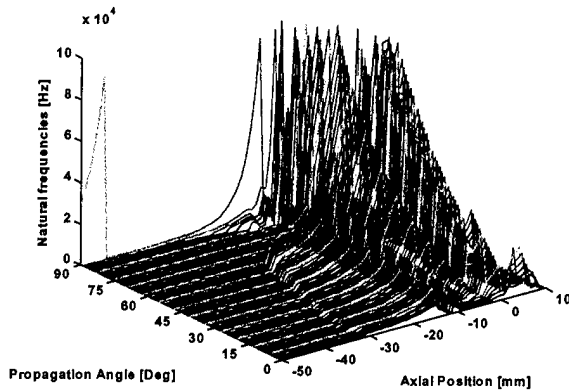


FIG. 4. Predicted frequencies for unstable (exponentially growing) disturbances along the discharge channel, for various propagation angles. The background plasma conditions are those measured for 100V discharge operation.

indicate that the disturbances at low discharge voltages are ionization waves, influenced in part by the spatial variation in other plasma properties (e.g., magnetic field, ion velocity). The development of an analytical model for these low frequency disturbances, and an extension of the numerical simulations to better understand the dynamical behavior of these discharges at high operating voltages is presently underway.

Finally, it has been an objective of this program, to understand the physics of these devices, so as to be able to scale the thrusters down to very low power levels. The operation of $E \times B$ discharge accelerators at these low power ranges introduce many engineering challenges. These include increased heat loads imposed on the structure due to the nature of the scaling of these plasma devices, and the increased frequency (possibly into the MHz regime, also due to the nature of the

scaling) of the strong "loop" instabilities and its impact on the plasma, and power processing unit, amongst others. At Stanford, we have developed and tested a linear-geometry, open electron drift Hall discharge. The linear geometry makes it feasible to use permanent magnets instead of electromagnets (this is important if micro-fabrication methods are to be introduced). The impetus for a linear geometry was largely the result of the experiments described above on coaxial geometries, which indicate that the drifting electrons may not make a complete revolution around the thruster before traversing the region of strong magnetic fields.

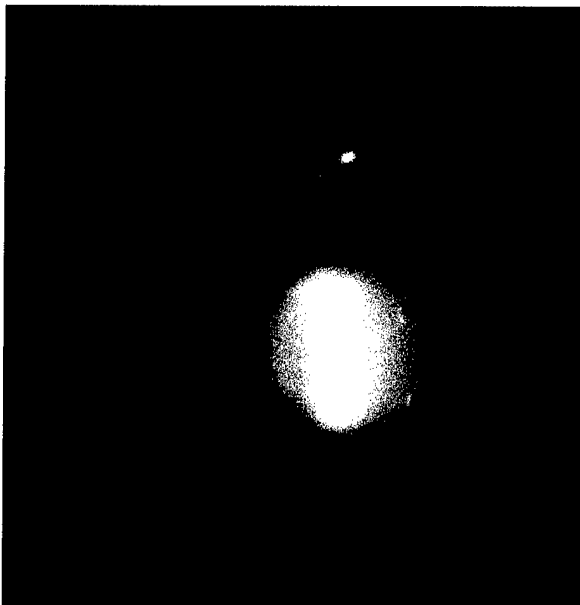


FIG. 5. Photograph of linear thruster operating at about 75W of discharge power.

A photograph of the linear-geometry thruster that we have fabricated and tested while operating at about 75W of power is shown in Fig. 5. Details of the geometry and operating characteristics have been presented in papers (see Publications 6, 17, and Appendix V], although we have not yet

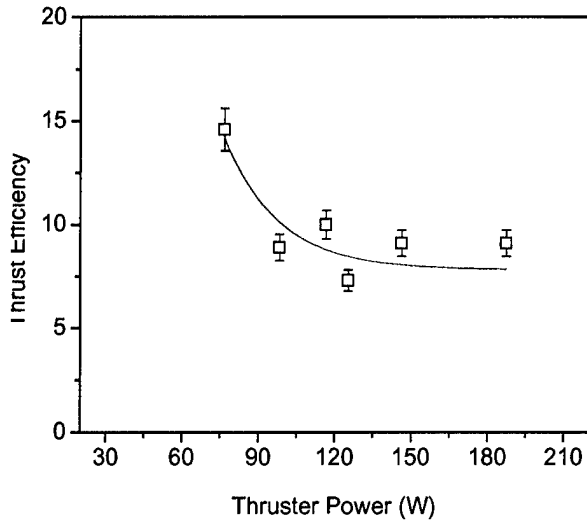


FIG. 6. Thrust efficiency of linear-geometry Hall discharge. Anode mass flow rate varies from 0.2 = 0.4 mg/s of xenon.

published any details on the performance, which is quite encouraging. Using facilities down at Edwards Air Force Base, we were able to characterize the performance of this linear thruster over a wide range of conditions. An example of the measured thrust efficiency is shown in Fig. 6. It is apparent that the thrust efficiency shows a marked increase with decreasing power, unlike the behavior seen in coaxial devices. At the low power operating point, where the efficiency exceeded 14%, the measured specific impulse approached 1100 seconds. As far as we know, no other ultra-low power Hall discharge has performed so well at these conditions, despite the lack of design optimization. In the continuation grant, we propose to further examine the performance of Hall thrusters of radically altered geometries, including co-axial designs without inner magnetic

cores, such as the designs being explored at the Princeton Plasma Physics Laboratory by Fisch, Raites, and colleagues.

References

1. A.I. Morozov, V.A. Nevrovski, and V.A. Smirnov, "Driven Electrostatic Plasma oscillations in a Closed Electron Drift Accelerator," *Sov. Phys. Tech. Phys.*, **18**, 339, 1973.
2. A.I. Morozov, V.A. Nevrovski, and V.A. Smirnov, "Effect of Feedback System on the Plasma Flux in an Accelerator with Closed Electron Drift," *Sov. Phys. Tech. Phys.*, **18**, 344, 1973.
3. W.A. Hargus, Jr., and M.A. Cappelli, "Laser-Induced Fluorescence Measurements in the Interior of a Closed-Electron Drift Hall Discharge," accepted to *Applied Physics B - Lasers and Optics*, 2001.
4. N.B. Meezan, W.A. Hargus, Jr., and M.A. Cappelli, "The Anomalous Electron Mobility in a Coaxial Hall Discharge Plasma," *Phys. Rev. E* **63**, 026410, 2001.
5. D. Bohm in *The Characteristics of Electrical Discharges in Magnetic Fields*, edited by A. Guthrie and R.K. Wakerling, (McGraw, New York, 1949), Chap. 2, p. 65.
6. J. P. Boeuf and L. Garrigues. "Low Frequency Oscillations in a Stationary Plasma Thruster." *J. Appl. Phys.* **84**, 3541, 1998.
7. E. Chesta, C. Lam, N.B. Meezan, D.P. Schmidt, and M.A. Cappelli, A Characterization of Plasma Fluctuations within a Hall Discharge," accepted to *IEEE Transactions on Plasma Science*, 2001.
8. E. Chesta, N.B. Meezan, and M.A. Cappelli, "The Stability of a Magnetized Hall Plasma Discharge," accepted to *Journal of Applied Physics*, 2001.

Acknowledgements

The P.I. would like to express his gratitude to the Air Force for support of this research. The research funded under this grant has contributed directly to the dissertations of W. Hargus, R.

Cedolin, Q. Walker, and N. Meezan, and has included the efforts of many undergraduate and M.S. level students. The views and conclusions contained herein are those of the authors and should not be interpreted as necessarily representing the official policies or endorsements, either expressed or implied, of the Air Force Office of Scientific Research or the U.S. Government.

Publications Arising Directly from this Grant

Archival Publications

1. "Arcjet Nozzle Flowfield Characterization by Laser-Induced Fluorescence," P.V. Storm and M.A. Cappelli, *Applied Optics* **37**, 486-495, 1998.
2. "The Structure of an Expanding Hydrogen Arcjet," W.A. Hargus and M.A. Cappelli, *Phys. Plasmas*, **5**, 4488-4497, 1998.
3. "Coherent Structures in Crossed-Field Closed Drift Hall Plasma Discharges," M.A. Cappelli, W.A. Hargus, Jr., and N.B. Meezan, *IEEE Trans. Plasma Science* **27**, 96-97, 1999.
4. "Raman Scattering Measurements of Molecular Hydrogen in a Low-Density, Arc-heated Plasma," D.R. Beattie and M.A. Cappelli, *Appl. Phys. B* **70**, 419-427, 2000.
5. "Doppler-Free Absorption Measurements of Stark Broadening in a Flowing Hydrogen Plasma," M.A. Cappelli, Q.E. Walker, and P.V. Storm, *JQSRT*, **66**, 343-361, 2000.
6. "A Low-Power, Linear-Geometry Hall Plasma Source with an Open Electron-Drift," D.P. Schmidt, N.B. Meezan, W.A. Hargus, Jr., and M.A. Cappelli, *Plasma Sources Sci. Technol.* **9**, 68-76, 2000.
7. "The Anomalous Electron Mobility in a Coaxial Hall Discharge Plasma," N.B. Meezan, W.A. Hargus, Jr., and M.A. Cappelli, *Phys. Rev. E* **63**, 026410, 2001.
8. "Laser-Induced Fluorescence Measurements in the Interior of a Closed-Electron Drift Hall Discharge," W.A. Hargus, Jr., and M.A. Cappelli, accepted to *Applied Physics B - Lasers and Optics*, 2001.
9. "Laser-Induced Fluorescence Characterization of a Helium Arcjet Flow," Q.E. Walker and M.A. Cappelli, submitted to *Applied Optics*, June 2000.
10. "An Examination of the Stability of a Magnetized Hall Plasma Discharge," E. Chesta, N.B. Meezan, and M.A. Cappelli, accepted to *Journal of Applied Physics*, 2001.
11. "A Characterization of Plasma Fluctuations within a Hall Discharge," E. Chesta, C. Lam, N.B. Meezan, D.P. Schmidt, and M.A. Cappelli, accepted to *IEEE Transactions on Plasma Science*, 2001.
12. "Interior and Exterior Laser-Induced Fluorescence and Plasma Potential Measurements within a Laboratory Hall Discharge," W.A. Hargus, Jr., and M.A. Cappelli, submitted to *Journal of Propulsion and Power*, October 2000.

Conference Papers/Presentations

13. "The Structure and Transient Behavior of Closed-Drift Hall Current Plasma Discharges," M.A. Cappelli, W.A. Hargus, and N.B. Meezan, 51st Annual Gaseous Electronics Conference, American Physical Society, Maui, HI, October 19-22, 1998. See also *Bull. Am. Phys. Soc.* **43**, 1499, 1998.

14. "Oscillatory Behavior in Closed-Drift Hall Plasma Discharges," M.A. Cappelli, N.B. Meezan, W.H. Hargus, Jr., Annual Meeting of the Division of Plasma Physics, American Physical Society, New Orleans, LA, November 16-20, 1998. See also Bull. Am. Phys. Soc. **43** (8), 1936, 1998.
15. "Electron Transport in Hall Thrusters," N.B. Meezan, D.P. Schmidt, W.A. Hargus, Jr., and M.A. Cappelli, NASA/JPL Advanced Rocket Propulsion Research Workshop, Huntsville, AL, April, 1999.
16. "Affecting Electron Transport in a Laboratory Hall Thruster," N.B. Meezan, D. Schmidt, M. A. Cappelli, and W. A. Hargus Jr., AIAA-99-2284, 35th Joint Propulsion Conference, Los Angeles, CA, June 20-24, 1999.
17. "Continued Development of a Linear Hall Thruster," M.A. Cappelli, D. Schmidt, N. B. Meezan, and W.A. Hargus Jr., AIAA-99-2569, 35th Joint Propulsion Conference, Los Angeles, CA, June 20-24, 1999.
18. "Interior and Exterior Laser-Induced Fluorescence Measurements on a Lab Hall Thruster," W. A. Hargus Jr. and M.A. Cappelli, AIAA-99-2721, 35th Joint Propulsion Conference, Los Angeles, CA, June 20-24, 1999.
19. "Characterization of Plasma Disturbances in a Hall Discharge using a Double Probe," D. P. Schmidt, N.B. Meezan, and M. A. Cappelli, AIAA-99-3437, 30th Plasmadynamics and Lasers Conference, AIAA 99-3603, Norfolk, VA, June 28-July 1, 1999.
20. "Laser Induced Fluorescence Measurements of a Helium Arcjet Flow," Q.E. Walker and M.A. Cappelli, AIAA 99-3603, 30th Plasmadynamics and Lasers Conference, Norfolk, VA, June 28-July 1, 1999.
21. "Laser Induced Fluorescence Measurements within a Laboratory Hall Thruster, W.A. Hargus and M.A. Cappelli, AIAA 99-3436, 30th AIAA Plasmadynamics and Lasers Conference, Norfolk, VA, June 28-July 1, 1999.
22. "LIF Measurements of a Low-power Helium Arcjet," Q.E. Walker and M.A. Cappelli, 26th IEEE International Conference on Plasma Science, Monterey, CA, June 20-24, 1999.
23. "Anomalous Transport in Closed and Open-Drift Hall Discharges," Mark Cappelli, Nathan Meezan, and Dan Schmidt, 52nd Annual Gaseous Electronics Conference, American Physical Society, Norfolk, VA, October 5-8, 1999. See also Bull. Am. Phys. Soc. **44**, 59, 1999.
24. "Laser Induced Fluorescence Measurements of a Helium Arcjet Flow," Q.E. Walker and M. A. Cappelli, 41st Annual Meeting of the Division of Plasma Physics, American Physical Society, New Orleans, LA, November 16-20, 1999. See also Bull. Am. Phys. Soc. **44**, 29, 1999.
25. "Dispersion of Low Frequency Azimuthal Waves in Hall Discharges," M. A. Cappelli, D.P. Schmidt, and N.B. Meezan, 41st Annual Meeting of the Division of Plasma Physics, American Physical Society, New Orleans, LA, November 16-20, 1999. See also Bull. Am. Phys. Soc. **44**, 61, 1999.
26. "Anomalous Transport in Closed-Drift Hall Transport," N.B. Meezan, M. A. Cappelli, 41st Annual Meeting of the Division of Plasma Physics, American Physical Society, New Orleans, LA, November 16-20, 1999. See also Bull. Am. Phys. Soc. **44**, 29, 1999.

27. "Two Dimensional Simulations of Hall Thrusters," E. Fernandez and M.A. Cappelli, 27th IEEE International Conference on Plasma Science, New Orleans, LA, June 4-7, 2000. See also Proceedings Record, pg. 188.
28. "Two Dimensional Simulations of Hall Thrusters," E. Fernandez and M.A. Cappelli, 27th IEEE International Conference on Plasma Science, New Orleans, LA, June 4-7, 2000. See also Proceedings Record, pg. 188.
29. "Fluctuation-Induced Electron Transport in Closed-Drift Hall Discharges," M. A. Cappelli, N.B. Meezan, and E. Chesta, 27th IEEE International Conference on Plasma Science, New Orleans, LA, June 4-7, 2000. See also Proceedings Record, pg. 187.
30. "Electron Density Measurements for Determining the Anomalous Electron Mobility in a Coaxial Hall Discharge Plasma," N.B. Meezan and M.A. Cappelli, AIAA 2000-3420, 36th AIAA Joint Propulsion Conference, Huntsville, AL, July 16-29, 2000.
31. "The Anomalous Electron Mobility in a Coaxial Hall Discharge Plasma Hall," N.B. Meezan, M. A. Cappelli, 42nd Annual Meeting of the Division of Plasma Physics, American Physical Society, Quebec City, Quebec, October 23-27, 2000. See also Bull. Am. Phys. Soc. **45**, 30, 2000.
32. "The Anomalous Electron Mobility in a Coaxial Hall Discharge Plasma Hall," N.B. Meezan, M. A. Cappelli, 42nd Annual Meeting of the Division of Plasma Physics, American Physical Society, Quebec City, Quebec, October 23-27, 2000. See also Bull. Am. Phys. Soc. **45**, 30, 2000.
33. "Plasma Fluctuations within a Hall Discharge," E. Chesta, N.B. Meezan, and M. A. Cappelli, 42nd Annual Meeting of the Division of Plasma Physics, American Physical Society, Quebec City, Quebec, October 23-27, 2000. See also Bull. Am. Phys. Soc. **45**, 30, 2000.
34. "Impact Pressure Measurements of a Helium Arcjet Flow," Q.E. Walker and M. A. Cappelli, 42nd Annual Meeting of the Division of Plasma Physics, American Physical Society, Quebec City, Quebec, October 23-27, 2000. See also Bull. Am. Phys. Soc. **45**, 92, 2000.
35. "A Linear Stability Analysis of a Magnetized Hall Plasma Discharge," M. A. Cappelli, E. Chesta, and N.B. Meezan, , 42nd Annual Meeting of the Division of Plasma Physics, American Physical Society, Quebec City, Quebec, October 23-27, 2000. See also Bull. Am. Phys. Soc. **45**, 165, 2000.
36. "Modeling Anomalous Electron Transport in Two-Dimensional Simulations of Hall Thrusters," E. Fernandez and M. A. Cappelli, 42nd Annual Meeting of the Division of Plasma Physics, American Physical Society, Quebec City, Quebec, October 23-27, 2000. See also Bull. Am. Phys. Soc. **45**, 166, 2000.

Patent Disclosures and Applications Arising Directly from this Grant

1. "A Method and Apparatus for Neutralizing Very High Power Ion Rockets," M.A. Cappelli, Invention Disclosure, Stanford Docket S97-198. Assigned to Stanford University, Patent Pending.
2. "Linear Hall Thruster," M.A. Cappelli, D.B. Schmidt, N.B. Meezan, and W.H Hargus, Jr. Invention Disclosure, Stanford Docket S99-117. Assigned to Stanford University, Patent Pending.

Appendix I

Laser-Induced Fluorescence Measurements in the Interior of a Closed-Electron Drift Hall Discharge

W.A. Hargus, Jr., and M.A. Cappelli,

To appear in *Applied Physics B - Lasers and Optics*, 2001.

Laser-Induced Fluorescence

Measurements of Velocity within a Hall Discharge

W.A. Hargus, Jr.* and M.A. Cappelli

Mechanical Engineering Department

Thermosciences Division

Stanford University

Stanford, CA 94305

Abstract

The results of a study of laser induced fluorescence velocimetry of neutral and singly ionized xenon in the plume and interior portions of the acceleration channel of a Hall thruster plasma discharge operating at powers ranging from 250 to 725 W are described. Axial ion and neutral velocity profiles for four discharge voltage conditions (100 V, 160 V, 200 V, 250 V) are measured as are radial ion velocity profiles in the near field plume. Ion velocity measurements of axial velocity both inside and outside the thruster as well as radial velocity measurements outside the thruster are performed using laser induced fluorescence with nonresonant signal detection on the xenon ion $5d[4]_{7/2} - 6p[3]_{5/2}$ excitation transition while monitoring the signal from the $6s[2]_{3/2} - 6p[3]_{5/2}$ transition. Neutral axial velocity measurements are similarly performed in the interior of the Hall thruster using the $6s[3/2]_2^0 - 6p[3/2]_2$ transition with resonance fluorescence collection. Optical access to the interior of the Hall thruster is provided by a 1 mm wide axial slot in the insulator outer wall. While the majority of the ion velocity measurements used partially saturated fluorescence to improve the signal to noise ratio, one radial trace of the ion transition was taken in the linear fluorescence region and yields an xenon ion translational temperature between 400 and 800 K at a location 13 mm into the plume.

Introduction

Due to their high specific impulse and high thrust efficiencies, Hall thrusters are now being considered for use on commercial, research, and military spacecraft. This technology provides economic advantages for a number of missions and its use can be translated into lower launch mass, longer time on station, or larger payloads [1]. In order to extend the performance and operating envelope of Hall thrusters, there is a need for increased understanding of the complex phenomena that control propellant ionization and acceleration within the discharge. In order to more fully understand the physics in these discharges, several laboratory model Hall thrusters have been constructed at Stanford University. These thrusters serve as test articles for model development and advanced plasma diagnostics including laser induced fluorescence (LIF), probes of various types, and thrust measurements [2-5].

* Now located at
Air Force Research Laboratory
Spacecraft Propulsion Branch
Edwards AFB, CA

Laser based techniques have been developed to nonintrusively probe neutral and ionized xenon [2,5]. Such measurements in the plumes of Hall and other types of ion thrusters provide important information on the expansion of the plasma plume and its potential effect on satellite propulsion design and integration. Laser based diagnostic measurements have been previously employed to examine plume plasma properties in other electric propulsion devices. For example, the hydrogen arcjet has been extensively studied using lasers to measure velocity, temperature, and electron number density [6]. However, few measurements (especially optical measurements) have been made within the interior discharge of these devices. The high spatial resolution of single point LIF is essential in probing nonuniform plasma environments such as those inside Hall thrusters and other electric propulsion devices.

Ion velocity measurements of axial velocity, both inside and outside the thruster as well as radial velocity measurements outside the thruster, are performed using LIF with nonresonant signal detection exciting the xenon ion $5d[4]_{7/2} - 6p[3]_{5/2}$ electronic transition while monitoring signal from the $6s[2]_{3/2} - 6p[3]_{5/2}$ transition. Neutral axial velocity measurements are similarly performed in the interior of the Hall thruster using the $6s[3/2]_2^0 - 6p[3/2]_2$ transition with resonance fluorescence collection. The majority of the velocity measurements use partially saturated fluorescence to improve the signal to noise ratio.

Theory

Laser Induced Fluorescence

Laser induced fluorescence is used to detect velocity-induced shifts in the spectral absorption of xenon atoms and ions. The fluorescence is monitored as a continuous-wave laser is tuned in frequency over the transition of interest, of energy $h\nu_{12}$. Measurements can be made with high spatial resolution, determined by the intersection of the probe laser beam with the fluorescence optical collection volume.

In laser-induced fluorescence velocimetry, an atom or ion moving with a velocity component u relative to the direction of the incoming laser will absorb the light at a frequency shifted from that of stationary absorbers due to the Doppler effect. The magnitude of this frequency shift $\delta\nu_{12}$ is:

$$\delta\nu_{12} = \nu_{12} \frac{u}{c} \quad (1)$$

The measured fluorescence signal is given by [7-9]:

$$S_f = \eta_d \alpha_c h\nu_{12} A_{21} N_2 \quad (2)$$

where η_d is the efficiency of the detection system, α_c accounts for geometric factors involving the collection system, and A_{21} is the Einstein coefficient for spontaneous emission of the relevant transition. For low

laser intensities, rate equation analysis indicates that the upper level population N_2 , and therefore the fluorescence signal, is linearly dependent on laser intensity at steady state, i.e.,

$$N_2 \sim I_\nu B_{12} \phi_\nu \quad (3)$$

where I_ν is the spectral irradiance at frequency ν , B_{12} is the Einstein stimulated absorption coefficient, and ϕ_ν is the transition's spectral line shape which accounts for the variation of the absorption or laser excitation with frequency. The line shape is determined by the environment of the absorbing atoms, so an accurate measurement of the line shape function can lead to the determination of various plasma parameters. However, for velocity measurements, partially saturated fluorescence with a distorted line shape can still provide an adequate measure of the mean velocity. This was experimentally verified with several saturation studies which also examine the Doppler shift. The variation of the resultant velocities was found, in this study, to be less than the experimental uncertainty for the ions (± 500 m/s), or for the neutrals (± 60 m/s).

Several factors affect the line shape and give rise to broadening and/or shift of the spectral line. In high temperature plasmas, the most significant is Doppler broadening due to the absorber's random thermal motion, characterized by the molecular kinetic temperature, T_{kin} . When the absorbing species velocity distribution is Maxwellian in shape, the Doppler broadening results in a Gaussian line shape. Collisional interactions between the absorbers and other species in the plasma give rise to spectral line shapes that are often Lorentzian. This includes interactions with charged particles (Stark broadening) and uncharged particles (van der Waals broadening). If both Doppler broadening and collisional broadening are important and independent, the resulting line shape is a convolution of the Gaussian and Lorentzian line shape into a Voigt line shape [9].

The absorption line shape is an intrinsic property of the absorbers, whereas the fluorescence excitation line shape is the variation in the detected fluorescence signal with frequency as the laser is tuned across the absorption line feature. If the laser excitation significantly perturbs the populations of the coupled levels, it is said to be *saturating* the transition and the fluorescence signal is then a nonlinear function of laser intensity. In cases where the laser intensity is significantly below the saturation level and the laser linewidth is small compared to the measured linewidth, the fluorescence excitation line shape reflects the spectral absorption line shape as given by Eqns. 2 and 3. When the laser intensity is sufficiently high to saturate the transition, the fluorescence excitation line shape is broader than the spectral line shape and the fluorescence intensity is less than it would be if it were linear with the laser intensity I_ν . The saturation intensity, defined as that intensity which produces a fluorescence signal half of what it would be if the fluorescence was linear with I_ν , depends inversely on the line strength of the particular transition. Stronger transitions have a smaller saturation intensity and thus a larger saturation effect for a given laser intensity.

Hyperfine Structure

The nine isotopes of xenon, the propellant most commonly used in Hall plasma thrusters, each have a slight difference in their electron transition energies due to their differences in mass [10]. The odd mass isotopes are further spin split due to nuclear magnetic dipole and electric quadrupole moments. Nuclei which have an odd number of protons and/or an odd number of neutrons possess an intrinsic nuclear spin $I\hbar/2\pi$, where I is integral or half-integral depending on if the atomic mass is even or odd, respectively [11]. For nuclei with non-zero nuclear spin (angular momentum), the interaction of the nucleus with the bound electrons lead to the splitting of levels with angular momentum J into a number of components, each corresponding to a specific value of the total angular momentum $F = I + J$ [12]. As a result of this interaction, F is a conserved quantity while I and J individually are not. The interaction is weak allowing the hyperfine splitting of each level to be taken independently of the other levels. The number of nuclear spin split hyperfine components is $2I + 1$ if $J \geq I$ and $2J + 1$ if $J < I$, with F taking on the values $F = J + I, J + I - 1, \dots, |J - I|$ [12,13] while satisfying the selection rules imposed on F , i.e., $\Delta F = 0, \pm 1$, unless $F = 0$, in which case $\Delta F \neq 0$.

With these selection rules on the quantum numbers for a particular electronic transition, and with knowledge of the hyperfine structure constants which characterize the magnetic dipole and electric quadrupole moments of the nucleus [11], the hyperfine energy shifts from the position of the energy for the unshifted level with angular momentum J can be easily calculated [13]. The relative intensities of transitions between these levels is derived assuming Russell-Saunders coupling [13], allowing the complete construction of the fluorescence lineshape. Of course, the intensities of the isotope shifted transitions are proportional to each isotope's relative abundance [11,14-15]. The relative intensities of the nuclear spin split hyperfine splitting are governed by two summation rules [12]. First, the sum of the intensities of all the lines of the hyperfine structure of a transition $J \rightarrow J'$ (the prime refers to the upper level involved in the transition) originating from a component F of the level J is proportional to the statistical weight of this component, $2F + 1$. Second, the sum of the intensities of all the lines of the hyperfine structure the transition $J \rightarrow J'$ ending on the component F' of the level J' is proportional to the statistical weight of this component, $(2F' + 1)$. With these two sum rules, a system of linear equations are solved for the relative intensities of the nuclear spin split components of each isotope.

Xenon Spectroscopy

For the results reported here, we probed the 823.2 nm and 834.7 nm electronic transitions of neutral and singly ionized xenon, respectively. The isotopic and nuclear-spin effects contributing to the hyperfine structure of the $6s[3/2]_2^0 - 6p[3/2]_2$ neutral xenon transition at 823.2 nm produce 21 spectral lines, 15 of which are shown in the transition schematic in Fig. 1a (the other six are of the same transition shown for the even isotopes). Similarly, the $5d[4]_{7/2} - 6p[3]_{5/2}$ xenon ion transition at 834.7 nm has a total of 19 isotopic and spin split components, 13 of which are shown in Fig. 1b (again, the other six are of the same transition shown for the even isotopes). The hyperfine splitting constants are only known for a limited set of energy

levels [16-20]. While isotope shifts and all of the hyperfine splitting constants are available for the upper and lower levels of the neutral 823.2 nm transition, the 834.7 nm xenon ion transition only has data on the nuclear spin splitting constants of the upper state, and no information is available on the transition dependent isotope shifts. For LIF measurements primarily aimed at determining velocities within the plasma flow, it is often convenient to probe more accessible transitions for which there is incomplete knowledge of the isotopic and nuclear spin splitting constants. Manzella has shown that the $5d[4]_{7/2} - 6p[3]_{5/2}$ xenon ion transition at 834.7 nm may be used to make velocity measurements in a Hall thruster plume [21]. A convenient feature of this transition is the presence of a relatively strong line originating from the same upper state ($6s[2]_{3/2} - 6p[3]_{5/2}$ transition at 541.9 nm) which allows for nonresonant fluorescence collection [22]. A nonresonant fluorescence scheme is preferred where there is the possibility of laser scattering from internal surfaces of the discharge.

Experiment

Test Facility

The test facility consists of a non-magnetic cylindrical stainless steel vacuum vessel 1 m in diameter and 1.5 m in length, pumped by two 50 cm diffusion pumps (backed by a 425 l/s mechanical pump) mounted at each end. Figure 2 shows a schematic of the facility. The base pressure with no flow is approximately 10^{-6} Torr as measured by an ionization gauge calibrated for nitrogen. Chamber pressures during discharge operation result in pressures of approximately 10^{-4} Torr (3×10^{-5} Torr on xenon, $\pm 50\%$). Gas flow to the Hall thruster anode and cathode is throttled by two Unit Instruments 1200 series mass flow controllers factory calibrated for xenon. The gas (propellant) used in this study was research grade (99.995%) xenon.

The thruster is mounted on a two axis translation system having a vertical range of travel of 30 cm and axial (horizontal) range of 8 cm, each with a resolution of about $10 \mu\text{m}$. Although the repeatability is considerably courser, it is still significantly less than the dimensions of the laser probe volume in the axial dimension. For internal LIF measurements, the thruster is mounted on a platform that provides optical access through a slot machined into the acceleration channel wall (described below). The view of the thruster mounting scheme is also shown in Fig. 2.

Hall Thruster

The thruster used in this study has been described in detail extensively elsewhere [4]. It has four outer magnetic windings and a single inner winding generating the magnetic field, which is a maximum near the discharge exit plane. The insulator is constructed from 2 sections of cast alumina tubing 84 mm in length cemented to a machinable alumina back plate. The anode, which also serves as the gas distributor, is positioned at the back of the discharge channel constructed from the coaxial assembly of the alumina tubes. The channel has an outer diameter of 95 mm and a 12 mm width. A cross-sectional view of the assembled discharge thruster is shown in Fig. 3. Not shown in Fig. 3 is the external hollow cathode (ion Tech HCN-252),

positioned with its orifice 20 mm beyond the thruster exit plane, used to neutralize the ion beam and sustain the anode discharge.

For the LIF studies within the discharge chamber, a slot parallel to the axis 1 mm wide was machined into the outer insulator. The slot width was selected to be less than the local electron Larmor radius to minimize its influence on the discharge properties. The slot provides optical access to the interior of the Hall thruster, and operation with the slot did not differ significantly from the operation with the unslotted insulator (identical current-voltage characteristics). Despite the presence of the slot, optical access to the interior is still limited near the exit plane by the front plate of the magnetic circuit, precluding optical measurements very near the exit plane. The front iron plate is not cut since this would modify the local magnetic field.

Laser Induced Fluorescence

The experimental apparatus used for the LIF measurements includes a tunable Coherent 899-21 single frequency titanium sapphire laser, actively stabilized to provide line widths on the order of 1 MHz with near zero frequency drift. The titanium sapphire laser is pumped by a Coherent Nd:YAG solid state Verdi pump laser, which provides 5 W of single mode pump power at 532 nm. The tunable laser wavelength is monitored by a Burleigh Instruments WA-1000 scanning Michelson interferometer wavemeter with a resolution of 0.01 cm^{-1} .

The laser beam is chopped to allow for phase sensitive detection and directed into the Hall thruster plume by a series of mirrors. For axial velocimetry measurements, the slightly divergent beam (1.7 milliradians full angle) is focused to a submillimeter beam waist by a 50 mm diameter, 1.5 m focal length lens as shown in Fig. 2. For radial velocimetry measurements, the beam enters through a side window and is focused by a 50 mm diameter, 50 cm focal length lens as shown in Fig. 5. The collection optics for both radial and axial velocity measurements consist of a 75 mm diameter, 60 cm focal length, collimating lens. The collected light is then focused on to the entrance slit of a 0.5 m Ebert-Fastie monochromator with a 50 mm diameter, 30 cm focal length, lens. An optical field stop is placed between the two lenses to match the $F/\#$ of the optical train with that of the monochromator. The monochromator is used in the collection optical train as a narrow band optical filter so that only light from the transition of interest is collected. With entrance and exit slits fully open ($425 \mu\text{m}$), the 600 groove/mm plane grating (blazed for 600 nm) within the monochromator allows the exit slit mounted Hamamatsu R928 photomultiplier tube (PMT) to sample a wavelength interval of approximately 1 nm. The orientation of the monochromator allows the slit aperture to define the length of the probe beam along which the fluorescence is collected. The sample volume for the axial data presented in this work is approximately $100 \mu\text{m}$ in diameter and 2 mm in length. Similarly, the sample volume of the radial data is approximately $100 \mu\text{m}$ in diameter and 1 mm in length. For neutral xenon LIF velocimetry measurements, a portion of the probe beam is split from the main beam, passed

through a xenon glow discharge tube, and used as an stationary absorption reference. A silicon photodiode monitors the absorption signal. This use of the glow discharge tube is only possible for neutral xenon. The glow discharge does not support a sufficient population of excited state ions. However, the unshifted ion transition line center was confirmed to correspond to that taken from the literature by the observation of very slow moving ions near the anode, and by radial measurements near the acceleration channel center.

The probe laser beam is chopped, and the LIF signal is collected using a Stanford Research Systems SRS-850 digital lockin amplifier. Concurrently, the absorption signal from the stationary reference is collected using an SRS-530 lockin amplifier. Data from the absorption signal, laser power output, and the wavemeter are stored on the digital lockin amplifier using 3 available analog inputs along with the LIF signal. Typical tests consist of a 12-20 GHz scan of the probe laser frequency over a 3 minute period. The beam is chopped at a frequency of 1.5 kHz, and both lockin amplifiers use 1 s time constants. Data is sampled at 8 Hz, producing four traces of approximately 2,000 points for each velocity data point. Several unsaturated traces using lower laser intensities, 10 s time constants, and 10 min scans were also collected.

Results and Analysis

The Hall thruster is operated at four conditions for the work reported here. At each condition, the peak magnetic field is 125 G, the mass flow to the anode is 2 mg/s, and the mass flow to the external hollow cathode is 0.3 mg/s. The test conditions correspond to discharge voltages of 100, 160, 200, and 250 V. The anode currents for these conditions are 2.1, 2.4, 2.6, and 2.9 A, respectively. The total power consumed by the cathode and magnet circuit is approximately 30 W. It should be noted that the power dissipated in the ballast resistors on the anode and cathode keeper lines (~10 W) is not included in these calculations.

All spatially resolved measurements are referenced to a two coordinate system shown in Fig. 5. The position in the radial coordinate is referenced to the radial location corresponding to the midpoint of the acceleration channel using the variable D , defined as positive toward the thruster centerline. The axial coordinate is given by Z which is the distance from the thruster exit plane and is defined as positive along the thrust vector.

Saturation Study

The $5d[4]_{7/2} - 6p[3]_{5/2}$ xenon ion transition at 834.7 nm was probed to extract local velocity data from the Doppler shift of the measured fluorescence. Figure 6 shows the saturation curve of the transition at a location 13 mm from the exit plane at the center of the acceleration channel. Here, the laser beam is propagating normal to the thrust vector and the measurement is of the radial velocity component. A typical saturated trace (laser power of 20 mW) used to determine the velocity in the probed volume is compared to an unsaturated trace (laser power of 0.2 mW) from the same location in Fig. 7. Both traces are normalized in the figure to unity peak signal.

Velocity measurements of the saturation curve data making up Fig. 6 are shown in Fig. 8. The mean velocity for these data points yields a value of -62 m/s with a standard deviation of 65 m/s and a range of 127 m/s. The absolute accuracy of the measurements is limited by the specified uncertainty of the wavemeter reading, which is ± 500 m/s at this wavelength. The important conclusion that may be drawn from this data is that the $5d[4]_{7/2} - 6p[3]_{5/2}$ xenon ion transition of xenon provides useful LIF velocimetry data even when partially saturated. This allows the collection of partially saturated fluorescence signals, maximizing the signal to noise ratio and/or allowing for faster scans while still being able to extract velocity data from the fluorescence signal. These measurements also serve as a confirmation of an improved accuracy of the unshifted wavelength since a finite radial velocity is not expected at this location. Similar results were also obtained in a neutral xenon LIF saturation study.

Xenon Ion LIF Velocimetry

The axial LIF velocimetry measurements consist of two data sets for each operating condition. The first data set includes ion velocity measurements taken externally extending from the exit plane to approximately $Z = 35$ mm. The second data set contains internal axial velocity measurements taken from the exit plane to approximately $Z = -75$ mm. These ranges are imposed by the limited travel of the translation stage that provides axial motion to the Hall thruster. Axial velocimetry measurements were taken every 2.5 mm with a sample probe volume of $100\ \mu\text{m}$ in diameter and 2 mm long. For several of the test conditions examined, profiles of the axial velocity across the coordinate D were also examined. Measurements of near plume radial ion velocities were also performed. These measurements are limited to the plume due to the limited optical access to the interior of the Hall thruster.

The complete axial velocity profiles for the four cases examined are shown in Fig. 9. The error bars correspond to the ± 500 m/s uncertainty associated with the determination of the magnitude of the Doppler shift relative to the unshifted line center. The axial velocity profiles exhibit the expected behavior. The velocity is near zero near the anode ($Z = -78$ mm), and begins to rise near $Z = -10$ mm at the edge of the acceleration zone. The ions are rapidly accelerated in the region of the exit plane and reach their full velocity in the neighborhood of $Z = 20$ mm. This latter position corresponds to the location of the hollow cathode neutralizer relative to the body of the thruster and is sometimes referred to as the *cathode plane* in the literature [21].

The length of the acceleration region in all cases is invariant at 30 mm. Therefore, increases in the anode potential result in a concomitant increase of the axial electric field component within the thruster acceleration channel. The initial acceleration is seen to begin at 10 mm within the thruster where the magnetic field has a value of approximately 85% of the centerline maximum. The propellant acceleration is completed 20 mm beyond the exit plane when the magnetic field has a value of approximately 25% of the centerline maximum.

Significant acceleration of the ionized propellant occurs outside the Hall thruster. This is consistent with the results first identified in a Hall discharge with a much shorter acceleration channel [2]. It is noteworthy that the velocity increment imparted to the propellant outside the of Hall thruster is essentially constant, invariant to discharge voltage, with an average value of 5,000 m/s. Only for the 100 V case, does the majority of the acceleration occur outside the thruster. Higher discharge voltages appear to have a constant percentage of the acceleration occurring externally. It is also equally interesting to cast this result in terms of the kinetic energy of the propellant. In the case of the 100 V discharge operation, approximately 90% of the energy is deposited into the propellant between the exit and cathode planes. For the 250 V case, the fraction of energy deposition beyond the exit plane is nearer to 60%. It appears then that the majority of the energy deposition into the Hall thruster propellant occurs outside the thruster. However, since the thrust is equivalent to the momentum flux, the majority (65%) of the thrust is still generated within the thruster in all cases above 100 V. It is further noteworthy that in all the cases approximately 60 eV is unaccounted. This value is constant to within the uncertainties of the velocity measurement and implies that the mechanism responsible for this loss is invariant with the applied anode potential. This energy loss may be a product of the anode and cathode potential falls, or other mechanisms common to these discharges (e.g. distribution of in the ion production, or resistive losses in regions of low ionization fractions). It is noted that these measurements are limited to axial velocities and do not account for losses due to plume divergence.

Several radial profiles of the axial ion velocity in Fig. 10 illustrate the radial variation of the measured axial velocities for a discharge voltage of 160 V at two locations in the plume and one within the thruster for a discharge voltage of 200 V. The width of the acceleration channel is 12 mm ($-6 \text{ mm} < D < 6 \text{ mm}$). The axial velocity profile is nearly flat which strongly implies lines of constant potential in the radial direction. The slightly concave distribution inside the channel (200 V case) is consistent with the expected equipotential surfaces associated with the radial magnetic field.

Radial velocity measurements were also performed in the plume. Combined with the above axial velocity measurements and the observation that the axial velocity appears to be independent of D , vector plots of the near plume may be constructed. Figure 11 shows a vector plot constructed for a 200 V discharge voltage. In this case, radial velocities vary linearly with D with near zero velocity at $D = 0 \text{ mm}$ and peak at values above 6,000 m/s as close as $Z = 13 \text{ mm}$ and $D = 8 \text{ mm}$. A prominent feature of a Hall thruster plume is the luminous central cone originating at the thruster axis adjacent to the center pole piece. Although the propellant stream exits the thruster in an annulus, an intense, optically emitting conical feature extends a significant distance into the vacuum chamber (10 to 30 cm for our background pressures) and is especially evident at higher discharge voltages. The inward focus of the divergent propellant flow is likely a contributing mechanism in the formation of this intriguing feature which is not precisely understood.

Ion Line Shape Analysis

The hyperfine splitting constants for the xenon ion $5d[4]_{7/2} - 6p[3]_{5/2}$ transition at 834.7 nm are only known for the upper $6p[3]_{5/2}$ state. The isotope shifts for this transition are also unknown. While this does not greatly impact the accuracy to which velocities may be determined, it does impact the ability to use this transition for accurate measurements of the ion velocity distribution, or *temperature*. We point out here that the notion of a temperature for the ions in this flow is highly tenuous, as the ions may be treated kinetically, do not suffer many collisions, and are born (created) at distributed axial locations within the discharge. Furthermore, a time averaged broadening of the fluorescence excitation spectra can arise due to oscillations in the zone of ionization. King has shown by mass and resolved energy analysis that the axial velocity of the ions has an energy distribution of approximately 10 eV (in the far field) due in part to the plasma oscillations within the Hall thruster [23]. The issue of the distribution of ion velocities due to the axial location where they were born is minimized by examining the fluorescence spectra in the radial direction. The spectra is taken from the position with the minimum measured velocity, approximately 100 m/s (± 500 m/s) at a location of $D = 0$ mm and $Z = 13$ mm. In order for a temperature to be extracted from the measured lineshape, the ion population is assumed to be Maxwellian, or at least frozen in a close facsimile.

An estimate of the ion kinetic temperature with uncertainties of 40-70% is possible. A radial excitation unsaturated fluorescence trace is shown in Fig. 12 and compared to a line shape model developed by Cedolin [24]. The model uses the $5d[3]_{7/2}$ lower level hyperfine spin splitting and isotopic shift data from the 605.1 nm transition and the measured splitting data for the upper $6p[3]_{5/2}$ level. Lorentzian broadening is neglected and only Doppler broadening is considered. The best fit of this model predicts a kinetic temperature of approximately 450 K. The model does not completely predict the outlying features, but this is expected since the spin splitting constants for the $5d[3]_{7/2}$ state are used for the lower level rather than those for the $5d[4]_{7/2}$ state probed here. If hyperfine splitting is ignored and only the isotope shifts corresponding to the values for the 605.1 nm transition are used, the model predicts a kinetic temperature of approximately 800 K. Neglecting all hyperfine splitting mechanisms, including isotopic and nuclear spin splitting, an *upper bound* on the temperature of 1,700 K is determined from the fluorescence Doppler half width. The uncertainty of this measurement is in large part due to the uncertainties of the spectral data as well as due to the noise in the fluorescence signal. A similar measurement in the plume of a SPT-100 by Manzella yielded a kinetic temperature of approximately 800 K [21]. It should be noted that Manzella used an incorrect value of J for the lower state which was first misidentified by Humphreys [25] and propagated by Moore [26] before finally being corrected by Hansen and Persson [22].

Neutral LIF Velocimetry

Figure 13 shows the results of axial neutral xenon velocity measurements within the acceleration channel. The four cases examined show very similar behavior. The initial velocity near the anode is very low. The neutral velocity slowly rises until a position of approximately 20 mm within the thruster. At this point, where the ion acceleration is also seen to begin, the neutrals are accelerated at a higher rate until near

the exit plane where the acceleration appears to slow and even possibly reverse when the thruster is operated at higher voltages. The decrease in neutral xenon velocity is likely due to thruster ingestion of background xenon. Since the effect appears to grow with increased discharge voltage, it is possible that a portion of the propellant flow reflected from nearby vacuum facility walls (now entirely consisting of neutrals) is ingested by the thruster.

Flow from the cathode may be eliminated as the source of the apparent deceleration of the neutrals for a variety of reasons. First, the flow from the cathode, although 15% of the anode flow, is exiting from a 2 mm orifice approximately 12 cm above the sample volume. Flow from the cathode should be sufficiently diffuse and not affect the neutral velocity measurements in the sample volume. Second, the cathode is 2 cm downstream of the exit plane and angled 30° from the front plate pointed along the thrust axis. It is difficult to envision the cathode affecting the neutral velocity measurements within the acceleration channel. It is therefore almost certain that random neutral flux from the chamber background is responsible for the apparent drop in neutral velocity seen near the exit plane in Fig. 13.

Due to the highly nonequilibrium nature of the Hall thruster, it is important to understand the apparent acceleration of the neutrals beginning 40 mm upstream of the exit plane. The plasma within the Hall thruster is required to be of low collisionality by the constraint that the magnetic field limit the electron flux to the anode. The disparate velocities of the ions and neutrals strongly suggest that the neutral and ion populations are not coupled. As such, the apparent acceleration of the neutrals may actually be an artifact of the time of flight of the neutrals through the volumetric zone of ionization. Slower neutrals, or neutrals that travel a longer effective path length due to collisions with the walls of the acceleration channel, have a greater probability of being ionized than do neutrals in the high energy portion of the velocity distribution. Therefore, neutrals from the high energy range of the velocity distribution are more likely to reach the upstream portion of the acceleration channel. In this case, there is no actual acceleration of the neutrals, but rather a depletion of the slower moving neutrals by ionization.

The depletion of the slower neutral velocity classes accounting for the apparent acceleration of the neutrals as seen in Fig. 13 may be qualitatively explained by considering the one dimensional Boltzmann equation [27].

$$u \frac{\partial}{\partial z} [nf(u)] = -[nf(u)]n_e S_i \quad (18)$$

Where n is the neutral number density, u is the neutral velocity class, z is the spatial coordinate, $f(u)$ is the velocity distribution function, n_e is the local plasma electron number density, and S_i is the ionization rate coefficient. The generalized one dimensional Boltzmann equation is simplified here by assuming the process is steady with no external forces and that the sole depletion mechanism for the neutral velocity classes is

electron collisional ionization. Implicit in these assumptions is that the ions and neutrals do not significantly interact.

Equation 18 may be easily integrated with respect to $nf(u)$ to produce an analytic solution if the ionization rate coefficient S_i and the electron number density n_e are assumed to be constant. In this case, the population of the u velocity class $nf(u)$ exponentially decays with the spatial variable z moderated by the value of u .

$$nf(u) \sim e^{-z/u} \quad (20)$$

The qualitative conclusion drawn from this straightforward analysis of the one dimensional Boltzmann equation is that the neutral density in a model plasma is depleted along the Z axis due to neutral-electron collisional ionization. This relative depletion depends on the velocity class. Neutrals in the lower velocity classes have a greater probability of being ionized when passing through the zone of ionization than neutrals of higher velocity classes. Therefore, the apparent acceleration of the neutrals in Fig. 13 is most likely the result of the depletion of the slower moving neutrals rather than an acceleration process.

Conclusions

Measurements of xenon ion and neutral velocities were performed in the plume and into the interior of the thruster through a 1 mm wide slot in the outer insulator wall. From these measurements, information on propellant energy deposition, electric field strength, and flow divergence were extracted. Xenon ion velocity measurements of axial velocity both inside and outside the thruster as well as radial velocity measurements outside the thruster, were performed using LIF with nonresonant signal detection using the xenon ion $5d[4]_{7/2} - 6p[3]_{5/2}$ electronic transition while monitoring signal from the $6s[2]_{3/2} - 6p[3]_{5/2}$ transition. Neutral velocity measurements were similarly performed in the interior of the Hall thruster using the $6s[3/2]_2^0 - 6p[3/2]_2$ transition with resonance fluorescence collection. Most velocity measurements used partially saturated fluorescence to improve the signal to noise ratio. One radial trace of the xenon ion transition was taken in the linear fluorescence region and yielded a plume ionic translational temperature between 400 and 800 K. However, since the hyperfine structure constants are not known for the $5d[4]_{7/2}$ level, the constants for the $5d[3]_{7/2}$ level were used instead. This result should therefore be viewed with caution. An upper limit on the kinetic temperature using only the full width at half maximum assuming no hyperfine splitting yields a temperature of 1,700 K. From the neutral velocity measurements, the neutrals appear to be accelerated within the thruster. Conclusions drawn from analysis of the one dimensional Boltzmann equation imply that neutrals are depleted along the Z axis due to neutral-electron collisional ionization, and the relative depletion depends on the velocity class of the neutral atom. This preferentially depletes the lower velocity classes producing the apparent acceleration of the neutrals.

Acknowledgments

This work is supported by the Air Force Office of Scientific Research. W.A. Hargus, Jr. was supported under the Air Force Palace Knight Program.

References

1. Janson S W 1993 (AIAA 29th Joint Propulsion Conference) 93-2220
2. Cedolin R J, Hargus Jr W A, Storm P V, Hanson R K, and Cappelli M A 1997 *J. Phys. B* **65** 459
3. Hargus Jr W A, Meezan N B, and Cappelli M A 1997 (AIAA 33rd Joint Propulsion Conference) 97-3050
4. Hargus Jr W A, Jr., Cedolin R J, Meezan N B, and Cappelli M A 1997 (AIAA 33rd Joint Propulsion Conference) 97-3081
5. Hargus Jr W A and Cappelli M A, "Interior and Exterior Laser-Induced Fluorescence and Plasma Potential Measurements within a Hall Thruster," *submitted to Journal of Propulsion and Power July 2000*
6. Storm P V 1997 *Thermosciences Division Report No. TSD-102: Optical Investigations of Plasma Properties in the Interior of a Arcjet Thrusters* (Mech. Eng. Dept. Stanford University)
7. Lucht R P 1987 *Laser Spectroscopy and its Applications* eds Radziemski L J, Solarz R W, and Paisner J A (New York: Marcel Dekker) 623
8. Eckbreth A C 1996 *Laser Diagnostics for Combustion Temperature and Species* (Amsterdam: Overseas Publishers Association)
9. Demtroder W 1996 *Laser Spectroscopy: Basic Concepts and Instrumentation* (Berlin: Springer-Verlag)
10. Herzberg G 1944 *Atomic Spectra and Atomic Structure* (New York: Dover Publications)
11. Cowan R D 1981 *The Theory of Atomic Structure and Spectra*, (Berkley: University of California Press)
12. Sobelman I I 1992 *Atomic Spectra and Radiative Transitions* (Berlin: Springer-Verlag)
13. White H E 1934 *Introduction to Atomic Spectra* (New York: McGraw-Hill Book Co.)
14. 1993, *Handbook of Chemistry and Physics: 74th Edition* ed Lidde D R (Boca Raton, Florida: CRC Press)
15. Jackson D A and Coulombe M C 1974 *Proc. R. Soc. Lond. A.* **338** 277
16. Borghs G, De Bisschop P, Silerans R E, Van Hove M, and Van den Cruyce J M 1981 *Atoms and Nuclei.* **299** 11
17. Bingham C R, Gaillard M L, Pegg D J, Carter H K, Mlekodaj R L, Cole J D, and Grffin P M 1982 *Nucl. Instrum. Methods* **202** 147
18. Geisen H, Krumpelmann T, Neuschafer D, and Ottinger Ch 1988 *Phys. Lett. A* **130** 299
19. Fischer W, Huhnermann H, Kromer G, and Schafer H J 1974 *Z. Phys.* **270** 113

20. Bronstrom L, Kastberg A, Lidberg J, Mannervik S 1996 *Phys. Rev. A* **53** 109
21. Manzella D H 1994(AIAA 30th Joint Propulsion Conference) 94-3141
22. Hansen J E and Persson W 1987*Physica Scripta* **36** 602
23. King L B 1998 *Transport-Property and Mass Spectral Measurements in the Plasma Exhaust Plume of a Hall-Effect Space Propulsion System*, (Ph.D. Dissertation, Aerospace Engineering, University of Michigan)
24. Cedolin R J 1997 *Thermosciences Division Report No. TSD-105: Laser-Induced Fluorescence Diagnostics of Xenon Plasmas* (Mech. Eng. Dept. Stanford University)
25. Humpreys C J 1939 *Journal of the National Bureau of Standards* **22** 19
26. Moore C E 1958 *Atomic Energy Levels: Volume III* (Washington: National Bureau of Standards) 113-123
27. Vincenti W G and Kruger Jr C H 1986 *Introduction of Physical Gas Dynamics*, (Malabor, Florida: Krieger Publishing)

List of Figures

Fig. 1. Nuclear spin splitting of the (a) neutral xenon $6s[3/2]_2^0 - 6p[3/2]_2$ and (b) singly ionized xenon $5d[4]_{7/2} - 6p[3]_{5/2}$ transitions.

Fig. 2. Stanford high vacuum facility, collection optics, and LIF probe beam access for axial velocimetry with a cutaway view showing mounted Hall thruster.

Fig. 3. Cross-section of the Stanford Hall thruster. (A) Central iron core. (B) Outer iron cores. (C) Anode and propellant distribution system. (D) Alumina insulator.

Fig. 4. LIF probe beam access for radial velocimetry.

Fig. 5. Coordinate system for referencing locations of measurements.

Fig. 6. Saturation curve of radial xenon ion measurements for an anode discharge voltage of 200 V at $Z = 13$ mm, $D = 0$ mm. Note the uncertainty of these measurements is primarily due to the uncertainty of the optical densities of the neutral density filters used for this measurement ($\pm 5\%$).

Fig. 7. Saturated (20 mW) and unsaturated (0.2 mW) radial xenon ion LIF traces for a discharge voltage of 200 V at $Z = 13$ mm, $D = 0$ mm.

Fig. 8. Invariance of the measured radial xenon ion velocity in the saturation study shown in Fig. 7. Note that the uncertainty of the velocity measurements is approximately ± 500 m/s.

Fig. 9. Axial internal and external xenon ion velocity measurements at $D = 0$ mm for discharge voltages of 100 V, 160 V, 200 V, and 250V.

Fig. 10. Profiles of axial xenon ion velocity measurements for several discharge voltages and axial locations.

Fig. 11. External xenon ion velocity field calculated from radial and axial velocity measurements for a 200 V discharge voltage.

Fig. 12. Model fit to unsaturated radial xenon ion laser induced fluorescence trace at a discharge voltage of 200 V, at a location of $D = 0$ mm and $Z = 13$ mm.

Fig. 13. Axial neutral velocity measurements at $D = 0$ mm for discharge voltages of 100 V, 160 V, 200 V, and 250V.

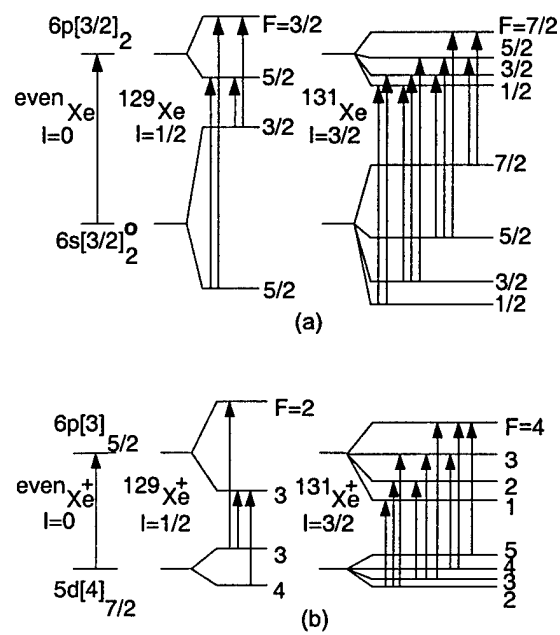


Fig. 1.

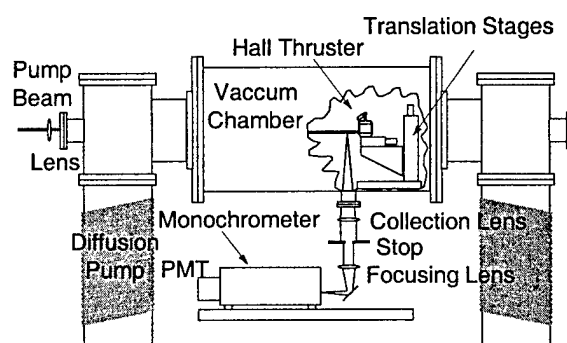


Fig. 2.

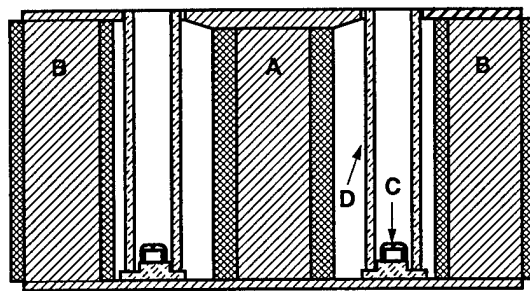


Fig. 3.

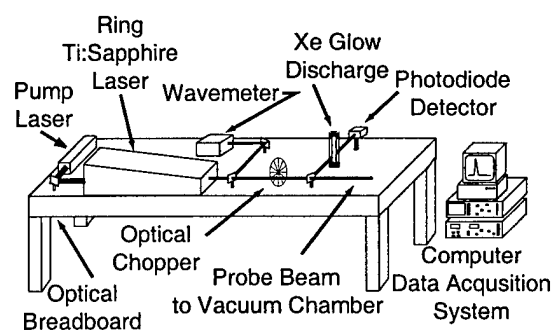


Fig. 4.

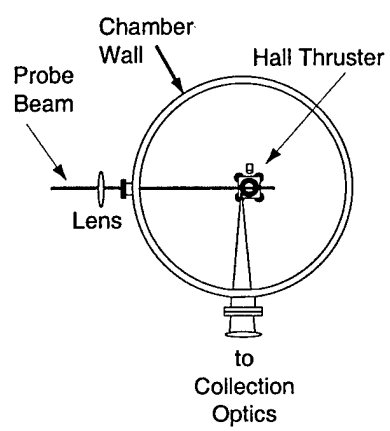


Fig. 5.

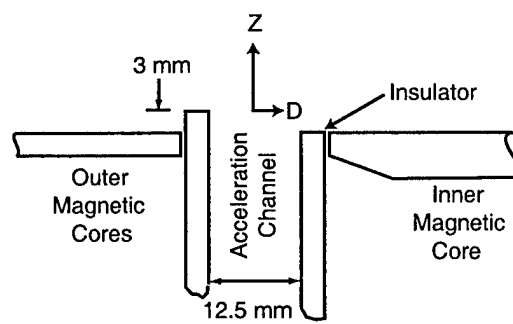


Fig. 6.

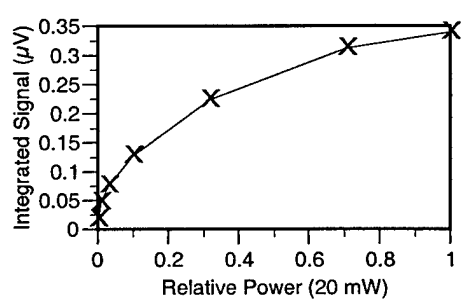


Fig. 7.

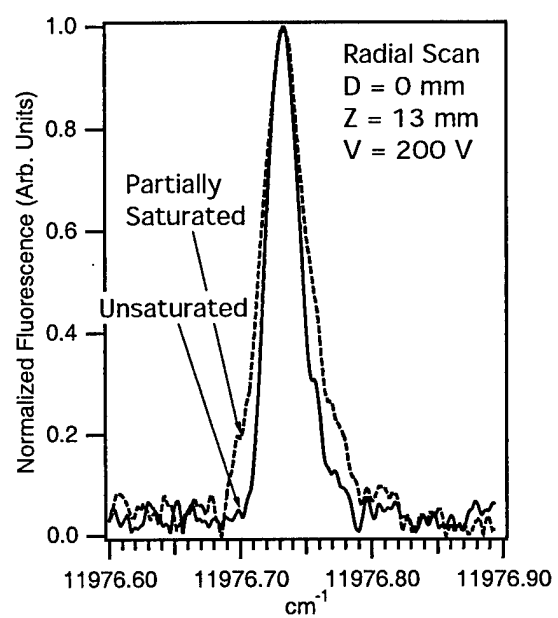


Fig. 8.

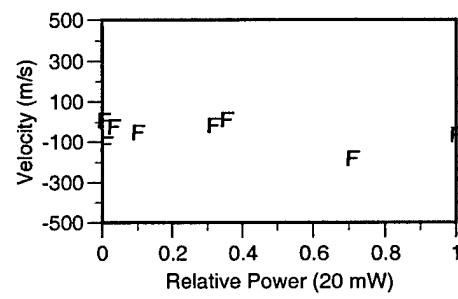


Fig. 9.

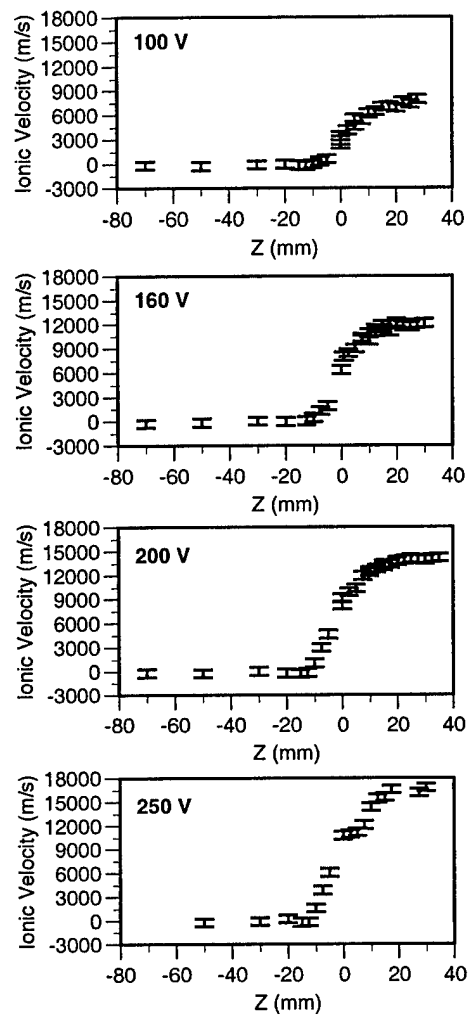


Fig. 10.

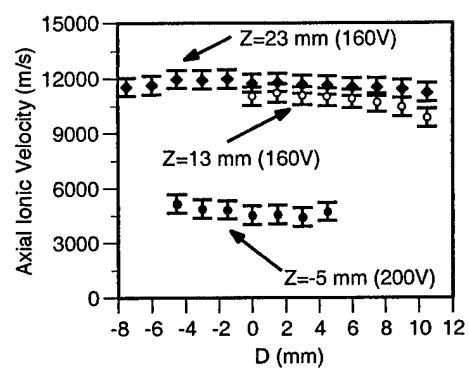


Fig. 11.

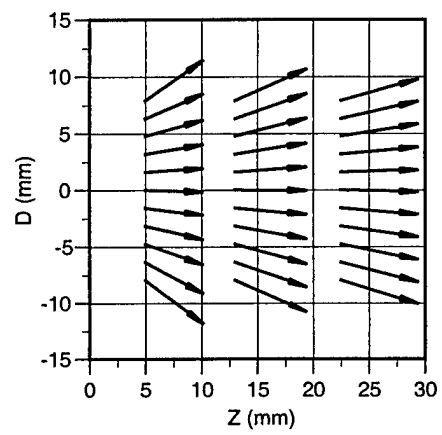


Fig. 12.

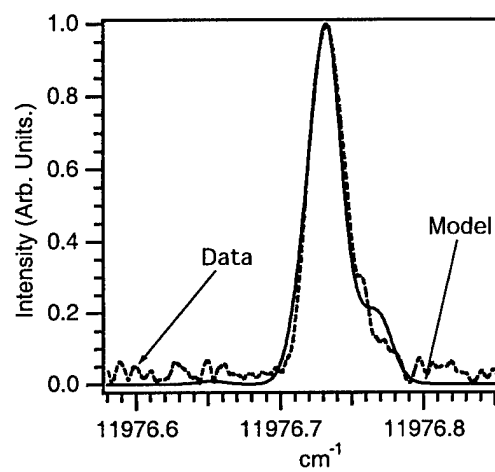


Fig. 13

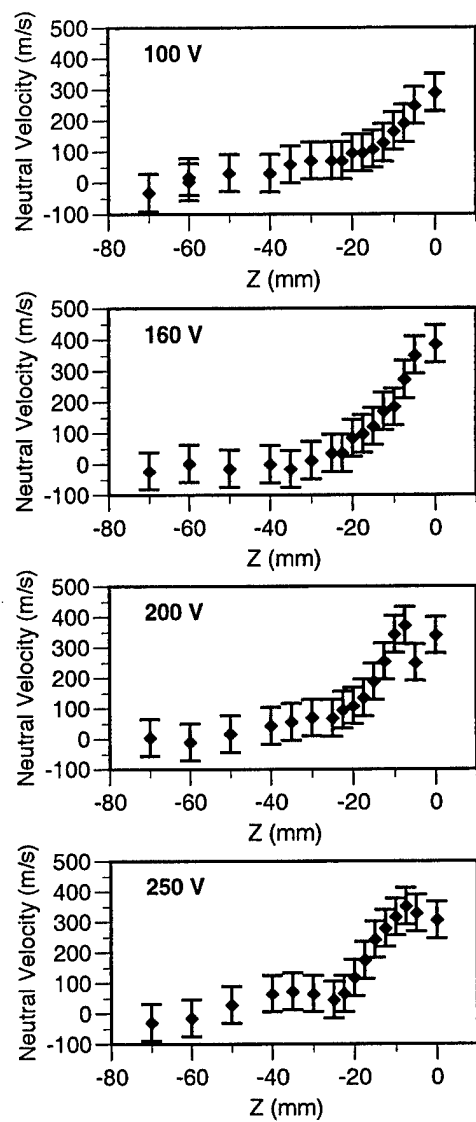


Fig. 14.

Appendix II

The Anomalous Electron Mobility in a Coaxial Hall Discharge Plasma

N.B. Meezan, W.A. Hargus, Jr., and M.A. Cappelli
Phys. Rev. E **63**, 026410, 2001.

Anomalous electron mobility in a coaxial Hall discharge plasma

Nathan B. Meezan, William A. Hargus, Jr., and Mark A. Cappelli

Mechanical Engineering Department, Stanford University, Stanford, California 94305-3032

(Received 12 June 2000; published 24 January 2001)

A comprehensive analysis of measurements supporting the presence of anomalous cross-field electron mobility in Hall plasma accelerators is presented. Nonintrusive laser-induced fluorescence measurements of neutral xenon and ionized xenon velocities, and various electrostatic probe diagnostic measurements are used to locally determine the effective electron Hall parameter inside the accelerator channel. These values are then compared to the classical (collision-driven) Hall parameters expected for a quiescent magnetized plasma. The results indicate that in the vicinity of the anode, where there are fewer plasma instabilities, the electron-transport mechanism is likely elastic collisions with the background neutral xenon. However, we find that in the vicinity of the discharge channel exit, where the magnetic field is the strongest and where there are intense fluctuations in the plasma properties, the inferred Hall parameter departs from the classical value, and is close to the Bohm value of $(\omega_{ce}\tau)_{\text{eff}} \approx 16$. These results are used to support a simple model for the Hall parameter that is based on the scalar addition of the electron collision frequencies (elastic collision induced plus fluctuation induced), as proposed by Boeuf and Garrigues [J. Appl. Phys. **84**, 3541 (1998)]. The results also draw attention to the possible role of fluctuations in enhancing electron transport in regions where the electrons are highly magnetized.

DOI: 10.1103/PhysRevE.63.026410

PACS number(s): 52.25.Fi, 52.75.Di, 52.70.Ds, 52.70.Kz

I. INTRODUCTION

The use of coaxial Hall discharges as high specific impulse plasma accelerators for satellite propulsion date back to the early 1960's. In a Hall discharge (Fig. 1), the plasma is sustained in imposed orthogonal electric and magnetic fields. The discharge electrons, a large fraction of which are emitted by an external cathode, are magnetized, whereas the more massive propellant ions, usually xenon, are not. Consequently, the electrostatic fields established by the retarded electron flow accelerate the ions to high velocities, typically 50%–60% of the discharge voltage. In a coaxial geometry, the electrons are constrained to move in the closed, azimuthal $\mathbf{E} \times \mathbf{B}$ drift, with cross-field diffusion providing the necessary current to sustain the discharge.

The first detailed investigation of the properties of these coaxial Hall discharges suggested that the axial electron current density is greater than that expected by classical transport [1]. This led to the first speculation of the presence of an “anomalous” cross-field drift of electrons, due in part to fluctuations in the electric field and plasma density. Fluctuations in the external circuit and plasma properties in these devices are now well documented [2–5], and recent numerical simulations of Hall discharges generally require the *ad hoc* introduction of an anomalous electron mobility to produce reasonably accurate results [6–9]. Despite many experimental and theoretical studies, the precise nature of the instabilities responsible for these fluctuations and the mechanism for their excitation are not yet well understood. Furthermore, other mechanisms, including collisions between energetic electrons and the channel wall, and experimental facility effects such as background gas ingestion may also play important roles in electron transport.

In this paper, we examine the electron-transport mechanism in a coaxial Hall discharge through a collection of applied diagnostics that serve to map the electron mobility in

the discharge channel. The two-dimensional electron momentum equation for a weakly ionized plasma gives the electron current density,

$$J_{ez} = en_e u_{ez} = en_e \left(\frac{E_z}{B_r} \right) \frac{\nu_{ne}}{\omega_{ce}} = en_e \left(\frac{E_z}{B_r} \right) \frac{1}{\omega_{ce} \tau}. \quad (1)$$

Here, n_e is the electron density, u_{ez} is the electron drift velocity, ν_{ne} is the momentum-transfer collision frequency for neutral-electron collisions, τ is the mean time between collisions, and the electron cyclotron frequency $\omega_{ce} \gg \nu_{ne}$. It is assumed that the applied electric field E_z and magnetic field strength B_r are in the axial and radial directions, respec-

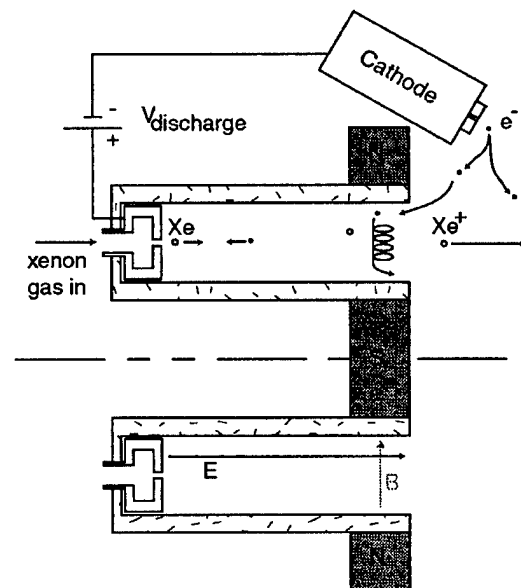


FIG. 1. Schematic of a typical Hall discharge accelerator.

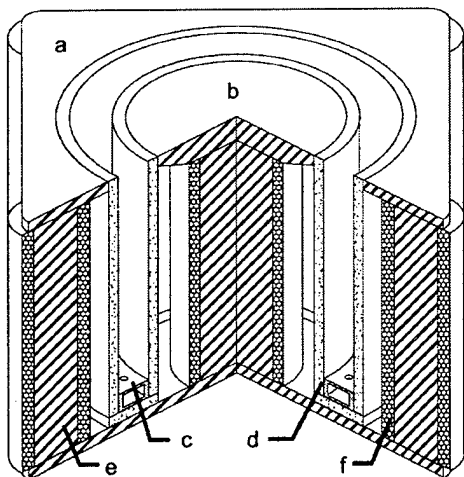


FIG. 2. Cutaway schematic of the Hall discharge studied. (a) Front magnetic plate; (b) central magnetic plate; (c) anode gas input; (d) alumina insulator wall; (e) magnet core; and (f) magnetic windings.

tively. From Eq. (1), we see that the cross-field electron mobility is inversely proportional to the electron Hall parameter, $\omega_{ce}\tau$,

$$\mu_{ez} = \left(\frac{1}{B_r} \right) \frac{1}{\omega_{ce}\tau}. \quad (2)$$

Equation (1) can be rearranged to give

$$\frac{1}{(\omega_{ce}\tau)} = \left(\frac{B_r}{E_z} \right) \frac{J_{ez}}{en_e}. \quad (3)$$

The Hall parameter (or electron mobility) can therefore be determined at any point in the discharge channel where the plasma properties on the right-hand side of Eq. (3) are known. Furthermore, the resulting Hall parameter can be compared to that calculated on the basis of known properties that independently determine the electron cyclotron frequency and the mean time between electron collisions. In this paper, we review our recent experimental measurements of plasma properties within the discharge channel, which permit this direct comparison. The results support the presence of an anomalous transport mechanism in regions of the plasma known to support fluctuations, and provide the first direct quantitative measure of the axial variation in the electron mobility.

II. EXPERIMENTS

A. Prototype Hall discharge

The Hall plasma source studied here was constructed at Stanford as a test bed for studying the discharge physics and is not intended to serve as an operational prototype plasma accelerator. A cutaway schematic of the plasma source is shown in Fig. 2. The source consists of an annular alumina channel 90 mm in diameter, 11 mm in width, and 80 mm in length. A magnetic circuit consisting of four outer coils, one

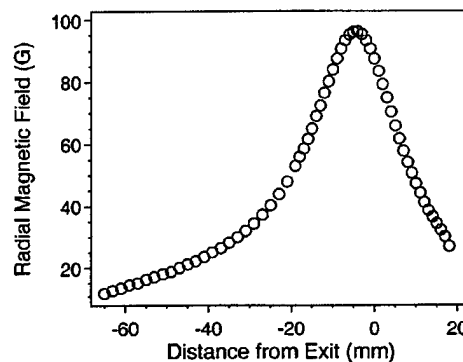


FIG. 3. Axial profile of radial magnetic-field strength for the Hall discharge studied.

inner coil, and three iron plates provides a magnetic field (mostly radial in direction) peaked near the exit of the discharge channel, as shown in Fig. 3. A hollow stainless-steel ring with 32 holes of 0.5-mm diameter serves both as the anode and the propellant (gas) input of the discharge.

A commercial hollow cathode (Ion Tech HCN-252) is used to neutralize the resulting ion beam and support the necessary electric field. The cathode is mounted approximately 2 cm downstream of the plasma source exit. The cathode body was kept at the vacuum chamber ground potential. To allow optical and probe access inside the discharge channel, a 1 mm wide slot was cut along the outer insulator wall, parallel to the discharge axis. The performance of the discharge is not noticeably altered by the presence of the slot.

Two independent mass flow controllers control the gas flow to the anode and cathode. Direct current power supplies are used to independently power the discharge, cathode heater, cathode keeper, and magnetic windings. The discharge (anode) power supply is always operated in the voltage-regulated limit. The experimental facility consists of a nonmagnetic stainless-steel tank approximately 1 m in diameter and 1.5 m in length pumped by two 50-cm diameter diffusion pumps and backed by a 425 L/s mechanical pump. The facility is equipped with several viewports and feedthroughs for optical and probe access to the discharge. The base pressure of the facility with no gas flow is approximately 10^{-6} Torr as measured by an ionization gauge uncorrected for gas species. The background pressure during discharge operation at a xenon flow rate of 2.3 mg/s is typically 10^{-4} Torr. Although this pressure is an order of magnitude lower than that of Janes and Lowder [1], it is still considerably higher than chamber pressures that are generally acceptable for the collection of accelerator performance data [10,11]. The ingestion of background gas near the exit of the discharge channel may influence the discharge characteristics.

B. Plasma diagnostic techniques

A variety of optical and probe diagnostics were utilized to measure the plasma properties needed for the determination of the effective Hall parameter [using Eq. (3)]. The potential distribution in the discharge was measured using an emissive

probe. This technique is described in more detail in another paper [12], and is only briefly summarized here. A tungsten filament inserted into the discharge channel was heated using a variable-current alternating current (ac) power supply and a second, floating step-down transformer. The filament current was increased until the potential of the floating transformer with respect to ground reached a nearly saturated value. This value was taken as the plasma potential [13]. This method of finding the plasma potential is less accurate than the more common "inflection point" method [14]; however, this alternative method involves the collection of electron current by the probe. Due to the small size of the discharge channel, it has been our experience that collecting electrons from the plasma can severely perturb the operation of the discharge. A probe collecting electron current causes a much greater disturbance on discharge performance than a floating probe or one collecting ion current. The floating potential of the plasma was also recorded at each point using the same probe without current passing through the filament. The magnetic-field distribution inside the channel was measured with the discharge off using a Hall effect sensor probe.

The electron current density is determined from the total discharge current density (discharge current divided by the channel cross sectional area) less the ion current density:

$$J_{ez} = I/A_{\text{channel}} - n_e V_i. \quad (4)$$

The ion current density is determined either directly using a guarded ion flux probe, or from a measurement of the electron (ion) density using a cylindrical Langmuir probe (discussed below) and from laser-induced fluorescence (LIF) measurements of the xenon ion velocity. These LIF measurements are described in detail elsewhere [12,15]. They involve propagating a narrow-linewidth, continuous-wave laser beam through the plasma along the discharge axis and measuring the fluorescence signal as a function of laser frequency. Due to the Doppler effect, the absorption line center is shifted from that of a stationary plasma reference. The bulk velocity of the absorbing xenon ions can then be determined from this frequency shift. In the studies reported here, a Coherent 899-21 tunable titanium sapphire laser was used to excite the $5d[4]_{7/2} - 6p[3]_{5/2}$ transition in Xe II at 834.7 nm, with nonresonance fluorescence detected at 541.9 nm. A similar method was also used to measure the velocity of excited neutral xenon atoms using the $6s[\frac{3}{2}]_2^0 - 6p[\frac{3}{2}]_2$ transition at 823.2 nm, only in this case, resonance fluorescence is detected. The neutral atom velocity together with the overall xenon mass flow rate served to provide a measure of the neutral xenon number density, from which the classical Hall parameter can be determined.

The electron density in the discharge was measured using two different techniques. In the first set of experiments, a cylindrical Langmuir probe was inserted into the discharge channel through the optical access slot. The probe was a 0.5-mm diameter tungsten wire bent at a right angle so that a 5-mm length of the probe was parallel to the ion flow in the channel. The ion-saturation current was collected at a probe bias of -46 V and the electron (ion) density was determined using a thin ("free-fall") sheath approximation [16] for ion

collection. This required an estimate of the electron temperature, as described below. Inserting the probe through the access slot minimized its disturbance of the plasma, but also prevented measurements near the exit of the discharge.

Shortcomings of this probe characterization method included spatial averaging along the length of the probe, "shadowing" of the backside of the probe due to wake formation, and the use of a relatively simple ion current collection theory for a high-velocity plasma in the presence of a magnetic field. The effects of the magnetic field on particle collection by the probe can be measured through the electron and ionic Larmor radii. For the Hall discharge, $r_e \approx a$ and $r_i \gg w \gg a$, where r_e and r_i are the electronic and ionic Larmor radii, a is the probe radius, and w is the channel width. While electron collection will be affected by the magnetic field, the ions are essentially not magnetized. Therefore, as pointed out by Batani *et al.* [17], the effect of the magnetic field on a measurement of the electron density from the ion current will be negligible compared to the 20% accuracy expected by this probe theory. Ideally, the entire Langmuir probe trace would be used for determining the electron temperature, plasma density, and plasma potential. As mentioned above, scanning the probe voltage into the electron-collection region is not desirable in this discharge, as it may strongly perturb the plasma, and requires an appropriate theoretical treatment of probe traces when electrons are strongly magnetized.

As mentioned above, the ion current density is also determined directly using a guarded ion-flux probe [18]. The ion (hence electron) density can be determined from these probe measurements and the measurements of the ion velocity. The ion probe was constructed of 1.5-mm diameter tungsten rod surrounded by an alumina sleeve. A tantalum guard ring biased to the same potential as the probe was mounted around the center probe to establish a one-dimensional sheath across the probe collection area, and to minimize outer sheath collection area growth with probe bias. At all locations within the discharge, the probe was biased at 20 V below the local floating potential. It is noted, however, that inserting the probe into the discharge channel caused a significant increase in the total discharge current, up to 20%. The intrusive perturbation of this probe precluded measurements upstream of the discharge exit plane.

Measurements of plasma fluctuations were also made to give insight into the role of oscillations in electron transport. Low-impedance shielded Langmuir probes were used to measure fluctuations in ion-saturation current, which roughly correspond to fluctuations in plasma density. These probes were designed to detect propagating plasma waves in the Hall discharge, experiments described in great detail in another paper [19]. For this experiment, one probe was connected to a direct current (dc) coupled digital oscilloscope through a 50 Ω terminator. Due to the high floating potential inside the discharge, this grounded probe collected current in the ion-saturation regime of the Langmuir probe trace.

III. RESULTS AND ANALYSIS

The plasma potential profiles as measured by the hot-filament probe are shown in Fig. 4 for the three operating

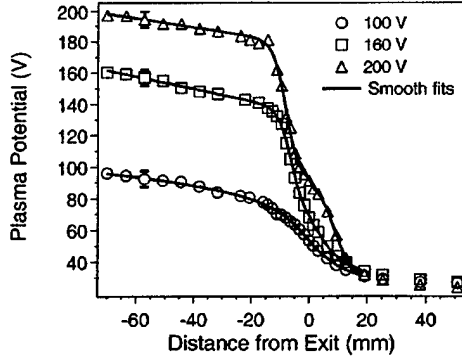


FIG. 4. Plasma potential profiles measured by the emissive probe.

conditions investigated in this paper. The floating potential of an emitting probe should be slightly below the actual plasma potential, since the emission will never be enough to neutralize the sheath [14]. It can be seen from Fig. 4 that as the probe approaches the anode, the measured plasma potential comes quite close to the applied anode potential. With the probe 5 mm away from the anode, the measured values are within 4 V of the applied potential, suggesting that the uncertainty in the measured potential is within 5 V, and possibly less, depending on the strength of the anode fall. The electric field inside the discharge channel, shown in Fig. 5, was calculated from the plasma potential data using the relation $E_z = -d\phi/dz$. Smooth curves were fit to the potential profiles before differentiation to prevent noise amplification. It is noteworthy that the peak in the electric field coincides closely with the peak in the magnetic field, although the distribution is more narrow, suggesting that the electron $\mathbf{E} \times \mathbf{B}$ drift velocity, $u_d = E_z/B_r$, is also highly peaked near $z = -10$ mm.

The plasma potential data was used in conjunction with floating potential data (not shown) to calculate the electron temperature:

$$\phi_p - \phi_f = \frac{kT_e}{2e} \ln \left(\frac{m_i}{2\pi m_e} \right). \quad (5)$$

Here, we assume that the ions enter the sheath at the Bohm velocity.

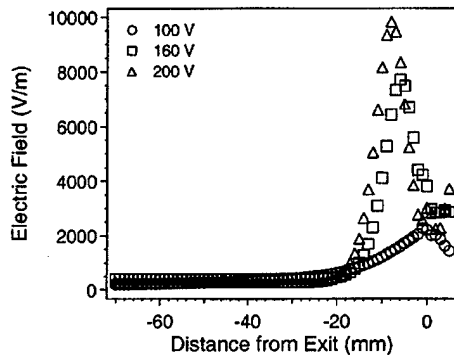


FIG. 5. Electric-field profiles calculated from plasma potential.

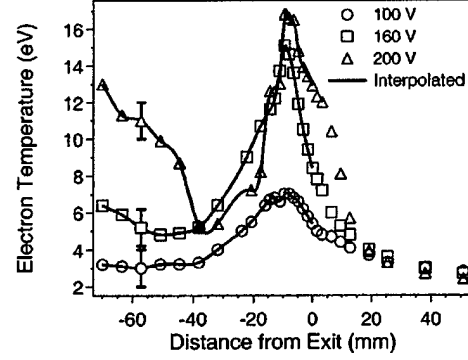


FIG. 6. Electron temperature profiles calculated from plasma and floating potential data.

The electron temperature is shown in Fig. 6. These temperature profiles are used in the remaining calculations needed to estimate the Hall parameter. The electron temperature is seen to peak above 16 eV. Although the temperature could be in error by a few volts due to underestimation of the plasma potential, the measured values do agree well with those from other investigators in similar discharges [20,21]. The peak in the electron temperature is coincident with the peaks in the electric and magnetic fields, as expected since the Ohmic dissipation will scale as $J_{ez}E_z$. We see an unexpected rise in the electron temperature near the anode for the higher power cases studied, most likely due to the formation of an anode glow region, as the production of electrons is needed in this region to support the higher current densities. These striking distributions suggest that the discharge length is not optimized, and can be shortened to 40 mm for more efficient operation as a plasma accelerator at the higher-voltage conditions.

The electron temperature is used to determine the electron (ion) density from the ion saturation current collected with the Langmuir probe discussed above,

$$J_{is} = 0.61en_e \sqrt{\frac{kT_e}{m_i}}. \quad (6)$$

The electron-density profiles measured from the two probe methods are plotted together in Fig. 7. As mentioned above, the error in the electron temperature will have a small impact on this measurement. For example, an error as large as 2 eV

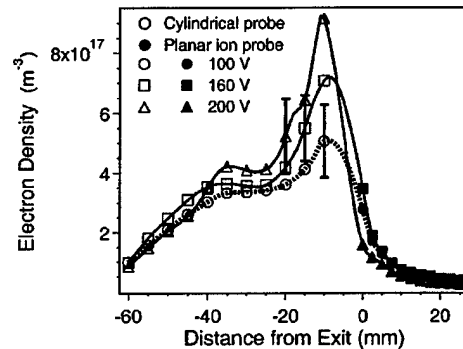


FIG. 7. Electron-density profiles from probe experiments.

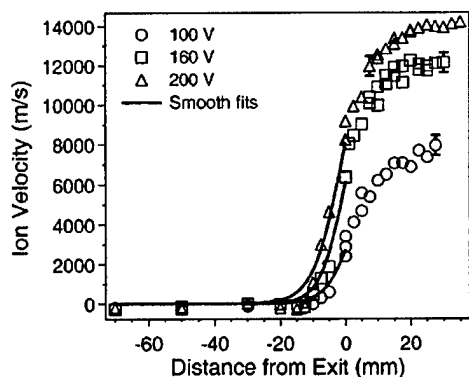


FIG. 8. Ion velocity profiles measured by laser-induced fluorescence velocimetry.

in a measured electron temperature of 6 eV will lead to an error of 15%–20% in the electron density—within the expected accuracy of the method.

The intrusive nature of the guarded ion probe precluded measurements with this probe within the discharge channel. Furthermore, the Langmuir probe inserted through the slot in the insulator was unable to collect data within a distance of 10 mm upstream of the channel exit, because of the presence of the magnetic pole piece. As a result, the two probe measurements were indeed complementary, and a cubic-spline interpolation was used to estimate the plasma density in the range between the discharge channel exit and the location of the base of the front magnetic plate. The resultant spline fits are also shown in Fig. 7. The electron number densities are seen to peak in the same vicinity where the other plasma properties reach their maximum values. The error in the electron-density measurement inside the channel is quite significant, but it is also bound. The values have an upper bound of 100% propellant utilization (i.e., the ion flow leaving the channel equals the mass flow entering the channel), and the ion-flux measurements effectively provide a lower bound on the density near the exit plane.

The ion velocity profiles measured using LIF are shown in Fig. 8. Just downstream of the high-temperature ionization region, the produced ions are seen to accelerate to high velocities consistent with the measured plasma potential distributions.

The data given above for B_r , E_z , n_e , and V_i (ion velocity) is enough to calculate the effective Hall parameter along the Hall discharge channel from Eqs. (3) and (4). This Hall parameter can be compared to the “classical” Hall parameter expected based on the electron momentum-transfer collision frequency ν_{ne} . For this calculation, the neutral gas density (the dominant electron collision partner) is determined from the neutral xenon velocity data, shown in Fig. 9, and the discharge mass flow rate,

$$n_g = \left(\frac{\dot{m}}{m_i A_{\text{channel}}} - n_e V_i \right) \frac{1}{V_n}. \quad (7)$$

The axial variation in the inferred neutral density is shown in Fig. 10.

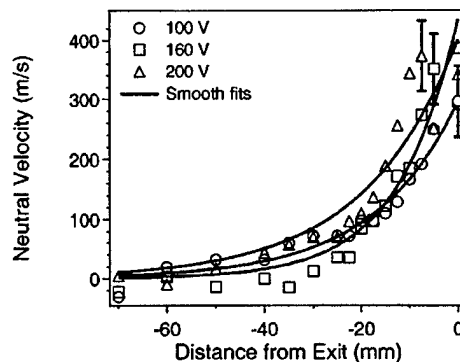


FIG. 9. Neutral xenon velocity profiles measured by laser-induced fluorescence velocimetry.

The dip in the neutral density near the exit plane at higher discharge voltages is due to the measurement of a significant increase in the ion flux, reflecting the ionization process taking place between $z = -5$ and as -10 mm. It is noteworthy that the calculation of the neutral gas density does not take ingestion of background gas from the vacuum chamber into account. Background chamber neutral xenon ingestion would cause an underestimate of the neutral xenon density, as the actual mass flow rate would be higher. These measurements of xenon density should be interpreted as lower limits on the actual values.

The electron momentum-transfer collision frequency was calculated using the cross section given in the SIGLO® database [22] assuming a Maxwellian electron energy distribution, using the electron temperature measurements described above.

IV. DISCUSSION

The deduced Hall parameter is compared to the “classical” Hall parameter (that determined by the direct calculation of the electron momentum-transfer collision frequency), in Fig. 11. In the figure, we plot the inverse of the Hall parameter ($1/\omega_{ce}\tau$), since this is proportional to the electron cross-field mobility [see Eq. (2)].

It is apparent from Fig. 11 that elastic electron-neutral collisions are the likely mechanisms for cross-field electron transport at locations between the anode ($z = -80$ mm) and

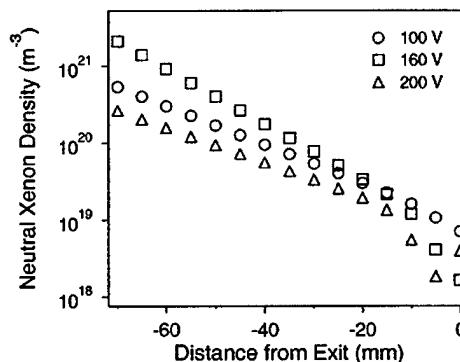


FIG. 10. Neutral xenon density profiles.

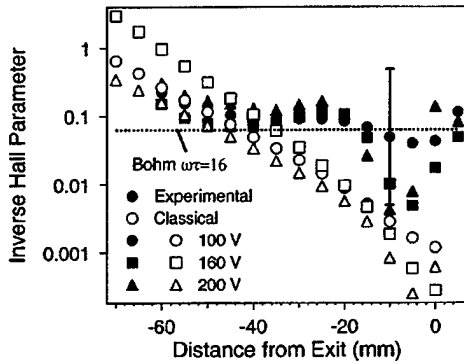


FIG. 11. Effective and classical inverse Hall parameter profiles inside Hall discharge channel.

approximately 40 mm upstream of the discharge channel exit. It is noteworthy that this location is where the magnetic-field strength reaches approximately 1/5th of its peak value (see Fig. 3). We also see that beyond this location, there is a striking departure from this classical value, although the uncertainty in the absolute measurements is still significant, a result mainly attributable to the uncertainty in the total discharge current caused by the intrusive nature of the diagnostic probes. At locations downstream of the $z = -40$ mm position, where the magnetic field reaches a maximum, the inverse Hall parameter is in remarkable agreement with the Bohm value of $\omega_{ce}\tau = 16$ [23]. In this region, we [24–28], and others [2–5,29–32] have reported on the existence of intense fluctuations in the plasma properties. These results are supportive of the conjecture that plasma fluctuations are partially responsible for the anomalous cross-field transport, although additional experiments may be necessary to obtain more accurate quantitative measurements of the resulting mobility. The results reported on here do, however, provide the first direct support of a model based on the use of a “mixed” mobility (or collision frequency),

$$\left(\frac{1}{\omega_{ce}\tau}\right)_{\text{total}} = \left(\frac{1}{\omega_{ce}\tau}\right)_{\text{collisions}} + \left(\frac{1}{\omega_{ce}\tau}\right)_{\text{oscillations}}, \quad (8)$$

as has been originally proposed by Boeuf and Garrigues for numerical simulations of Hall discharges [7]. The Bohm

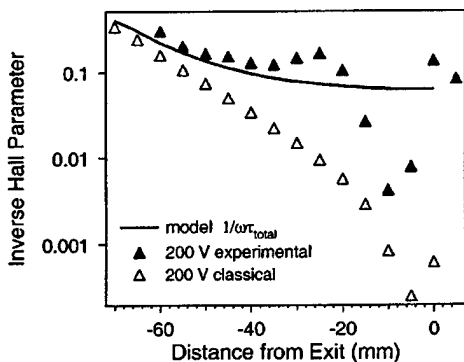


FIG. 12. Comparison of mixed mobility model to experimental and classical inverse Hall parameter profiles at 200 V operation.

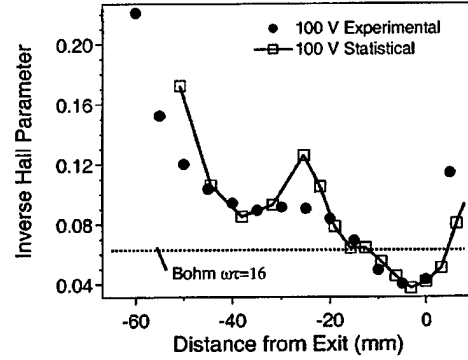


FIG. 13. Comparison of statistical fluctuation analysis to experimental inverse Hall parameter profile at 100 V operation.

value appears to be reasonable for the oscillation-induced part of the mobility (Fig. 12), despite the lack of a full understanding of the instabilities in this region of the plasma.

Additional support for the conjecture that oscillations are at least partly responsible for the enhanced cross-field mobility can be found in statistical analysis of probe fluctuation data. For a homogeneous plasma subjected to homogeneous turbulent fluctuations in the plasma density, the cross-field electron diffusion coefficient (which is directly proportional to the inverse of the effective Hall parameter) can be expressed as [33]

$$D_{\perp} \propto \frac{1}{(\omega\tau)_{\text{eff}}} = \frac{\pi}{4} \left[\frac{(\langle n_e - \langle n_e \rangle)^2}{\langle n_e \rangle^2} \right]. \quad (9)$$

The quantity inside the square brackets is the mean-square deviation of the observed plasma density fluctuation. As mentioned above, the raw fluctuation data collected by an ion-current probe is proportional to the local plasma density. Equation (9) was therefore applied directly to the raw probe data inside the discharge channel. This “statistical Hall parameter” is compared to the experimental value in Fig. 13. The agreement is remarkable, although the uncertainty in the measured value of the Hall parameter is large. More significantly, the trend in the mean-square deviation of the plasma density follows the experimental value very closely, suggesting that the role of fluctuations may be important.

The relatively large error bars in Fig. 11 are a consequence of the number of different data used to calculate the Hall parameter. The largest source of error is the measurement of the total current through the discharge. At a given voltage, the current through the discharge used in this study can drift up to 10% in a half hour, presumably due to fluctuations in the facility background pressure. Furthermore, the insertion of the ion and/or Langmuir probe gives rise to a perturbation that can be as high as 20% on the total discharge current. An alternate, nonintrusive measurement of the electron density is favored, and is the subject of our present research. Efforts will also be made to reduce the perturbation caused by the emissive potential probe.

V. CONCLUSIONS

In this paper, we have used a variety of plasma diagnostic techniques, both intrusive and nonintrusive, to evaluate the effective electron mobility in a Hall discharge. We provide strong evidence of the presence of an anomalous transport mechanism, in the region of the plasma where there is a strong radial magnetic field, and where we have seen intense plasma fluctuations. The Hall parameter has been shown to approach a constant value, within the margin of error, near the Bohm value of 16 in this region. Although these results fall short of identifying fluctuations in plasma density and/or temperature as the source of this enhanced cross-field electron mobility, they do suggest that fluctuations in plasma properties can account for the observed axial electron current flow. The Hall discharge accelerator falls within a difficult regime for plasma diagnostics—the device is small, low-density, fluctuating, and magnetized, making it difficult to interpret probe-based measurements of electron density using available probe theory. Furthermore, although the electron-density measurements themselves are not the largest source of uncertainty, we find that the probes used for these measurements have a weak perturbing effect on the total dis-

charge current, which does strongly contribute to the measurement accuracy. Future studies will focus on the development of nonintrusive measurements of plasma density to improve the measurement accuracy.

The most significant finding is that the results are in remarkable agreement with a simple model for the Hall parameter that is based on the scalar addition of the electron collision frequencies (elastic collision induced plus fluctuation induced), as first proposed by Boeuf and Garrigues [7]. The transition from a fluctuation-dominated mobility (Bohm-like) to collision induced mobility is found to occur at the point where the magnetic field is approximately 20% of its peak value, and where our other studies [19,28] identify the spatial onset of strong, quasicohherent azimuthally propagating waves in plasma density and potential.

ACKNOWLEDGMENTS

This work was supported by the Air Force Office of Scientific Research. W. Hargus Jr. was supported by the Air Force Palace Knight Program. The authors acknowledge the technical assistance of D. P. Schmidt.

-
- [1] G. S. Janes and R. S. Lowder, *Phys. Fluids* **9**, 1115 (1966).
 - [2] A. I. Morozov *et al.*, *Zh. Tekh. Fiz.* **42**, 612 (1972) [*Sov. Phys. Tech. Phys.* **17**, 482 (1972)].
 - [3] Y. B. Esipchuk *et al.*, *Zh. Tekh. Fiz.* **43**, 1466 (1973) [*Sov. Phys. Tech. Phys.* **18**, 928 (1973)].
 - [4] E. Y. Choueiri, AIAA Paper No. 94-3013, *30th Joint Propulsion Conference, Indianapolis, IN, 1994* (American Institute of Aeronautics and Astronautics, Washington, DC, 1994).
 - [5] G. Guerrini and C. Michaut, *Phys. Plasmas* **6**, 343 (1999).
 - [6] J. Fife and M. Martinez-Sanchez, AIAA Paper No. 96-3197, *32nd Joint Propulsion Conference, Lake Buena Vista, FL, 1996*.
 - [7] J. P. Boeuf and L. Garrigues, *J. Appl. Phys.* **84**, 3541 (1998).
 - [8] J. J. Szabo, Jr. and M. Martinez-Sanchez, AIAA Paper No. 98-3795, *34th Joint Propulsion Conference, Cleveland, OH, 1998*.
 - [9] E. Ahedo and M. Martinez-Sanchez, AIAA Paper No. 98-3788, *34th Joint Propulsion Conference, Cleveland, OH, 1998*.
 - [10] T. Randolph *et al.*, IEPAC Paper No. 93-093, *23rd International Electric Propulsion Conference, Seattle WA, 1993*.
 - [11] S. C. Bechu *et al.*, AIAA Paper No. 99-2567, *35th Joint Propulsion Conference, Los Angeles, CA, 1999*.
 - [12] W. A. Hargus, Jr. and M. A. Cappelli, AIAA Paper No. 99-2721, *35th Joint Propulsion Conference, Los Angeles, CA, 1999*.
 - [13] F. F. Chen, in *Plasma Diagnostic Techniques*, edited by R. H. Huddleston and S. L. Leonard (Academic, New York, 1965), Chap. 4, p. 184.
 - [14] J. R. Smith, N. Hershkowitz, and P. Coakley, *Rev. Sci. Instrum.* **50**, 210 (1979).
 - [15] R. J. Cedolin, W. A. Hargus, Jr., and M. A. Cappelli, *Appl. Phys. B: Photophys. Laser Chem.* **65**, 459 (1997).
 - [16] A. Lieberman and A. J. Lichtenberg, *Principles of Plasma Discharges and Materials Processing* (Wiley, New York, 1994), p. 174.
 - [17] D. Batani *et al.*, *Rev. Sci. Instrum.* **68**, 4043 (1997).
 - [18] G. S. Janes and J. P. Dotson, *Rev. Sci. Instrum.* **8**, 284 (1964).
 - [19] E. Chesta *et al.* (unpublished).
 - [20] M. Bishaev and V. Kim, *Zh. Tekh. Fiz.* **48**, 1853 (1978) [*Sov. Phys. Tech. Phys.* **23**, 1055 (1978)].
 - [21] A. I. Bugrova *et al.*, *Teplofiz. Vys. Temp.* **19**, 1149 (1981) [*High Temp.* **19**, 822 (1981)].
 - [22] CPAT and Kinema Software, www.csn.net/siglo (1998).
 - [23] D. Bohm, in *The Characteristics of Electrical Discharges in Magnetic Fields*, edited by A. Guthrie and R. K. Wakerling (McGraw-Hill, New York, 1949), Chap. 2, p. 65.
 - [24] M. A. Cappelli, W. A. Hargus, Jr., and N. B. Meezan, *IEEE Trans. Plasma Sci.* **27**, 96 (1999).
 - [25] N. B. Meezan and M. A. Cappelli, AIAA Paper No. 98-3502, *34th Joint Propulsion Conference, Cleveland, OH, 1998*.
 - [26] N. B. Meezan and M. A. Cappelli, AIAA Paper No. 99-2284, *35th Joint Propulsion Conference, Los Angeles, CA, 1999*.
 - [27] D. P. Schmidt, N. B. Meezan, and M. A. Cappelli, AIAA Paper No. 99-3437, *30th Plasmadynamics and Lasers Conference, Norfolk, VA, 1999*.
 - [28] E. Chesta, N. B. Meezan, and M. A. Cappelli (unpublished).
 - [29] F. Darnon *et al.*, *IEEE Trans. Plasma Sci.* **27**, 98 (1999).
 - [30] N. Gascon *et al.*, AIAA Paper No. 99-2427, *35th Joint Propulsion Conference, Los Angeles, CA, 1999*.
 - [31] D. Pagnon *et al.*, AIAA Paper No. 99-2428, *35th Joint Propulsion Conference, Los Angeles, CA, 1999*.
 - [32] G. Guerrini and C. Michaut, *Phys. Plasmas* **6**, 343 (1999).
 - [33] S. Yoshikawa and D. J. Rose, *Phys. Fluids* **5**, 334 (1962).

Appendix III

A Characterization of Plasma Fluctuations within a Hall Discharge

E. Chesta, C. Lam, N.B. Meezan, D.P. Schmidt, and M.A. Cappelli

To appear in *IEEE Transactions on Plasma Science*, 2001

A Characterization of Plasma Fluctuations within a Hall Discharge

Enrico Chesta, Cheryl Lam, Nathan B. Meezan, Dan P. Schmidt, and Mark A. Cappelli*

Thermosciences Division

Mechanical Engineering Department

Stanford University

Stanford, California 94305-3032

Abstract

Experimental results are presented for studies of low (2-20 kHz) and intermediate-frequency (20-100 kHz) oscillations in crossed-field closed-electron drift Hall discharges. Conditional sampling using two electrostatic probes is used to identify and extract properties of coherent structures associated with the propagation of azimuthal and longitudinal instabilities within the discharge channel. The azimuthal component phase velocities are determined for a wide range of wave frequencies and over characteristic regimes of operation of these devices. A variety of propagation modes are observed and analyzed, including the appearance of an induced mode due to the presence of the probes themselves. This latter result is believed to be the first direct evidence of how fluctuations can be influenced in these Hall discharges using relatively simple actuation methods.

Index Terms - Hall discharges, Langmuir probes, plasma propulsion, plasma instabilities.

*Author to whom correspondence should be sent.

Submitted to IEEE Transactions on Plasma Sciences, August 2000. Revised, January 2001.

I. INTRODUCTION

Closed electron-drift Hall discharges are low-pressure ($\sim 0.01 - 0.1$ Pa), weakly collisional, magnetized plasma sources that generate a relatively high velocity ion beam suitable for use in space propulsion applications. A particular class of Hall plasma thrusters, the so-called "Stationary Plasma Thruster," has been used in a number of space missions in the former Soviet Union [1]. A variation of this Hall thruster that has an annular (co-axial) discharge channel 100 mm in diameter – the SPT-100, has a high specific impulse (1100 – 2000 sec), operates at moderately high thrust levels (55 – 150 mN), and has an exceptionally high thrust efficiency (40-60%). Because of this performance, this plasma source is now being aggressively developed for use in station keeping applications on western satellites.

In a typical co-axial geometry Hall discharge (Fig. 1), the plasma is sustained in imposed orthogonal electric and magnetic fields. The discharge electrons, a large fraction of which are emitted by an external cathode, are magnetized, whereas the more massive propellant ions, usually xenon, are not. Consequently, the electrostatic fields established by the retarded electron flow accelerate the ions to high velocities, typically 50-60% of the discharge voltage ($\sim 100-300$ V). The maximum acceleration occurs in the region between the magnetic poles, where the magnetic field is a maximum. In a co-axial geometry, the electrons are constrained to move in the closed, azimuthal $\mathbf{E} \times \mathbf{B}$ drift, with cross-field diffusion providing the necessary current to sustain the discharge. An annular ceramic channel confines the electron flow towards the anode, located at its base.

It is widely known that the Hall discharge plasmas exhibit a rich spectrum of fluctuations in plasma properties [2]. While it is not yet known if and how these fluctuations can impact the performance of a Hall thruster, it is believed that fluctuations in the bulk plasma properties are partly responsible for anomalous electron transport across the imposed magnetic field [3]. While some studies characterizing the presence and origin of these fluctuations and their possible control were published in the mid 60's to mid 70's [3-9], they have received increased attention recently [10-15], as there is a growing need to extend and enhance the performance of these thrusters for a broader range of space missions.

Our research is motivated by the possibility of enhancing Hall thruster operation by the active control of these fluctuations, or by the passive suppression of the fluctuations in regions of the discharge channel where a reduction in electron current is desired. To do so, it is important that the nature of these fluctuations is adequately understood. In this paper, we present an experimental

characterization of the propagation of these disturbances over a range of Hall discharge operation, and demonstrate that it is possible to affect the oscillations within the discharge by the insertion of biased probes.

II. EXPERIMENT

The Hall discharge plasma source used in this study is a laboratory version of a low-power Hall thruster, and is described in more detail in previous papers [16-18]. This particular source is intended to be used as a test bed for studying the discharge physics and not to serve as an operational prototype plasma accelerator, although the principal design is similar to that used in practise. The time-averaged plasma properties within the annular discharge channel have been extensively characterized for a range of operating conditions [16]. The source consists of an annular alumina channel, 90 mm in diameter, 11 mm in width, and 80 mm in length. A magnetic circuit consisting of four outer coils, one inner coil, and three iron plates provides a magnetic field (mostly radial in direction) peaked near the exit of the discharge channel, as shown in Fig. 2. The mapping of the axial and radial components of the magnetic field strength within the channel is performed with a Hall probe in the absence of the plasma. The radial component of the magnetic field is found to drop off by approximately 15% at the inner and outer walls of the acceleration channel. Details of the two-dimensional magnetic field distribution for magnet currents used here can be found in [18]. A hollow stainless steel ring with 32 holes of 0.5 mm diameter serves both as the anode and the propellant (gas) input of the discharge. A commercial hollow cathode (Ion Tech HCN-252) is used to neutralize the resulting ion beam and provide the necessary electron current to sustain the discharge. The cathode is mounted such that its exit aperture is approximately 2 cm downstream of the plasma source exit. The cathode body was kept at the vacuum chamber ground potential. During discharge operation, the 1 m diameter by 1.5 m long chamber within which the discharge was operated was maintained at a pressure of 10^{-4} Torr (uncorrected for xenon), as indicated by an ionization gauge. Flanged elbows (0.5 m in diameter) at each end of the vacuum chamber supported two 0.5 m diameter diffusion pumps, operated without baffles, for maximum pumping speed (approximately 6000 l/s).

For the measurements reported on here, the xenon flow rate was 2 mg/s and a constant solenoid winding current of 125 mA provided a peak magnetic induction of about 100 G at 5mm upstream of the exit plane (inside the channel). The characteristics of the plasma fluctuations on centerline within the channel were studied at various discharge potentials.

Plasma density fluctuations were detected by two azimuthally-placed low-impedance Langmuir probes biased negatively with respect to the plasma potential to collect the ion saturation current, with the current density given as [19]:

$$J_{is} = 0.61 \, e n_e \sqrt{\frac{kT_e}{m_i}} \quad (1)$$

Here, T_e is the electron temperature, n_e is the electron number density, m_i is the xenon ion mass, e is the electron charge, and k is the Boltzmann constant. In Eqn. 1, it is assumed that the distant plasma is quasi-neutral ($n_e = n_i$), and that the ions enter the collisionless sheath at the Bohm velocity. While the fluctuations in collected current can be a result of both fluctuations in electron density and temperature, in prior studies, it has been shown that these low frequency disturbances at low operating potential are largely isothermal [3, 7].

A schematic of the Langmuir probe construction is shown in Fig. 3. The exposed part of the probe consisted of a 0.254 mm diameter, 3 mm long tungsten wire. The base of the probe was of a complex design, intended to minimize stray capacitance for extended frequency response. The probe base consisted of an alumina tube directly surrounding the tungsten wire (0.508 mm ID, 1.27 mm OD), followed by a stainless steel tube (1.48 mm ID, 1.58 mm OD), connected to the braided ground of a 50 Ω co-axial cable. The inner tungsten wire was connected to the center pin of the co-axial cable. This outer stainless steel tubing served as a shield to isolate the extended probe base from disturbances other than at the tip of the probe. The stainless steel tubing was then surrounded by another alumina tube (1.6 mm ID, 2.3 mm OD) and the entire inside air spaces were potted with an alumina paste.

The probe size was minimized so as to reduce its overall capacitance, and for the studies reported on here, was approximately 10 cm in length. Coaxial transmission line feed-throughs provided the transfer of the probe signal through the vacuum chamber to a National Instruments DAQScope 5102 digital oscilloscope card operating at an 800 kHz sample rate. Data was stored on a personal computer for future processing. The probes were terminated with 50 Ω at the input of the oscilloscope card. In this way, the probe tips were negatively biased (close to system ground) with respect to the plasma, which is predominantly at high positive potential, since the anode is maintained at a minimum of 86V, and since the near exit plane potential is always greater than 40V due to the cathode fall and finite electron temperature. Occasional scans of the Langmuir probe

across the electron retarding regime to regions of high negative bias verified that system ground potential was always in the ion current saturation regime.

The probes were oriented such that the exposed center wire axis was parallel to the axial coordinate of the thruster, and placed midway between the inner and outer insulating walls, as illustrated in Fig.4. Probe translation along the axial direction (the direction of the annular channel) was provided by a translation stage driven by a Slo-Syn stepper motor, powered and controlled by a Compumotor model SX Microstepping Drive/Indexer System. The azimuthal positions of the two probes were manually set before the beginning of each experiment, maintaining an equal angular distance from the two nearest outer magnetic coils. For this study, probe separations between 30 and 180 degrees were examined. In most cases, the axial probe locations varied between a distance of approximately 35 mm from the anode ($x = -45$ mm) and 10 mm beyond the exit plane ($x = 10$ mm), with the $x = 0$ reference taken to be the exit plane of the discharge, and negative positions implying that the probe locations are inside the discharge channel.

A fast Fourier transform of the signal from each probe was performed across a temporal window that was 1.25 msec wide and spaced every 0.625 msec in time. This operation was used to convert the digital signal in the time domain into the frequency domain, for every temporal interval, over the length of the temporal data set (in some cases, 0.625 sec long). To study the fluctuating component to the signals, the mean signal was removed (numerically) from the transient signal prior to its processing. A comparison of the mean signals, and the power spectrum from each of the two probes verified that the probes had equal sensitivities (to within $\sim 10\%$) and frequency responses. To avoid aliasing, only frequencies below 400 kHz (the Nyquist frequency, defined by the 800 kHz sampling rate used for all of the studies described here) were considered for interpretation. In the future, higher sampling rates will be used to better explore higher instability frequencies, since most of the probes used here were found to have a 20dB cut-off of well beyond 1 MHz.

Typical current (I) – voltage (V) discharge characteristics, as monitored by digital multi-meters, for the flow rates and magnetic field strength used for these studies is shown in Fig. 5. In some cases, these mean values were verified by recording the discharge current oscillations with a differential amplifier placed across a 4-ohm ballast resistor in the anode circuit. At the higher discharge voltages (e.g., ~ 200 V), the probes were seen to clearly affect the mean discharge current, perturbing it by as much as 20-30%. During the collection of the data, the residence time of the probes within the channel was several minutes. Damage to the probes from ion bombardment

precluded the collection of data beyond approximately 185V. While it is difficult to say how the immersion of the probes into the plasma affected the spontaneous instabilities detected, we discuss later in the paper the clear presence of waves that are induced by the presence of the probes themselves within the discharge channel.

III. DATA ANALYSIS

The data collected by a single probe was cast to display three-dimensional renderings of the plasma density fluctuations, as shown in Figs. 6 and 7. The axial variation in the mean electron density for three operating conditions has been reported previously [16], and is provided again here for reference (Fig. 8). In Fig. 6, the amplitude of the plasma density fluctuations are displayed verses operating voltage, for four axial locations $x = 12.7$ mm, 0 mm, -12.7 mm, and -25.4 mm. Prominent in these figures is the presence of strong, relatively low frequency disturbances in the range of 5 – 30 kHz, and a broader range of disturbances towards higher frequencies, at very low voltages downstream of and at the exit plane, and at high voltages upstream of the exit plane. Similar spectral maps have been reported for the behavior of discharge current oscillations in the Russian Stationary Plasma Thruster SPT-70 [15].

In Fig. 7, the Fourier component amplitudes of the plasma density fluctuations and the ratios of the amplitudes to the mean are displayed verses axial position for a range of operating voltages. We find that the fluctuations in the plasma density can be as high as the mean values. While it is apparent that the fluctuations are most intense near the exit plane, it is noteworthy that the relative fluctuations (amplitude of the fluctuations divided by the mean value) actually diminish in the region between $x = -20$ mm and $x = 0$ mm over a wide range of operating conditions. Note also that the broadband fluctuations are concentrated at $x = -10$ mm and beyond the exit plane at low voltages, but are damped in this spatial region at high voltages. This dramatic difference suggests that the nature of these high frequency disturbances differ depending on the operating voltage.

A comparison of the response of two probes located at the same axial position, but separated by some angle on the azimuth, provides additional information on the nature of these disturbances. A cross-spectral analysis of the signals from the two probes provides a measure of their coherence, suggests the direction of propagation, and can be used to estimate the azimuthal phase velocity. The azimuthal phase velocity V_{py} of the disturbances can be obtained from:

$$V_{p_y}(f) = 2\pi f \left(\frac{\theta_p R}{\phi_2(f) - \phi_1(f)} \right) \quad (2)$$

where θ_p is the angular probe separation (in radians), R is the channel radius, $f = \omega/2\pi$ is the frequency, and $\phi_{1,2}$ are the phase shifts of the individual probe signals, determined from:

$$\phi_{1,2}(f) = \tan^{-1} \left(\frac{\text{Im}_{1,2}(f)}{\text{Re}_{1,2}(f)} \right) \quad (3)$$

with Re and Im the real and imaginary components of the complex Fourier transform $F(f) = \text{Re}(f) + i\text{Im}(f)$, respectively.

The signals from the two probes were used to derive wave dispersion maps, rendered as the phase velocity verses wave frequency. In all cases, conditional sampling is employed, to isolate only the strongest correlated disturbances detected by the two probes. Two examples of dispersion maps are shown in Fig. 9, for a relatively low operating voltage (100V) and an axial position of $x = 0$, and for a relatively high voltage (172V) and a location just 12 mm beyond the exit plane. For these dispersion studies, the azimuthal probe separation was $\theta_p = 30^\circ$. Disturbances were considered only if the amplitude of the component on the first probe was at least three times its mean, and that on the second probe, within its mean and five times its mean. The condition imposed on the second probe allows for the possible damping of the wave or loss of intensity due to out-of-plane propagation.

Also drawn in the dispersion maps of Fig. 9 are lines corresponding to the azimuthal component phase velocities for the $m=1$, $m=4$, and $m=12$ azimuthal modes of the cylindrical annulus. In general, we can express the azimuthal phase velocity for a tilted azimuthal mode:

$$V_{p_y} = \frac{2\pi \cos(\alpha)}{\sqrt{k_x^2 + k_y^2}} \cdot f = \frac{2\pi \cos(\alpha)}{\sqrt{k_x^2 + \left(\frac{m}{r}\right)^2}} \cdot f \quad (4)$$

Here, k_x and k_y are the component wavenumbers along the axial and azimuthal directions, respectively. We assume that $k_y = m/r$, and m is the integer azimuthal mode number. For a purely azimuthal wave, the axial wave number component is $k_x = 0$. For $m=1$ and $k_x=0$ condition, the oscillation wavelength is equal to the channel circumference, $2\pi r$ where as it is one-fourth and one-twelfth the circumference for the pure azimuthal $m=4$ and $m=12$ modes, respectively. In the top

frame of Fig. 9, we also depict vertical lines corresponding to possible $m = 0$ modes. For $m = 0$, the wave is longitudinal and the azimuthal phase velocity is infinite. In general, the observed natural disturbances can have both azimuthal and axial components, and can propagate with an angle α , defined by:

$$\tan \alpha = \frac{k_x}{k_y} \quad (5)$$

An examination of the dispersion maps, and comparison to the lines associated with the pure azimuthal $m = 1$ mode suggests that some of these disturbances may be tilted out of the azimuthal plane (ie $k_x \neq 0$). Indeed, for the $m = 1$ modes shown in the top and bottom frames of Fig. 9, a propagation angle of 15° and 20° respectively has been used to best capture the trends seen for these disturbances. The strong $m = 1$ low-frequency disturbances at $x = 0$ also appear, however, to have a range in the possible propagation directions, preferring lower propagation angles at the lower frequencies.

IV. RESULTS DISCUSSION

A number of features are identifiable in the dispersion maps of Fig. 9, attributed here to four or possibly five intrinsic instabilities, and an instability induced by the probes themselves. We shall discuss them here, some within the context of what has been seen experimentally in previous Hall discharge studies.

The most prominent mode seen at low voltages is that of a relatively strong, $m = 1$ azimuthally propagating disturbance of frequency in the 5-10 kHz range, and of phase velocity $V_{py} \sim 1000 - 4000$ m/s, nearly equal to the critical ionization velocity of the xenon propellant. As mentioned above, that the data in this region departs slightly from the superimposed line $m = 1$ ($\alpha = 15^\circ$) line suggests that this disturbance lacks a unique tilt in its propagation vector, and that the propagation angle tends to increase slightly with increasing frequency. These waves are similar in their properties to those identified by Janes and Lowder [3], and others [4,7], as "rotating spokes", and are attributed to tilted ionization waves of still unknown origin, although the connection to the critical ionization velocity may be more than coincidental since an appropriate scaling is found when operating on different inert gases [3]. A second prominent mode seen at low discharge voltage is that associated with nearly purely $m = 0$ axial modes at higher frequencies, a few of which are identified on the figure by superimposing vertical lines at characteristic frequencies. These modes will be more apparent on

dispersion plots discussed later. While the behavior of these modes are consistent with an $m = 0$ azimuthal mode, they could be higher-order azimuthal modes that are propagating in the axial direction (the azimuthally spaced probes would not resolve this). These high frequency modes correspond to the nearly constant frequency bursts seen as intense horizontal striations in the low voltage (86V and 100V) spectral maps in Fig. 7. It is noteworthy that these disturbances are relatively turbulent and broadband, and they exhibit a curious power-law behavior in their spectral distribution. Fig. 10 displays the Fourier transform of the plasma density fluctuations for the 100V and also 86V cases, showing a characteristic $-5/3$ power law power-law decay in the amplitudes at frequencies beyond 20 kHz (indicated by the dashed line in the figures). It is natural at first to suspect that these turbulent, longitudinal disturbances may correspond to the so-called “transit time” oscillations first identified by Morizov and colleagues [4,7], and conjectured to be associated with transit time of ions within the acceleration channel. We dismiss this possibility here, because we see that they are excited at relatively low discharge voltage (in the ionization branch of the I-V characteristic), unlike the broadband oscillations described in Ref. 4 and 7. Furthermore, the frequencies are much lower than the inverse transit time of the ions in the acceleration region of the thruster, which, for our case, is approximately 500 kHz.

A third mode seen in the low discharge voltage dispersion plot in Fig. 9 appears actually as a low-velocity cut-off to the higher frequency longitudinal modes, and is identified on the frame with a line corresponding to an $m = 4$ mode. The origin of this clear demarcation is not presently understood, although we suspect that it is associated with an azimuthal asymmetry due to the four equally spaced magnetic solenoids that connect to the front outer pole-piece. The persistence of this demarcation is seen to weaken with increasing voltage, and is non-existent at the higher discharge voltages studied. This result is consistent with an examination of the axial and azimuthal variation in the mean signal from a single probe, which reflects the spatial variation in mean plasma density, as seen in Fig. 11 for a representative low voltage (86V) and high voltage (150V) condition. It is seen that the four-fold asymmetry associated with the solenoid placement is more apparent in the azimuthal variation in the plasma density at lower voltages. The interaction between the axial disturbances and the $m = 4$ azimuthal asymmetry is the subject of ongoing research in our laboratory.

A fourth mode which appears at high operating voltages is that of an azimuthal $m = 1$ wave, tilted to approximately 20° , and in the frequency range above 20 kHz (see Fig. 9 panel for 172V

condition). High frequency azimuthal disturbances (extending as far as ~ 1 MHz) have been identified in the past [8] and have been attributed to drift instabilities of “magnetosonic” waves, excited primarily in the axial region where the magnetic field gradients have negative values (i.e., B decreases with increasing distance from the anode). Simple theories have been suggested for the growth rate and the dispersion of these waves [8] based on a multi-fluid description of the magnetohydrodynamic flow, although a rigorous comparison to experimental measurements has not yet been carried out. While it is tempting to suggest that the disturbances at low frequencies seen here may be the band edge of such drift-instabilities, our results do not support such an assignment, since these azimuthal waves, responsible for the high frequency disturbances shown in Fig. 7 (for the high voltage conditions) are not largely excited in the region of negative magnetic field gradients. In fact, there is a sudden damping of the waves at approximately $x = -5$ mm, beyond which there is very little high frequency activity. This location, which defines the edge of the activity of these disturbances, is about the location of the peak in the magnetic field (see Fig. 2). It is also tempting to suggest that the azimuthal disturbances seen at higher discharge voltages may simply be an extension of the low frequency azimuthal waves seen at lower voltage. However, the azimuthal waves seen at the lower voltages are predominantly excited in regions where the magnetic field gradients are negative, consistent with what has been seen in the literature [4].

A fifth mode that is apparent at high voltage conditions is that of an exceptionally strong low-frequency (~ 5 -10 kHz) axial ($m = 0$) disturbance that is present within the ionization zone. This disturbance, which is associated with very strong overall discharge current fluctuations, is known to interact with the external circuitry driving the discharge [20]. In the literature, this instability has been referred to as the characteristic “breathing” mode [20], the “circuit” instability [2], or the “loop” instability [9]. The origin of this instability is now reasonably well understood and its behavior has been captured in many discharge simulations [21-23]. The instability is characteristic of a predator-prey behavior in the neutral xenon and xenon ion dynamics, coupled by the ionization process [22]. It is manifested as a disturbance in the balance between the rapid removal of xenon ions within the discharge channel via electrostatic acceleration, and the replenishment of the channel with ions created from the slow-moving neutrals. The characteristic frequency of this instability is expected to be close to the inverse of the residence time of the neutrals within the ionization zone, and has been found to scale appropriately with diminishing discharge scale lengths [24].

A sixth mode that is identifiable in both frames of Fig. 9 is that of an $m = 12$ azimuthal wave, which has a wavelength equal to that of the separation between the two probes, and is believed to be “anchored” by the placement of the probes within the discharge annulus. The mode number of these disturbances is found to track the relative placement of the two probes used to study the intrinsic plasma fluctuations, as shown in Fig. 12, for exit plane disturbances ($x = 0$ mm), and a moderate operating voltage (125V). An intriguing feature of the plots in Fig. 11 is that the placement of the probes also impacts the behavior of the other prominent $m = 1$ mode. It is noteworthy that as the mode number corresponding to the separation of the probes diminishes, there seems to be an increased “coupling” of the disturbances, as seen by the tendency of the points on the $m = 1$ line to “gravitate” towards the line corresponding to the dispersion of the induced modes. The discovery of this induced perturbation and the coupling of these disturbances to the $m = 1$ mode may have applications in the control of thruster oscillations, and, quite possibly, the control of electron transport if strongly correlated azimuthal waves are largely responsible for the anomalous axial electron flow.

Fig. 13 gives the dispersion plots obtained for some of the operating conditions of the spectral maps shown in Fig. 7. A comparison is made between the plots obtained at three axial locations. At an axial location corresponding to the exit plane of the discharge ($x = 0$), we see that high discharge voltage operation is dominated by relatively strong high frequency $m = 1$ azimuthal waves (tilted slightly with respect to the azimuthal plane), and low frequency longitudinal waves, most likely associated with the “breathing” mode ionization instability. At lower voltages, the high frequency azimuthal waves become apparently more longitudinal in direction, and there is a growth of very strong low-frequency azimuthal waves, associated with the ionization process. For the low voltage case shown, the azimuthal asymmetry associated with the placement and separation of the magnetic solenoids plays a significant role in the wave dynamics only beyond $x = 0$ mm, and appears to have a dominating effect on the propagation of the disturbances in this region. A comparison of the dispersion plots at the three locations for the highest operating voltage shown confirms the conclusions that were drawn earlier that the growth and propagation of these higher frequency azimuthal waves do not depend on the sign of the local gradient in the magnetic field in contradiction to what has been postulated in the literature for azimuthal waves of higher frequency [4,7]. On the other hand, a comparison of the dispersion plots for these three axial locations for the lowest

operating voltage shown suggests that the low-frequency azimuthal waves indeed are seen to be active most notably in the region where the magnetic field gradients are negative.

V. SUMMARY

A detailed examination of the propagation behavior of low (2-20 kHz) and intermediate-frequency (20-100 kHz) oscillations in closed-electron drift Hall a discharge is presented. Conditional sampling using two electrostatic probes collecting ion saturation current is used to identify and extract properties of correlated structures associated with the propagation of azimuthal and longitudinal instabilities within the discharge channel. The azimuthal component phase velocities (dispersion plots) are determined for a range of wave frequencies and over characteristic regimes of operation of the discharge. A variety of propagation modes are observed and analyzed, some of which have been documented in the previous literature. In addition to the low-frequency azimuthal "spokes" and the so-called "breathing mode" that is well known to be excited in these discharges, we have identified the appearance longitudinal disturbances (that are prevalent at low discharge voltages) and azimuthal disturbances (at higher discharge voltages) in the 20 – 100 kHz range that do not seem to have been described previously. Finally, we have seen that the presence of azimuthal non-uniformities due to the location of the magnetic solenoids, and, due to the placement of the diagnostic probes, can couple strongly to the intrinsic natural instabilities. Such methods of coupling to the natural dynamical behavior of these discharges may be useful in the control or enhancement of turbulence, which is known to influence the axial electron transport.

Acknowledgements

This research was funded by the Air force Office of Scientific Research. N.B. Meezan was supported through a National Defense Science and Engineering Graduate Fellowship. Additional support for E. Chesta was provided by the Politecnico di Torino, Italy, and by the Ecole Centrale Paris, France, through the Top Industrial Managers for Europe program.

References

- [1] G.A. Popov and Y.A. Ryzhov, "Electric propulsion in Russia and its practical applications", *Z. Fluwiss. Weltraumforsch* **17**, 161-169, 1993.
- [2] E.Y. Choueiri, "Characterization of oscillations in closed drift thrusters", AIAA Paper No. 94-3013, 30th Joint Propulsion Conference, Indianapolis, IN, June 27-29, 1994.

- [3] G.S. Janes and R.S. Lowder, "Anomalous electron diffusion and ion acceleration in a low-density plasma", *Phys. Fluids* **9**, 1115-1123, 1966.
- [4] A.I. Morozov, Y.V. Esipchuk, A.M. Kapulkin, V.A. Nevrovskii, and V.A. Smirnov, "Effect of the magnetic field on a closed-electron-drift accelerator", *Sov. Phys. – Tech. Phys.* **17**, pp. 482-487, 1972.
- [5] A.I. Morozov, V.A. Nevrovskii, and V.A. Smirnov, "Effect of feedback system on the plasma flux in an accelerator with closed electron drift", *Sov. Phys. – Tech. Phys.* **18**, pp. 344-347, 1973.
- [6] A.I. Morozov, V.A. Nevrovskii, and V.A. Smirnov, "Driven electrostatic plasma oscillations in a closed electron drift accelerator", *Sov. Phys. – Tech. Phys.* **18**, pp. 339-343, 1973.
- [7] Y.V. Esipchuk, A.I. Morozov, G.N. Tilinin, A.V. Trofimov, "Plasma oscillations in closed-drift accelerators with an extended acceleration zone", *Sov. Phys. – Tech. Phys.* **43**, pp. 1466-1473, 1973.
- [8] Y.V. Esipchuk and G.N. Tilinin, "Drift instability in a Hall-current plasma accelerator", *Sov. Phys. – Tech. Phys.* **21**, pp. 417-423, 1976.
- [9] G.N. Tilinin, "High-frequency plasma waves in a Hall accelerator with an extended acceleration zone", *Sov. Phys. – Tech. Phys.* **22**, pp. 974-978, 1977.
- [10] V.I. Baranov, Y.S. Nazarenko, V.A. Petrosov, A.I. Vasin, and Y.M. Yashnov, "Electron drift oscillations outside the accelerator with closed electron drift," IEPC Paper No. 95-062, 24th International Electric Propulsion Conference, Moscow, Russia, 1995.
- [11] V.I. Baranov, Y.S. Nazarenko, V.A. Petrosov, A.I. Vasin, and Y.M. Yashnov, "Electron drift oscillations outside the accelerator with closed electron drift," AIAA Paper No. 96-3192, 32nd Joint Propulsion Conference, Lake Buena Vista, FL, July 1-3, 1996.
- [12] D. Kusamoto and K. Komurasaki, "Optical diagnostics of the plasma in the channel of a Hall thruster" IEPC Paper No. 97-067, 25th International Electric Propulsion Conference, Cleveland, OH, 1997.
- [13] F. Darnon, M. Lyszyk, and A. Bouchoule, "Optical investigations on plasma oscillations of SPT thrusters," AIAA Paper No. 97-3051, 33rd Joint Propulsion Conference, Seattle, WA, July 6-9, 1997.

- [14] M.A. Cappelli, W.A. Hargus, Jr., and N.B. Meezan, "Coherent structures in crossed-field closed-drift Hall thrusters," IEEE Trans. Plasma Sciences **27**, pp. 96-97, 1999.
- [15] N. Gascon, C. Perot, G. Bonhomme, X. Caron, S. Bechu, P. Lasgorceix, B. Izrar, M. Dudeck, "Signal processing and non-linear behavior of a stationary plasma thruster: first results", AIAA Paper No. 99-2427, 35th Joint Propulsion Conference, Los Angeles, CA, June 20-24, 1999.
- [16] N.B. Meezan and M.A. Cappelli, "The anomalous electron mobility in a coaxial Hall discharge plasma" *submitted to Physical Review E*, June, 2000.
- [17] W.A. Hargus, Jr., and M.A. Cappelli, "Laser induced fluorescence measurements on a laboratory Hall thruster," AIAA Paper No. 98-3645, 34th Joint Propulsion Conference, Cleveland, OH, July 13-15, 1998.
- [18] W.A. Hargus, Jr., "Investigation of the plasma acceleration mechanism within a co-axial Hall thruster." Ph.D. Thesis, Mechanical Engineering Department, Stanford University.
- [19] M.Lieberman and A. Lichtenberg, Principles of Plasma Discharges and Material Processing, p. 161, Wiley and Sons, NY, 1994.
- [20] V. Zhurin, J. Kahn, H. Kaufman, K. Kozubsky, and M. Day, "Dynamic characteristics of closed drift thrusters, IEPC Paper No. 93-095, 23rd International Electric Propulsion Conference, Seattle, WA, 1993.
- [21] J. P. Boeuf and L. Garrigues, "Low frequency oscillations in a stationary plasma thruster." J. Appl. Phys. **84**, pp. 3541-3554, 1998.
- [22] J. Fife and M. Martinez-Sanchez, and J. Szabo, "A numerical study of low frequency discharge oscillations in Hall thrusters," AIAA Paper No. 97-3052, 33rd Joint Propulsion Conference, Seattle, WA, July 6-9, 1997.
- [23] E. Fernandez, M.A. Cappelli, and K. Mahesh, "2D simulations of Hall thrusters", Annual Research Briefs of the Center for Turbulence Research, Stanford University, pp. 81 – 90, 1998.
- [24] D.P. Schmidt, N.B. Meezan, W.A. Hargus, Jr., and M.A. Cappelli, "A low-power, linear-geometry Hall plasma source with an open electron-drift", Plasma Sources Sci. Technol. **9** pp. 68-76, 2000.

Figure Captions

FIG. 1. Schematic of a typical Hall discharge.

FIG. 2. Axial profile of radial magnetic field strength for the Hall discharge studied.

FIG. 3. Schematic of the Langmuir probes used to detect plasma density fluctuations.

FIG. 4. Schematic of the experimental arrangement showing the location and orientation of the Langmuir probes.

FIG. 5. Typical current – voltage Hall discharge characteristics.

FIG. 6. Spectral maps of the amplitude of the fluctuations in the probe signals over discharge voltage for axial locations of 12.7 mm, 0, -12.7 mm, and -25.4 mm (top to bottom).

FIG. 7. Spectral maps of the amplitude fluctuations in probe signal (left) and ratio of the amplitude fluctuations to the mean signal (right) for discharge conditions of 86V, 100V, 128V, 161V and 184V (top to bottom).

FIG. 8. Axial variation in the mean electron density [16].

FIG. 9. Typical experimental dispersion plots derived from the azimuthal probes located at the discharge exit ($x = 0$ mm) but separated by 30° . The top frame is for a discharge voltage of 100V, and the bottom frame is for a discharge voltage of 172V.

FIG. 10. Fourier spectrum of the fluctuations in plasma density at the exit of the Hall discharge. The top frame is for a discharge voltage of 86V, and the bottom frame is for a discharge voltage of 100V.

FIG. 11. Axial and azimuthal variation in the mean plasma density for 86V and 150V operating conditions. The gray scale is such that white corresponds to peak plasma densities of approximately $3 \times 10^{17} \text{ m}^{-3}$.

FIG. 12. Dispersion plots obtained using (top to bottom) probe separations of 180, 120, 90, and 60, degrees.

FIG. 13. Dispersion maps for the discharge conditions of Fig. 6, for just two voltage conditions (128V – top panels, and 186V – bottom panels) with the probes located at $x = -12.7$ mm (left panels), $x = 0$ mm (center panels), and $x = 12.7$ mm (right panels). The dashed line (---) corresponds to the pure $m = 12$ azimuthal mode, the dotted line (...) to the $m = 1$ azimuthal mode, the dot-dash line (vertical line) to the $m = 0$ mode, and the solid line to the $m = 4$ azimuthal mode.

Figure Captions

FIG. 1. Schematic of a typical Hall discharge.

FIG. 2. Axial profile of radial magnetic field strength for the Hall discharge studied.

FIG. 3. Schematic of the Langmuir probes used to detect plasma density fluctuations.

FIG. 4. Schematic of the experimental arrangement showing the location and orientation of the Langmuir probes.

FIG. 5. Typical current – voltage Hall discharge characteristics.

FIG. 6. Frequency maps of fluctuations in the probe signals over discharge voltage for axial locations of 12.7 mm, 0, -12.7 mm, and -25.4 mm (top to bottom).

FIG. 7. Spectral maps of the amplitude fluctuations in probe signal (left) and ratio of the amplitude fluctuations to the mean signal (right) for discharge conditions of 86V, 100V, 128V, 161V and 184V (top to bottom).

FIG. 8. Axial variation in the mean electron density [16].

FIG. 9. Typical experimental dispersion plots derived from the azimuthal probes located at the discharge exit ($x = 0$ mm) but separated by 30° . The top frame is for a discharge voltage of 100V, and the bottom frame is for a discharge voltage of 172V.

FIG. 10. Fourier spectrum of the fluctuations in plasma density at the exit of the Hall discharge. The top frame is for a discharge voltage of 86V, and the bottom frame is for a discharge voltage of 100V.

FIG. 11. Axial and azimuthal variation in the mean plasma density for 86V and 150V operating conditions. The gray scale is such that white corresponds to peak plasma densities of approximately $3 \times 10^{17} \text{ m}^{-3}$.

FIG. 12. Dispersion plots obtained using (top to bottom) probe separations of 180, 120, 90, and 60, degrees.

FIG. 13. Dispersion maps for the discharge conditions of Fig. 6, for just two voltage conditions (128V – top panels, and 186V – bottom panels) with the probes located at $x = -12.7$ mm (left panels), $x = 0$ mm (center panels), and $x = 12.7$ mm (right panels). The dashed line (---) corresponds to the pure $m = 12$ azimuthal mode, the dotted line (...) to the $m = 1$ azimuthal mode, the dot-dash line (vertical line) to the $m = 0$ mode, and the solid line to the $m = 4$ azimuthal mode.

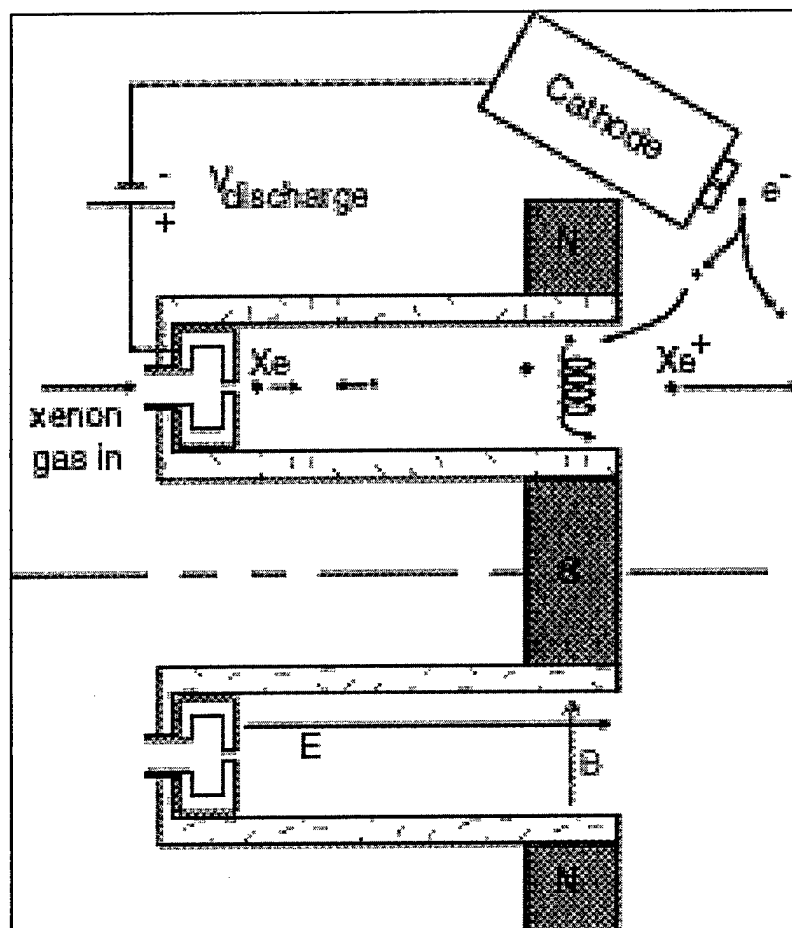


Figure 1, Chesta et al.

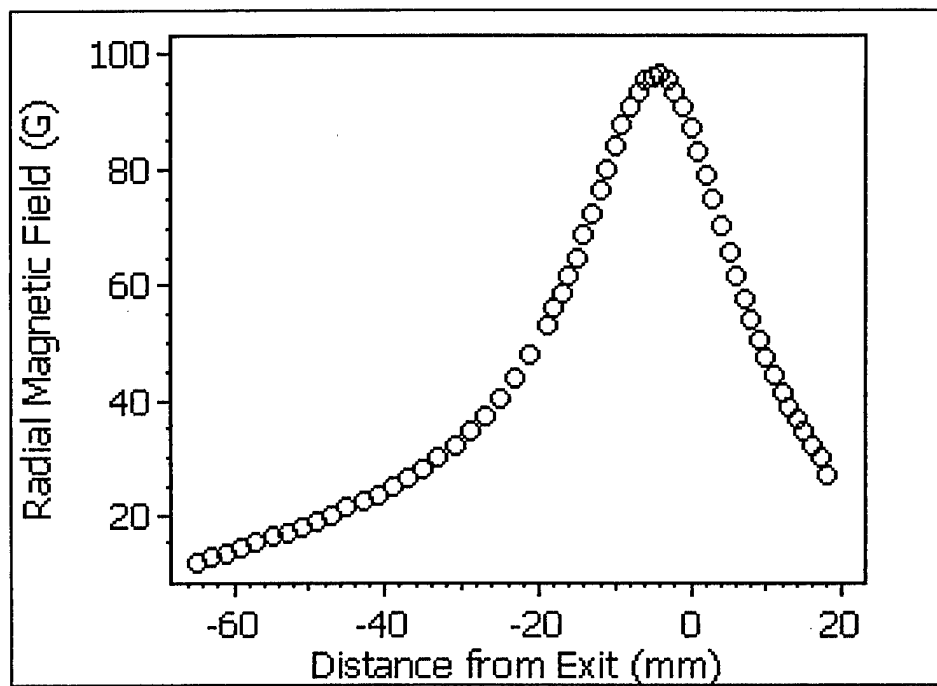


Figure 2, Chesta et al.

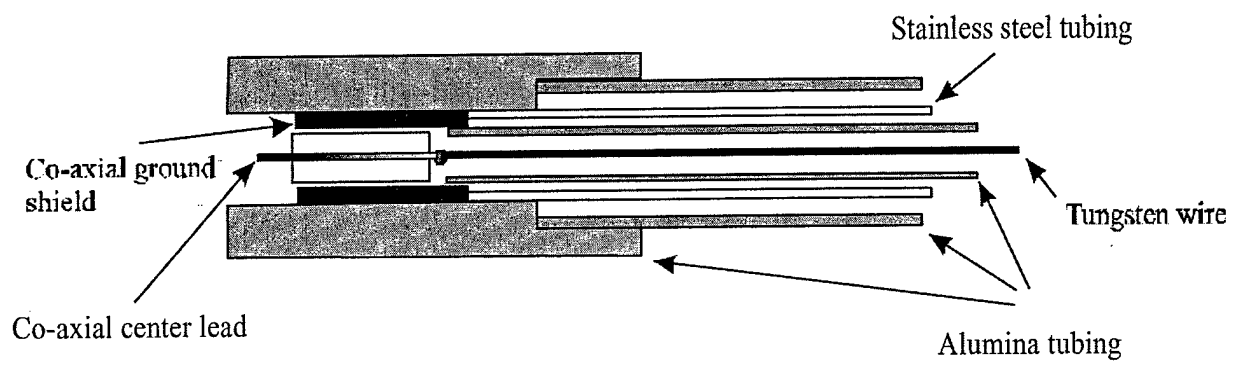


Figure 3, Chesta et al.

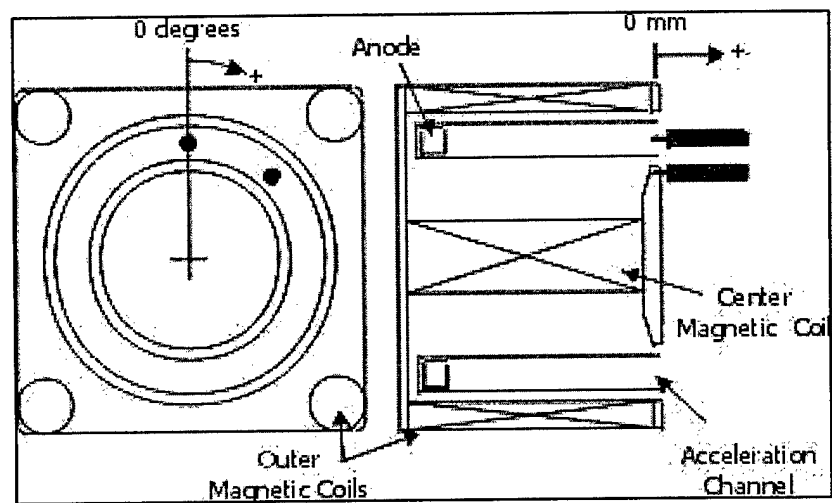


Figure 4, Chesta et al.

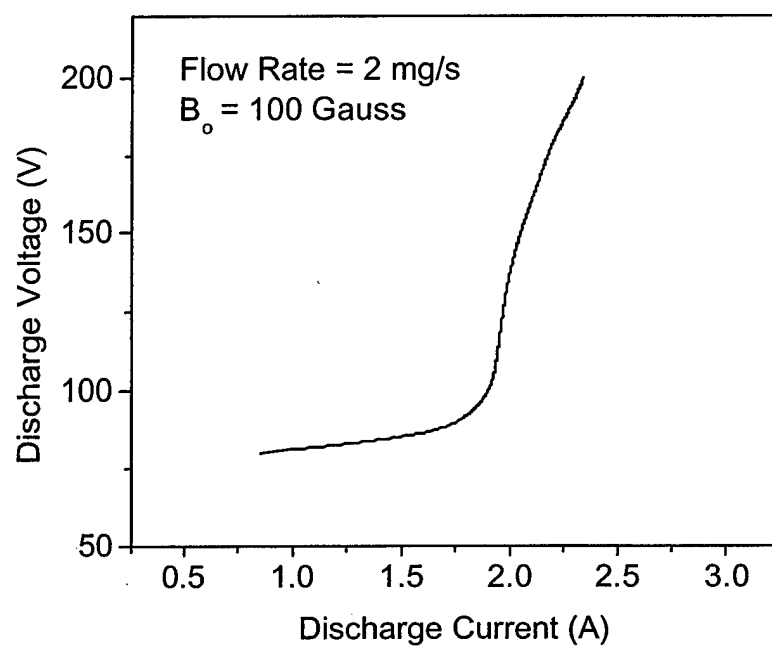


Figure 5, Chesta et al.

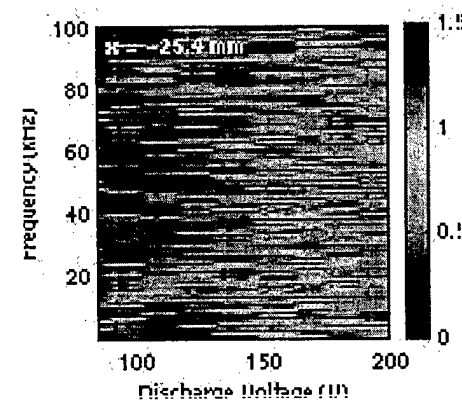
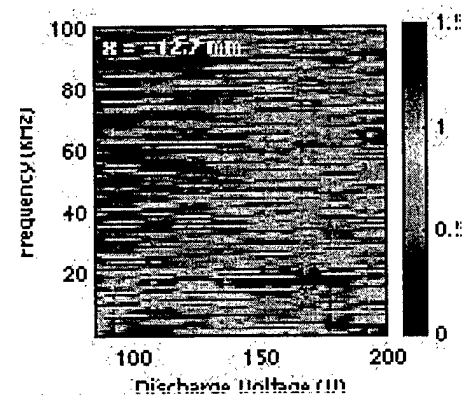
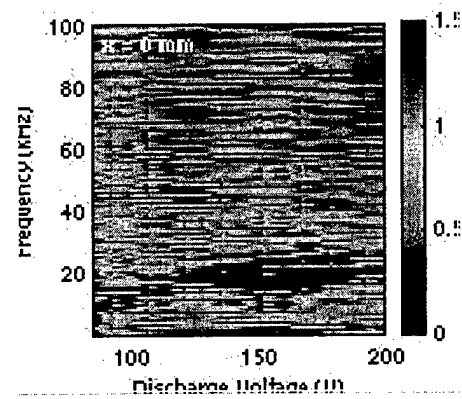
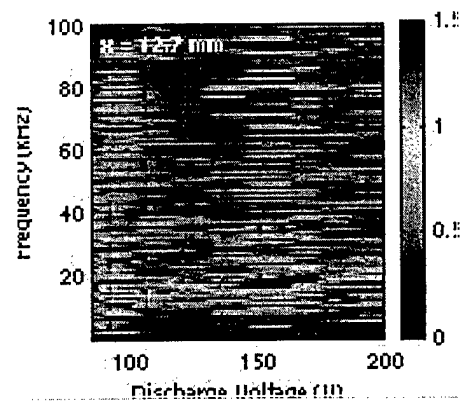


Figure 6, Chesta et al.

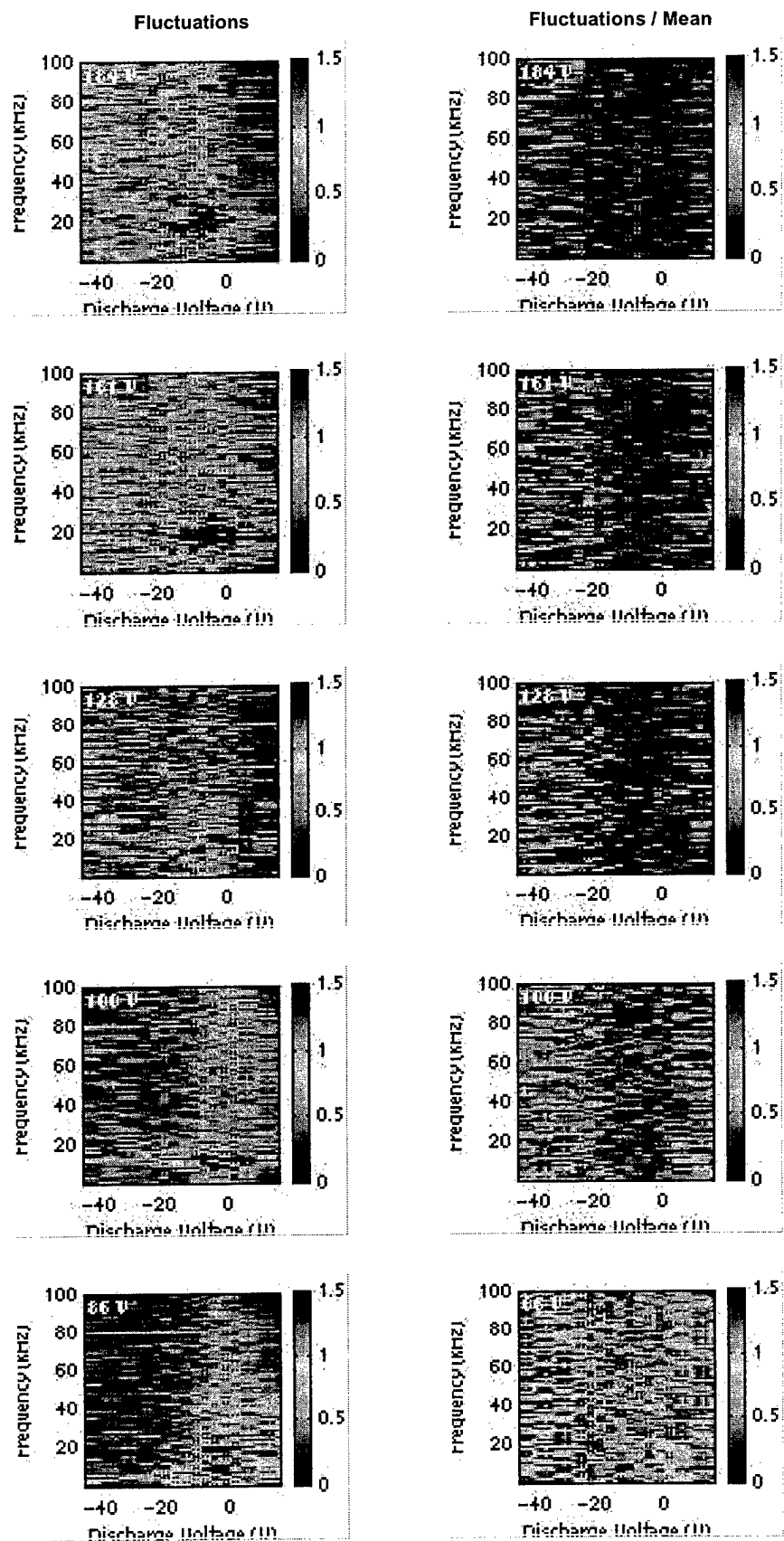


Figure 7, Chesta et al.

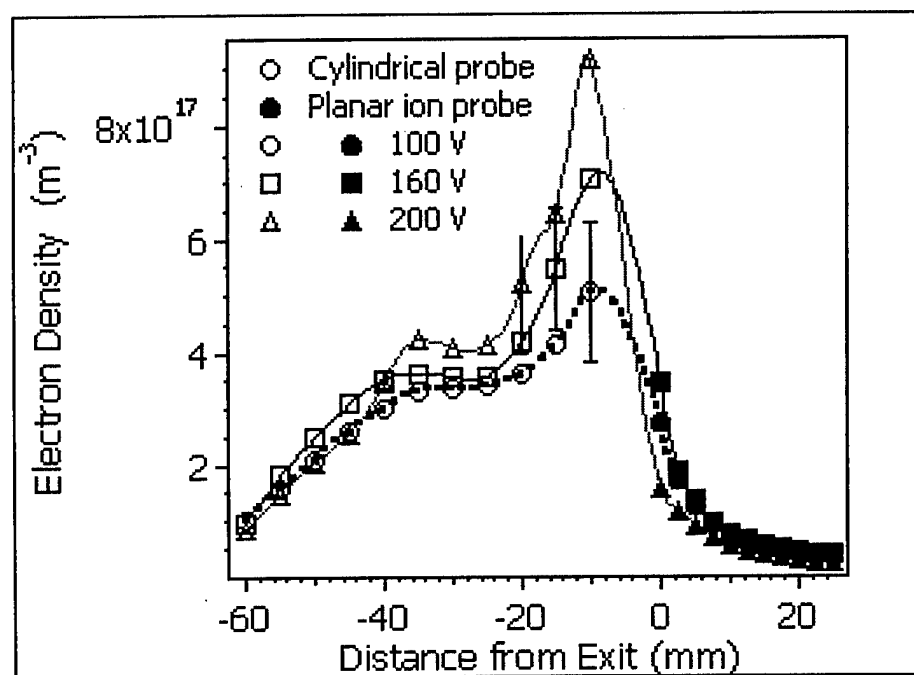


Figure 8. Chesta et al.

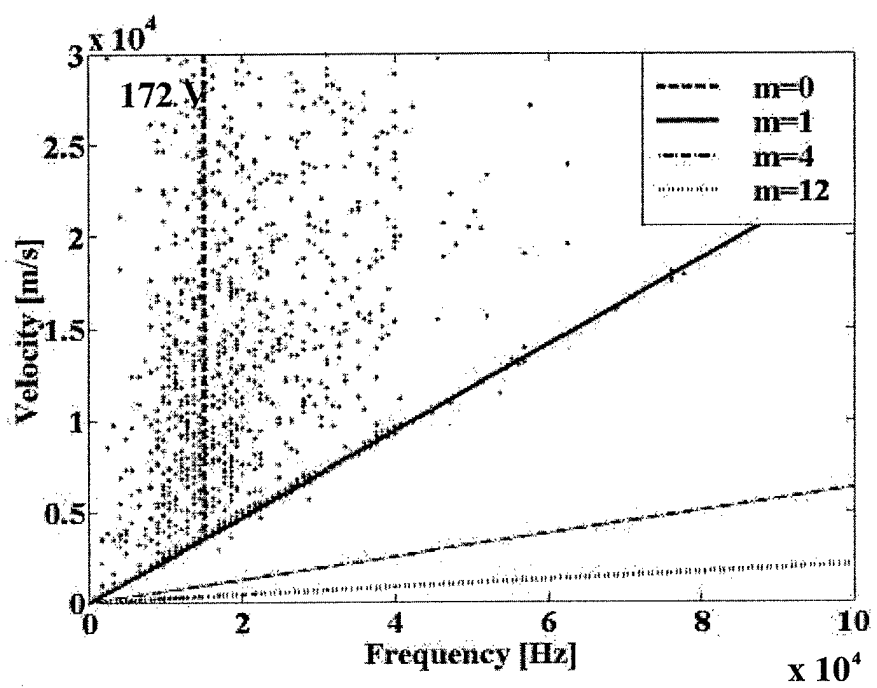
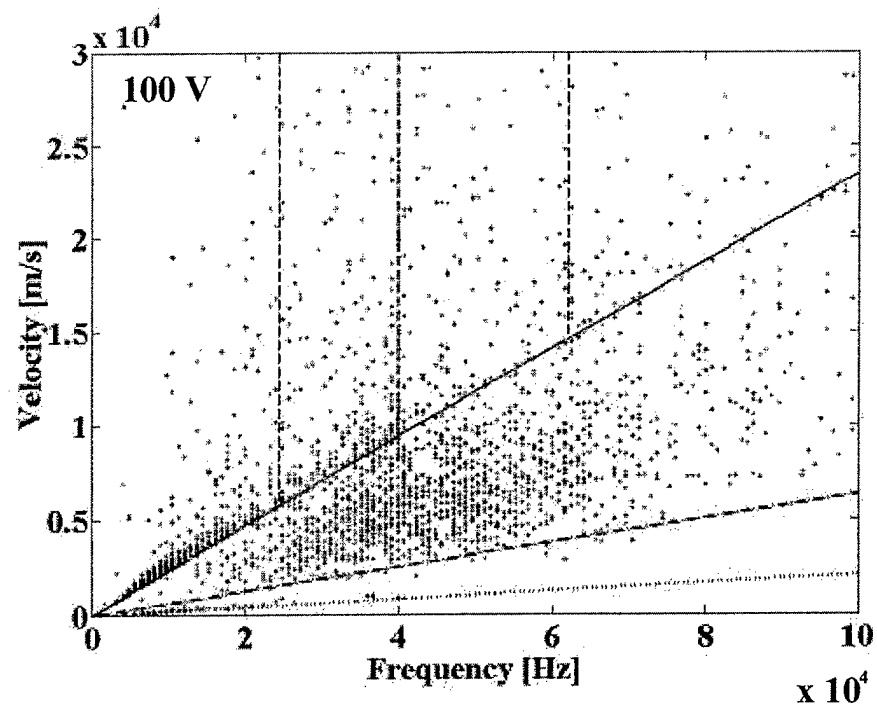


Figure 9. Chesta et al.

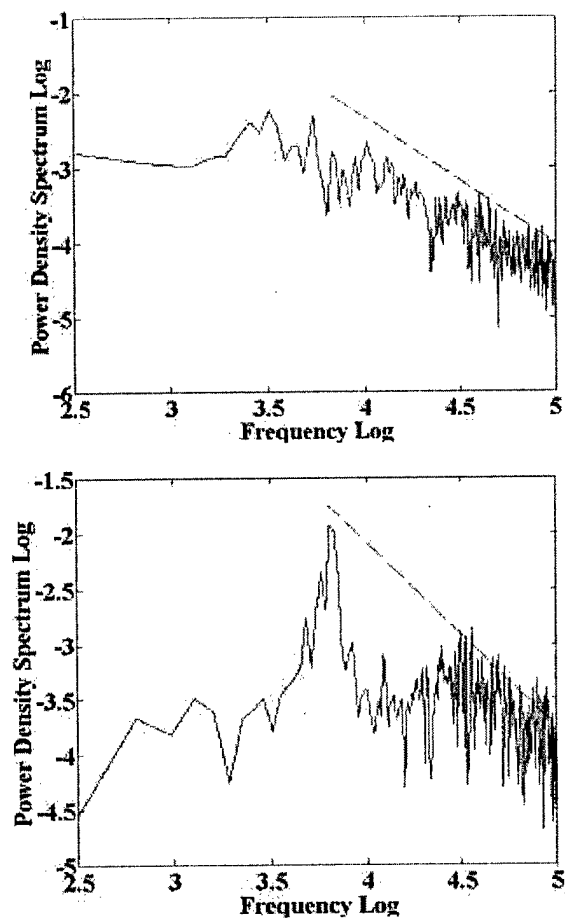


Figure 10. Chesta et al.

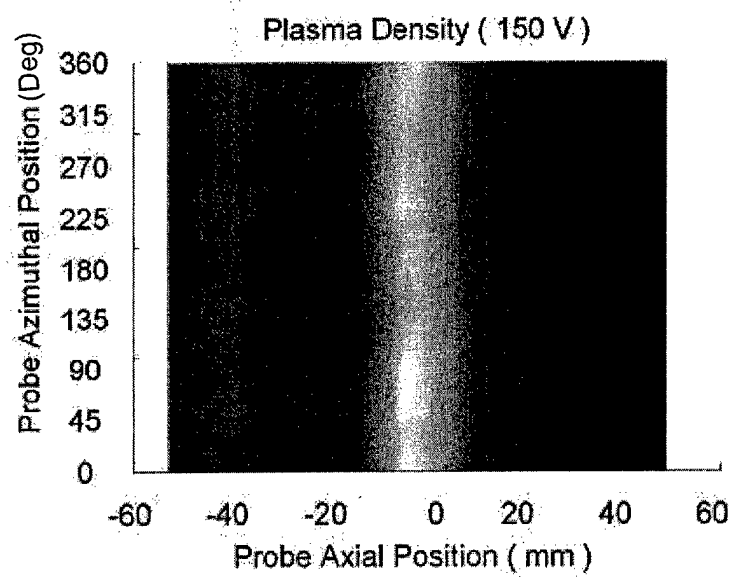
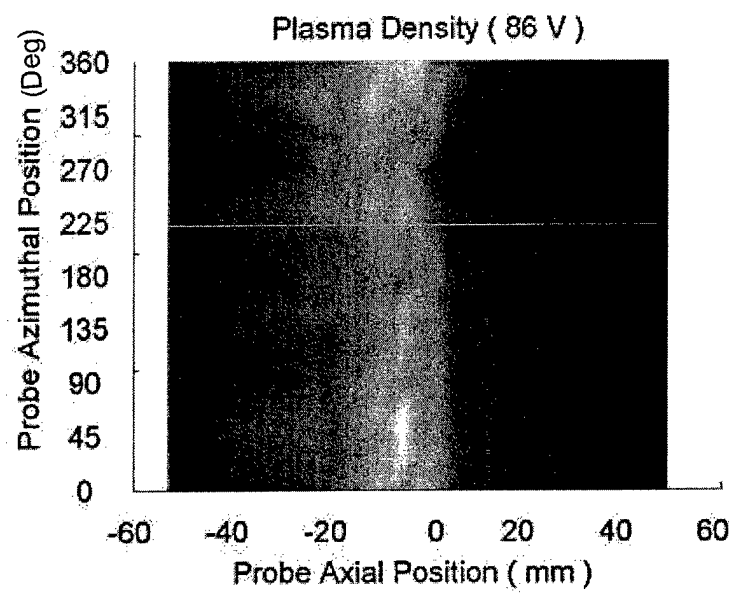


Figure 11. Chesta et al.

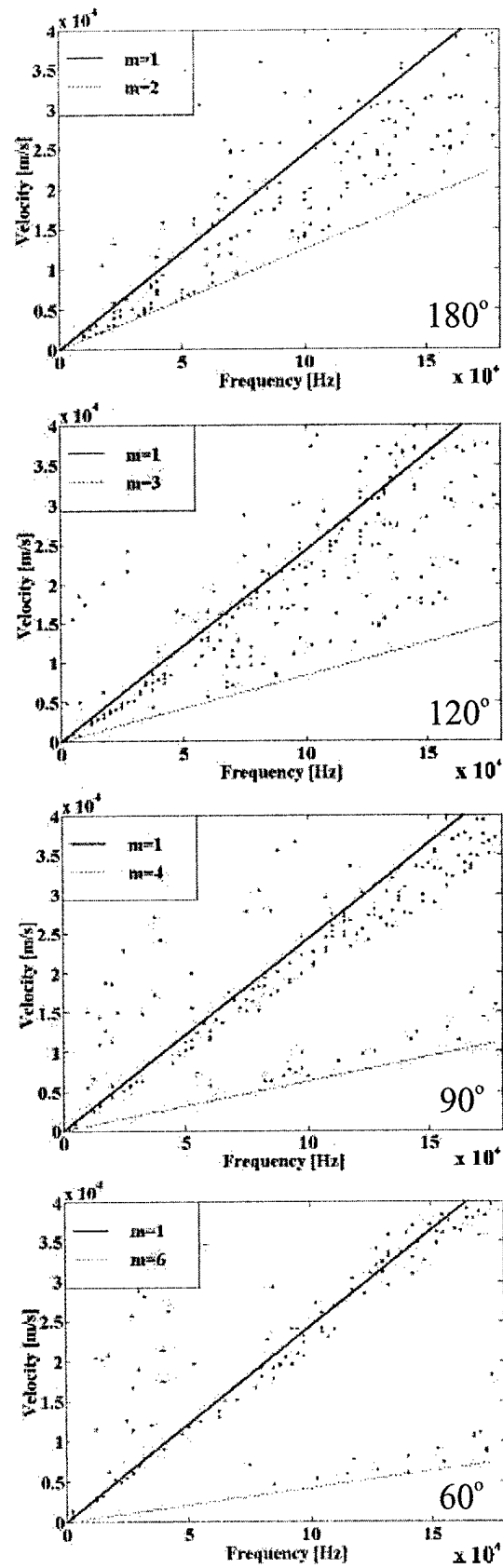


Figure 12. Chesta et al.

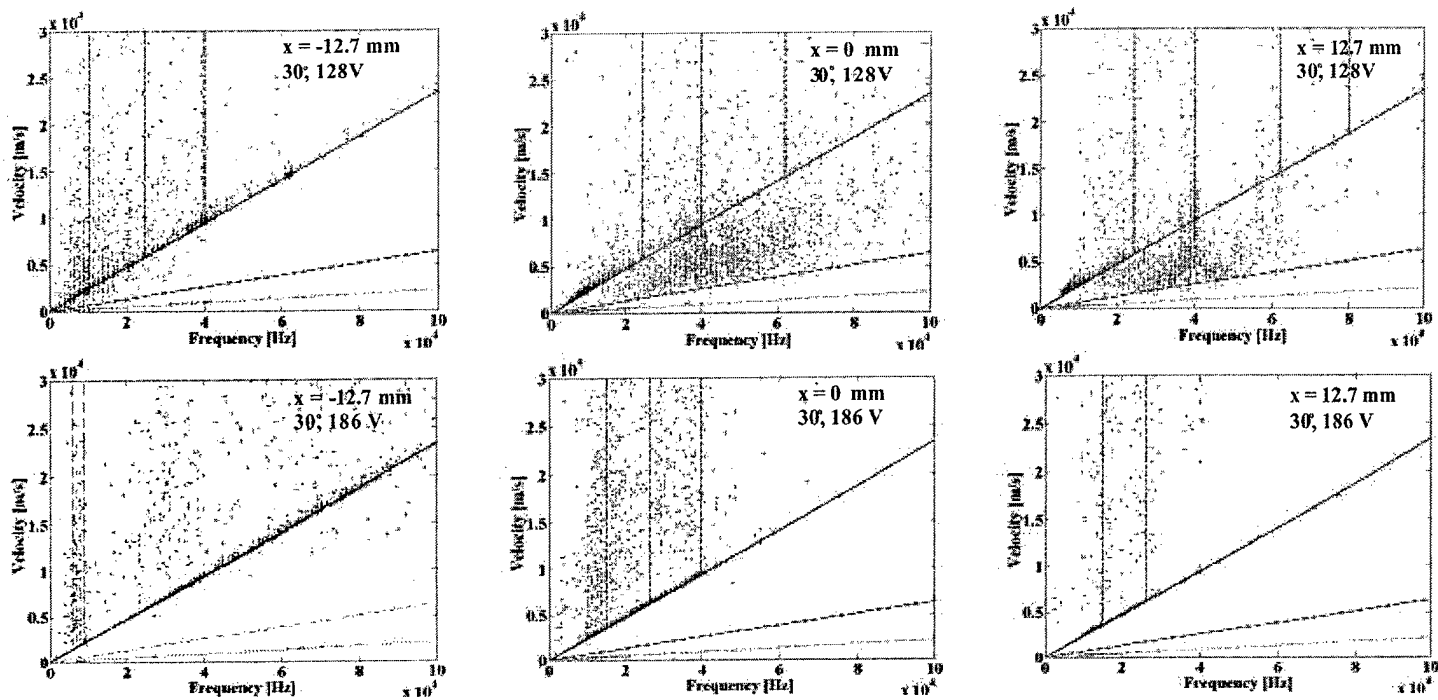


Figure 13. Chesta et al.

Appendix IV

The Stability of a Magnetized Hall Plasma Discharge

E. Chesta, N.B. Meezan, and M.A. Cappelli,

To appear in accepted to *Journal of Applied Physics*, 2001

Stability of magnetized Hall plasma discharge

E. Chesta, N. B. Meezan, and M. A. Cappelli^{a)}

Department of Mechanical Engineering, Thermosciences Division, Stanford University, Stanford, California 94305-3032

(Received 29 August 2000; accepted for publication 9 December 2000)

Using recent experimental data on the time-averaged, spatially varying plasma properties within a Hall discharge plasma, we present in this article, a theoretical study of the response of this plasma to small (linear) perturbations in its properties. As a starting point for this analysis, we assume a two-dimensional fluid description that includes a simplified equation for the electron energy, and constrain the azimuthal wave vector such that we excite only the dominant ($m=1$) azimuthal modes. The growth rate and frequencies of predominantly axial and azimuthally propagating plasma disturbances are obtained by numerical solution of the resulting eigenvalue problem under a quasiuniform plasma condition, along the entire discharge channel. The results identify the persistence of a low frequency instability that is associated with the ionization process, concentrated largely in the vicinity of the exit plane, where the magnetic field is at its maximum value, consistent with experimental observations for the relatively low operating voltages (~ 100 V) considered in this study. © 2001 American Institute of Physics. [DOI: 10.1063/1.1346656]

I. INTRODUCTION

Closed electron drift thrusters (CEDTs) are crossed-field co-axial Hall discharge plasma sources presently considered for use as satellite propulsion devices. Their potential as high specific impulse thrusters for space propulsion date back to the early 1960s.^{1,2} In a traditional CEDT, the plasma is sustained in an orthogonal electric and magnetic field. Electrons emitted by an external cathode are magnetized by the magnetic field and drift in the $\mathbf{E} \times \mathbf{B}$ direction. Ions, generated through volume ionization, having a Hall parameter much less than unity, are not magnetized, but are accelerated by the electrostatic fields established by the retarded electron flow. In a co-axial geometry, the electrons are constrained to move in the azimuthal direction of the closed $\mathbf{E} \times \mathbf{B}$ drift (hence the name "closed electron drift thruster"). The cross-field drift of electrons toward the anode is known to be anomalously high (greater than that determined by the plasma collisionality) and the mechanism for this anomalous transport is still the subject of ongoing debate.

Modern Hall discharges developed for space propulsion operate in a quasisteady mode, i.e., in some operating regimes, the discharge current can fluctuate by as much as 50% or more of its mean value.³ Furthermore, they exhibit a rich spectrum of fluctuations in their plasma properties,⁴⁻⁸ with intense fluctuations occurring predominantly in the region where the $\mathbf{E} \times \mathbf{B}$ electron drift velocity is near its maximum.⁹ These plasma fluctuations are believed to be partly responsible for the anomalous electron transport across the magnetic field,^{3,4,9} and furthermore, these fluctuations impact the overall design of power supplies for propulsion applications.¹⁰

The characteristic spectrum of fluctuations in Hall discharges at lower frequencies (≤ 100 kHz) are particularly sensitive to operating conditions, such as the magnetic field strength and the applied discharge voltage. In a recent review article, Choueiri attempted to classify these disturbances when the magnetic field is varied.³ A similar demarcation between "operating modes" is seen when the magnetic field is held constant, and the applied voltage is varied.^{10,11} Figure 1 shows the variation in the spectral intensity of electron density fluctuations with discharge voltage, at the exit of an annular Hall discharge channel ($x=0$) where the magnetic field is a maximum. These spectral maps were generated with a Langmuir probe collecting ion saturation current.^{8,11} At very low voltages, when the discharge is operating in the so-called "ionization regime" (when current rises sharply with increased voltage—a regime characterized by an increasing ionization fraction with increased current), the fluctuations are predominantly narrow band and of relatively low frequency (5–20 kHz), although some weaker higher frequencies persist to beyond 100 kHz. At relatively high currents and high voltages, when the current saturates with increasing voltage (in the so-called "current saturation regime"), the fluctuations have similar spectral characteristics, but the strong features at low frequency are noticeably shifted from those at lower voltages. At moderate voltages, say 120 V (in the "transition regime"), the discharge abruptly transitions from the ionization to current saturation regimes. Here we see that the plasma is relatively quiescent at this location, with the exception of the strong disturbance at 15–20 kHz.

The disturbances are known to be quite dependent on the location within the plasma discharge channel. Figure 2 shows the variation in the spectral intensity of the electron density disturbances with axial position within the annular discharge channel, for the same general conditions of Fig. 1, but at a discharge voltage of 100 V. With the exception

^{a)} Author to whom correspondence should be addressed; electronic mail: cap@leland.stanford.edu

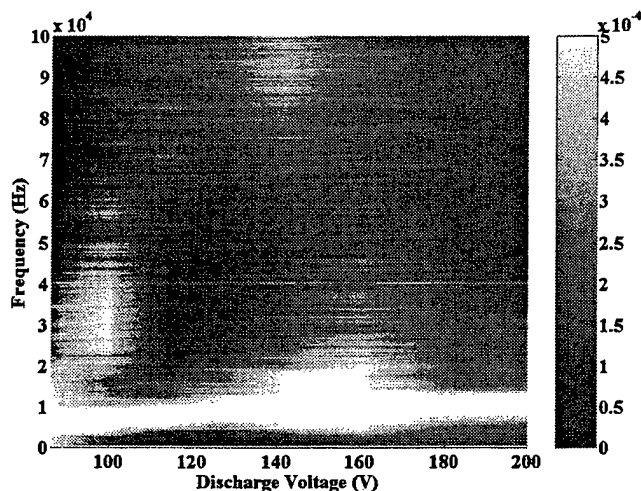


FIG. 1. Spectral map of disturbances in plasma density at the discharge exit for various operating voltages. The peak magnetic field is 100 G, and the xenon mass flow rate is 3 mg/s.

perhaps of the narrow-band 5–15 kHz disturbance, we see that the disturbances are fairly broadband, ranging from 20 to 100 kHz, and concentrated largely near the exit plane, near where the radial component of the magnetic field is strongest, and perhaps in the region where the gradient in the magnetic field is negative.¹¹ These broadband disturbances are easily separated from the lower frequency narrower band features, suggesting that these two waves are of different origins and character. A further difference is seen between frequency-position renderings of the fluctuations for other operating voltages¹¹ suggesting that the nature of the instabilities is quite sensitive to the regime of operation defined by the discharge voltage.

A comparison of the response of two probes located at the same axial position, but separated by some angle on the azimuth, provides additional information on the nature of these disturbances. Details of these measurements are provided in Ref. 11. A conditional cross-spectral analysis of the signals from the two probes provides a measure of their co-

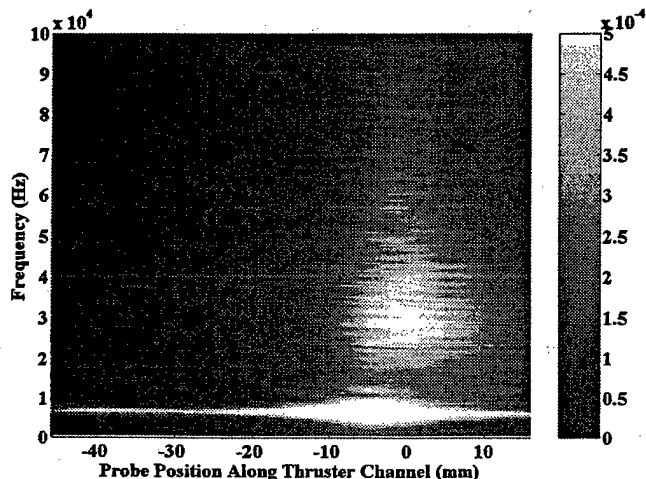


FIG. 2. Spectral map of disturbances in plasma density at various positions within the channel ($x=0$ corresponds to the channel exit, and $x=-80$ mm corresponds to the location of the anode).

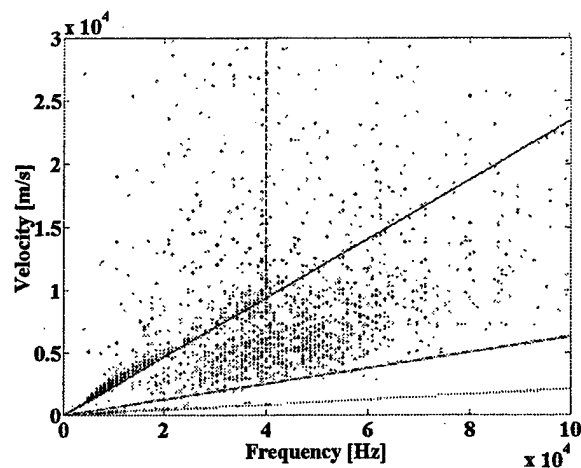


FIG. 3. Wave dispersion plot of plasma density disturbances detected at the exit plane of the discharge channel ($x=0$ mm), for a discharge voltage of 100 V, peak magnetic field of 100 G, and a mass flow rate of 3 mg/s. There is an apparent low frequency $m=1$ mode (solid line), high frequency $m=0$ modes (vertical dashed line), an $m=4$ cutoff (dashed line), and an $m=12$ probe-induced mode (dotted line).

herence, suggests the direction of propagation, and can be used to estimate the azimuthal phase velocity. Figure 3 shows a typical dispersion plot, for discharge conditions of Fig. 2, with the two probes separated by 30° along the azimuthal direction in a plane located at $x=0$ mm.

Four characteristic modes are identified in the dispersion plot. The most prominent is that of an azimuthally propagating mode ($m=1$ mode number, suggesting an azimuthal wavelength equal to the circumference of the channel, as indicated by the overlying solid line) of frequencies in the 5–20 kHz range, and of phase velocity $V_p \sim 1000$ –4000 m/s, nearly equal to the critical ionization velocity of the xenon propellant. The superimposed line is that which would be expected for an azimuthal $m=1$ mode with an out of plane tilt of 15° to the propagation vector. The spread of these disturbances above the $m=1$ line indicates that the tilt in the propagation direction is not unique for all frequencies. These waves are similar in behavior to those identified by Janes and Lowder² as “rotating spokes,” and are attributed to ionization waves of still unknown origin. A second prominent mode is that associated with nearly purely axial modes at higher frequency, one of which is identified on the figure by superimposing a vertical dashed line. While the behavior of these modes is consistent with an $m=0$ azimuthal mode, it could be higher-order modes that are propagating in the axial direction (the azimuthally spaced probes would not resolve this). These high frequency modes correspond to the nearly monochromatic bursts in Fig. 2. It is noteworthy that these disturbances are relatively broadband when averaged over time (i.e., they occur over a broad range of frequencies), and exhibit a curious $-5/3$ power-law behavior in their spectral energy density. Figure 4 displays the amplitude of the Fourier transform of the plasma density fluctuations for the 100 and 86 V cases, showing the power-law decay in the amplitudes at frequencies beyond 20 kHz.

The third mode, which is identifiable in Fig. 3, is that of an $m=12$ azimuthal wave (superimposed dotted line), which

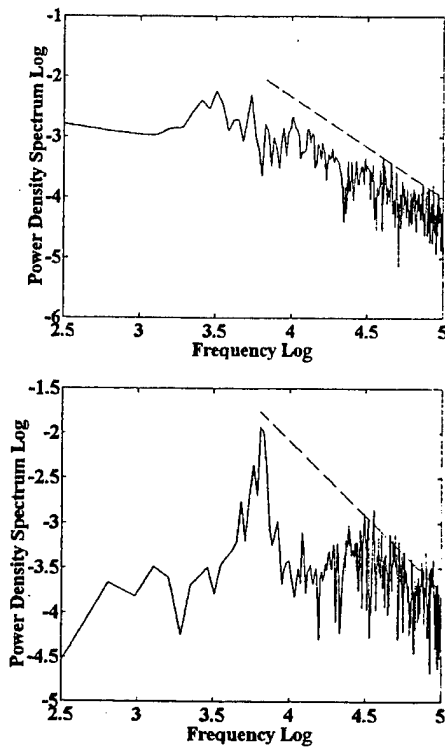


FIG. 4. Fourier spectra of the plasma density fluctuations for discharge conditions of 86 V (top) and 100 V (bottom). The power-law behavior beyond 20 kHz is apparent, and illustrated by the superimposed line.

has a wavelength equal to that of the separation between the two probes, and is believed to be “anchored” by the placement of the probes within the discharge annulus. The mode number of these disturbances is found to track the relative placement of the two probes used to study the intrinsic plasma fluctuations.¹¹ While the discovery of this induced perturbation may have potential applications in the control of thruster oscillations, we do not consider it further in this analysis, since it is not naturally excited within the discharge.

Finally, the fourth mode in Fig. 3 appears actually as a velocity limit to the higher frequency modes. It is identified in the figure as a dashed line corresponding to an $m=4$ mode. The origin of this clear demarcation is not presently understood, although we suspect that it is associated with an azimuthal asymmetry due to the four equally spaced magnetic solenoids that connect to the front outer pole piece. The persistence of this demarcation weakens at higher discharge voltages.¹¹ The interaction between the axial disturbances and the $m=4$ azimuthal asymmetry is the subject of ongoing research in our laboratory.

II. BACKGROUND

In this article, we present the results of a study aimed at developing an understanding of the low frequency oscillatory behavior of closed electron-drift Hall discharges. In prior theoretical research on the instabilities of these devices, most notably in earlier Russian literature,^{5,6} the emphasis was placed largely on understanding the origins of higher frequency azimuthal and longitudinal disturbances that were excited by magnetic-field gradient drifts. In almost all cases, simplifications were made to the governing equations so as

to derive closed-form analytical expressions for the dispersion relations for these waves and, almost exclusively, ionization, which is believed to be predominantly responsible for the low frequency disturbances that we observe at low discharge voltages (e.g., 80–125 V), and is usually neglected in these prior theoretical treatments.

One motivation for this work is to test the ability of a multifluid treatment of a Hall discharge to capture the oscillatory behavior seen in the laboratory. The success of such a test would lead to added confidence in the direct numerical solution of the fluid equations, or perhaps of a hybrid (fluid/particle) treatment in two or three dimensions,^{12,13} to further our understanding of these complex ionized plasma flows. In this article, we make use of an extensive and comprehensive experimental mapping of the background (time-averaged) plasma properties in a Hall discharge, which provides us with the necessary local background conditions for the theoretical stability analysis.¹⁴ We believe that at present, this is a better approach to understanding fluctuation phenomenon in Hall discharges, since a satisfactory theory for the “stationary” plasma properties do not exist, in part because of the inherent instabilities in these devices. We shall focus first at understanding low discharge voltage conditions (e.g., 100 V) for our particular Hall discharge,^{15–17} where we are on the ionization branch of the current–voltage ($I-V$) characteristics. Although this is not the “optimum” condition for operating a Hall discharge as a plasma propulsion source, it provides a starting point for a more complete analysis of the entire $I-V$ range, and is within an operating regime where we believe that the instabilities are coupled in some way to the ionization process.

III. FORMULATION OF THE PROBLEM

The coordinate geometry for the analysis is selected so that the x axis is along the thruster axis [along the direction of the applied electric field (E_0)], the y axis represents the azimuthal coordinate, with the azimuthal electron drift velocity in the negative y direction, and the z axis is along the thruster radius corresponding to the principle direction of the applied radial magnetic field B_0 . The plasma is assumed to be uniform in the z direction, and we restrict our attention to motion in the $x-y$ plane, rendering the problem to two dimensions.

The plasma behavior is governed by a set of 13 multi-fluid magnetohydrodynamic equations that describe the electron (subscript e), ion i , and neutral xenon n number densities (n_e, n_i, n_n), corresponding velocities (u, v, w), the electron temperature T_e , the components of the magnetic field along z , B_z , and the components of the electric field along x and y (E_x , and E_y). These equations are given below in vector form for completeness:

Electron species conservation

$$\frac{\partial n_e}{\partial t} + \nabla \cdot (n_e \mathbf{u}) = \alpha_i n_e n_n, \quad (1)$$

Ion species conservation

$$\frac{\partial n_i}{\partial t} + \nabla \cdot (n_i \mathbf{v}) = \alpha_i n_i n_n, \quad (2)$$

Neutral species conservation

$$\frac{\partial n_n}{\partial t} + \nabla \cdot (n_n \mathbf{w}) = -\alpha_i n_e n_n, \quad (3)$$

Electron momentum equation

$$n_e m \frac{\partial \mathbf{u}}{\partial t} + n_e m \mathbf{u} \cdot \nabla \mathbf{u} = -en_e \mathbf{E} - en_e \mathbf{u} \times \mathbf{B} - n_e m \bar{\nu}_{ei}(\mathbf{u} - \mathbf{v}) - n_e m \bar{\nu}_{en}(\mathbf{u} - \mathbf{w}), \quad (4)$$

Ion momentum equation

$$n_i M \frac{\partial \mathbf{v}}{\partial t} + n_i M \mathbf{v} \cdot \nabla \mathbf{v} = en_i \mathbf{E} - n_i m \bar{\nu}_{ei}(\mathbf{v} - \mathbf{u}) - n_i m_{in} \bar{\nu}_{in}(\mathbf{v} - \mathbf{w}), \quad (5)$$

Neutral momentum equation

$$n_n M \frac{\partial \mathbf{w}}{\partial t} + n_n M \mathbf{w} \cdot \nabla \mathbf{w} = -n_n m \bar{\nu}_{en}(\mathbf{w} - \mathbf{u}) - n_n m_{in} \bar{\nu}_{in}(\mathbf{w} - \mathbf{v}), \quad (6)$$

Electron energy equation

$$\frac{3}{2} n_e k_B \frac{\partial T_e}{\partial t} = en_e \mathbf{u} \cdot \mathbf{E} - \alpha_i n_e n_n \epsilon_i, \quad (7)$$

Ampere's law

$$\nabla \times \mathbf{B} = \frac{1}{c^2} \frac{\partial \mathbf{E}}{\partial t} + \mu_0 en(\mathbf{v} - \mathbf{u}), \quad (8)$$

Faraday's law

$$\nabla \times \mathbf{E} = -\frac{\partial \mathbf{B}}{\partial t}. \quad (9)$$

Here, α_i is the volumetric rate constant for ionization and $\bar{\nu}_{en}$ the averaged electron momentum transfer collision frequencies, which are determined from the known electron temperature, electron and neutral densities, and the ionization and momentum transfer cross sections for xenon.¹⁸ $\bar{\nu}_{ei}$ is the electron-ion momentum transfer collision frequency, calculated using the Spitzer-Harm expression,¹⁹ and $\bar{\nu}_{in}$ is the ion-neutral momentum transfer collision frequency, approximated using a constant cross section determined from the molecular diameter of xenon. The ionization rate and collision frequencies are taken to be time independent, allowing a linearization of the equations in plasma and neutral density, and so the ionization instabilities captured here are driven to first order by fluctuations only in the plasma density. The other variables in the governing equations are the electron charge and mass e and m , the ion and neutral xenon mass M , the reduced mass m_{in} , the speed of light c , Boltzmann constant k_B , the permeability of free space μ_0 , and the ionization energy of xenon ϵ_i .

In addition to the volumetric source of ionization, we model the radial transport of electrons and ions as driven primarily by the loss of electrons/ions at the channel wall. As a result, the electron and ion continuity equations are rewritten to show an explicit dependence on the wall loss rate ν_{wall}

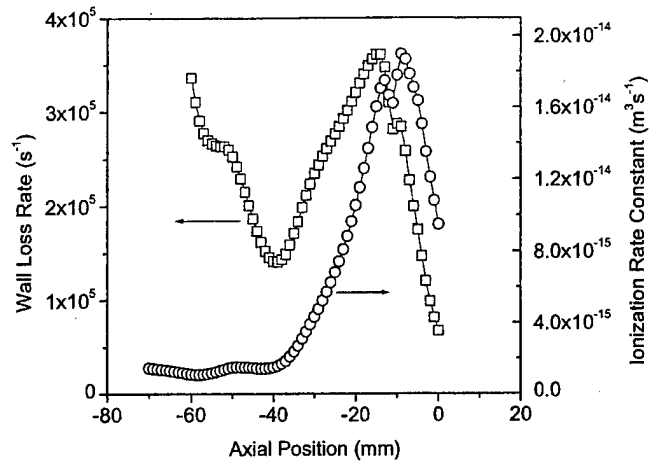


FIG. 5. Empirically determined ionization rate constant and wall loss rates for the low voltage (100 V) discharge conditions.

$$\frac{\partial n_e}{\partial t} + \frac{\partial n_e u_x}{\partial x} + \frac{\partial n_e u_y}{\partial y} = \alpha_i n_e n_n - n_e \nu_{wall}, \quad (10a)$$

$$\frac{\partial n_i}{\partial t} + \frac{\partial n_i v_x}{\partial x} + \frac{\partial n_i v_y}{\partial y} = \alpha_i n_e n_n - n_e \nu_{wall}, \quad (10b)$$

In expressing the continuity equations in this way, we assume that there is a net loss of charge at the wall, controlled largely by the electron diffusion. While the net wall loss rate is expected to depend in a complex way on the secondary electron emission process, we determine its value experimentally, from the measured axial variations in the background plasma properties, and from the computed volumetric ionization rate constant (assuming a Maxwellian electron energy distribution at the measured electron temperature):

$$\nu_{wall} = \alpha_i n_n - \frac{1}{en_e} \frac{dJ_e}{dx}. \quad (11)$$

The spatial variation in the ionization rate constant and the wall loss rate are shown in Fig. 5 for the 100 V discharge condition.

IV. STABILITY ANALYSIS

In general, for the case of an initially axially nonuniform plasma, a stability analysis would require the solution of a set (13 in this case) of homogeneous ordinary differential equations for the perturbation amplitudes, obtained by assuming a perturbation of the form

$$f = f_0(x) + f_1(x, y) e^{-i\omega t}, \quad (12)$$

where f is the plasma property of interest, f_0 is the steady-state background property value dependent on position for the nonuniform plasma case, and f_1 is its small perturbation amplitude (which can also depend on position and the mode frequency). In this study, we shall simplify the analysis by assuming that the plasma is initially uniform in the azimuthal direction y , and that the characteristic length of the axial perturbations ($\sim \lambda_x$, the wavelength component along x) are smaller than the characteristic length scale over which the background properties change, i.e.,

$$\lambda_x < \left(\frac{1}{f_0} \frac{\partial f_0}{\partial x} \right)^{-1}. \quad (13)$$

This scale length is approximately the length of the discharge channel (~ 8 cm) but, in some cases, is best characterized by the length of the ionization zone (~ 2 cm). Under these conditions, the problem reduces to a homogeneous set of linear, algebraic equations with

$$f_1(x, y, t) = \hat{f}_1 e^{i(k_x x + k_y y - \omega t)}, \quad (14)$$

where $\hat{f}_1(\omega)$ is the mode frequency-dependent amplitude of the perturbation. Although simplified, this first approach leads to a direct comparison between the predicted and observed azimuthal and axial mode propagation behavior at various locations within the discharge channel. The analysis results in the prediction of linear perturbation amplitudes and frequencies that may depend on position. In the analysis, gradients in these background properties are evaluated explicitly, based on their local values, determined experimentally.¹⁴

The resulting set of linear homogeneous equations is (where we have dropped the $\hat{}$ symbol over the perturbation amplitudes for clarity):

Electron species conservation

$$\begin{aligned} & (-i\omega + u_{0y}ik_y - \alpha_i n_{0n} + \nu_{\text{wall}}) \cdot n_{1e} - \alpha_i n_{0e} \cdot n_{1n} \\ & + \left(i\omega \frac{mn_{0e}}{eB_{0z}^2} \frac{\partial B_{0z}}{\partial x} - i\omega \frac{m}{eB_{0z}} \frac{\partial n_{0e}}{\partial x} - ik_y \frac{mu_{0y}n_{0e}}{eB_{0z}^2} \frac{\partial B_{0z}}{\partial x} \right. \\ & + ik_y \frac{mu_{0y}}{eB_{0z}} \frac{\partial n_{0e}}{\partial x} + ik_y \frac{mn_{0e}}{eB_{0z}} \frac{\partial u_{0y}}{\partial x} \left. \right) \cdot u_{1y} - ik_y \frac{n_{0e}}{B_{0z}} \cdot E_{1x} \\ & + \left(\frac{1}{B_{0z}} \frac{\partial n_{0e}}{\partial x} + ik_x \frac{n_{0e}}{B_{0z}} - \frac{n_{0e}}{B_{0z}^2} \frac{\partial B_{0z}}{\partial x} \right) \cdot E_{1y} \\ & - ik_y \frac{n_{0e}u_{0y}}{B_{0z}} \cdot B_{1z} = 0, \end{aligned} \quad (15)$$

Ion species conservation

$$\begin{aligned} & \left(-i\omega + v_{0x}ik_x + \frac{\partial v_{0x}}{\partial x} - \alpha_i n_{0n} \right) \cdot n_{1i} + \nu_{\text{wall}} \cdot n_{1e} - \alpha_i n_{0i} \cdot n_{1n} \\ & + \left(n_{0i}ik_x + \frac{\partial n_{0i}}{\partial x} \right) \cdot v_{1x} + n_{0i}ik_y \cdot v_{1y} = 0, \end{aligned} \quad (16)$$

Neutral species conservation

$$\begin{aligned} & \alpha_i n_{0n} \cdot n_{1e} + \left(-i\omega + w_{0x}ik_x + \frac{\partial w_{0x}}{\partial x} + \alpha_i n_{0e} \right) \cdot n_{1n} \\ & + \left(n_{0n}ik_x + \frac{\partial n_{0n}}{\partial x} \right) \cdot w_{1x} + n_{0n}ik_y \cdot w_{1y} = 0, \end{aligned} \quad (17)$$

Electron momentum equation (along x)

$$\begin{aligned} & -\bar{v}_{ei} \cdot v_{1x} + (-i\omega + u_{0y}ik_y + \bar{v}_{ei} + \bar{v}_{en}) \cdot u_{1x} + \frac{e}{m} B_{0z} \cdot u_{1y} \\ & -\bar{v}_{en} \cdot w_{1x} + \frac{e}{m} E_{1x} + \frac{e}{m} u_{0y} \cdot B_{1z} = 0, \end{aligned} \quad (18)$$

Electron momentum equation (along y)

$$\begin{aligned} & -\bar{v}_{ei} \cdot v_{1y} - \frac{e}{m} B_{0z} \cdot u_{1x} + (-i\omega + u_{0y}ik_y + \bar{v}_{ei} + \bar{v}_{en}) \cdot u_{1y} \\ & -\bar{v}_{en} \cdot w_{1y} + \frac{e}{m} E_{1y} = 0, \end{aligned} \quad (19)$$

Ion momentum equation (along x)

$$\begin{aligned} & \left(-i\omega + v_{0x}ik_x + \frac{\partial v_{0x}}{\partial x} + \frac{m}{M} \bar{v}_{ie} + \frac{m_{in}}{M} \bar{v}_{in} \right) \cdot v_{1x} - \frac{m}{M} \bar{v}_{ie} \cdot u_{1x} \\ & - \frac{m_{in}}{M} \bar{v}_{in} \cdot w_{1x} - \frac{e}{M} E_{1x} = 0, \end{aligned} \quad (20)$$

Ion momentum equation (along y)

$$\begin{aligned} & \left(-i\omega + v_{0x}ik_x + \frac{m}{M} \bar{v}_{ie} + \frac{m_{in}}{M} \bar{v}_{in} \right) \cdot v_{1y} - \frac{m}{M} \bar{v}_{ie} \cdot u_{1y} \\ & - \frac{m_{in}}{M} \bar{v}_{in} \cdot w_{1y} - \frac{e}{M} E_{1y} = 0, \end{aligned} \quad (21)$$

Neutral momentum equation (along x)

$$\begin{aligned} & -\frac{m_{ni}}{M_n} \bar{v}_{ni} \cdot v_{1x} - \frac{m}{M_n} \bar{v}_{ne} \cdot u_{1x} \\ & + \left(-i\omega + w_{0x}ik_x + \frac{\partial w_{0x}}{\partial x} + \frac{m}{M_n} \bar{v}_{ne} + \frac{m_{ni}}{M_n} \bar{v}_{ni} \right) \\ & \cdot w_{1x} = 0, \end{aligned} \quad (22)$$

Neutral momentum equation (along y)

$$\begin{aligned} & -\frac{m_{ni}}{M_n} \bar{v}_{ni} \cdot v_{1y} - \frac{m}{M_n} \bar{v}_{ne} \cdot u_{1y} \\ & + \left(-i\omega + w_{0x}ik_x + \frac{m}{M_n} \bar{v}_{ne} + \frac{m_{ni}}{M_n} \bar{v}_{ni} \right) \cdot w_{1y} = 0, \end{aligned} \quad (23)$$

Electron energy equation

$$\begin{aligned} & \frac{2\alpha_i n_{0n} \epsilon_i}{3k_B n_{0e}} \cdot n_{1e} + \frac{2\alpha_i \epsilon_i}{3k_B} \cdot n_{1n} - \frac{2eE_{0x}}{3k_B} \cdot u_{1x} - \frac{2eu_{0y}}{3k_B} \cdot E_{1y} \\ & - i\omega \cdot T_{1e} = 0, \end{aligned} \quad (24)$$

Ampere's law (along x)

$$\begin{aligned} & \frac{1}{\epsilon_0} ev_{0x} \cdot n_{1i} + \frac{1}{\epsilon_0} en_{0i} \cdot v_{1x} - \frac{1}{\epsilon_0} en_{0i} \cdot u_{1x} - \omega i E_{1x} \\ & - \frac{1}{\epsilon_0 \mu_0} ik_y B_{1z} = 0, \end{aligned} \quad (25)$$

Ampere's law (along y)

$$\begin{aligned} & -\frac{1}{\epsilon_0} eu_{0y} \cdot n_{1e} + \frac{1}{\epsilon_0} en_{0i} \cdot v_{1y} - \frac{1}{\epsilon_0} en_{0i} \cdot u_{1y} - \omega i E_{1y} \\ & + \frac{1}{\epsilon_0 \mu_0} ik_x B_{1z} = 0, \end{aligned} \quad (26)$$

Faraday's law (along z)

$$-ik_y E_{1x} + ik_x E_{1y} - i\omega B_{1z} = 0. \quad (27)$$

The electron conservation equation is modified to be explicitly dependent on the gradient in the magnetic field by solving the electron momentum equations for the component velocities (neglecting collision terms), i.e.,

$$u_{1y} = -\frac{m}{eB_{0z}} \frac{\partial u_{1x}}{\partial t} - \frac{m}{eB_{0z}} u_{0y} \frac{\partial u_{1x}}{\partial y} - \frac{E_{1x}}{B_{0z}} - \frac{u_{0y}}{B_{0z}} B_{1z}, \quad (28a)$$

$$u_{1x} = \frac{m}{eB_{0z}} \frac{\partial u_{1y}}{\partial t} + \frac{m}{eB_{0z}} u_{0y} \frac{\partial u_{1y}}{\partial y} + \frac{E_{1y}}{B_{0z}}, \quad (28b)$$

and by substituting these back into the electron species equation. In this way, we are able to capture any magnetic field-gradient driven modes in a manner similar to that suggested by Esipchuck and Tiliin.⁶ However, in our case, we have also kept for now terms associated with gradients in other plasma properties and also terms associated with the electron inertia, although these inertia terms are expected to be important for only very high frequency modes.

Our approach is to solve the so-called "temporal formulation" of the problem, where the wave vectors k_x and k_y are taken as real quantities, and solve the system of equations for the complex ω , searching through the roots for positive frequencies (real component of ω) and positive growth rates (imaginary component of ω). For purely azimuthal modes, we constrain $k_y = -m/r$ (negative sign since we are looking for disturbances propagating in the negative azimuthal direction), with $m=1$ (to be consistent with what is seen experimentally) and $r=4$ cm, the radius of the midpoint of the annular discharge channel. For predominantly azimuthal waves with small propagation angles α out of the azimuthal plane, we use $k_x = k_y \tan(\alpha)$ for the out of plane component of the wave vector. For our particular discharge channel, we find that we satisfy the weak axial nonuniformity condition above provided that $20^\circ \geq \alpha \geq 70^\circ$. For other propagation angles, the axial component of the wavelength is comparable to and slightly greater than the length of the channel, and so the results for these intermediate propagation angles must be interpreted cautiously.

To find the mode frequencies, we solve a generalized eigenvalue problem of the form

$$\left[\frac{1}{i} \Lambda - \omega I \right] \hat{\mathbf{f}}_1 = 0, \quad (29a)$$

where the vector describing the perturbation amplitudes is

$$\hat{\mathbf{f}}_1 = [n_{1e}, n_{1i}, n_{1n}, u_{1x}, u_{1y}, v_{1x}, v_{1y}, w_{1x}, w_{1y}, T_{1e}, E_{1x}, E_{1y}, B_{1z}] \quad (29b)$$

and all of the elements of the coefficient matrix A are functions of the axial position, known from experiments. Here, I is the identity matrix. For each eigenmode representing a nondamped physical instability, we can determine the corresponding set of perturbation amplitudes (and relative phases) as complex components of that specific eigenvector. It is noteworthy that to cast the equation set in this eigenvalue form, we had to neglect the local acceleration (inertia terms)

in the electron momentum equation. We find that for the low frequency modes of interest here, these terms do not affect the overall results of the calculation.

V. RESULTS

The eigenvalue problem was applied to the conditions for Hall discharge operation at low voltage (100 V), as described in Ref. 14. All of the background plasma properties needed to determine the coefficient matrix A are specified in that article, for the length of the entire discharge channel, extending to about 10 mm beyond the exit plane. Apart from the trivial solution ($\omega=0$), we generally find four modes very close to the electron plasma frequency ω_e ($\sim 10^{11}$ Hz), two modes very close to the lower hybrid frequency ($\sim 10^6$ – 10^7 Hz), three modes between 20 and 100 kHz, and three other modes between 1 and 15 kHz.

Of the lower frequency roots, there is usually only one root that satisfies the condition for unstable growth of the disturbance. In some cases, two roots are found, and that which has the largest growth rate is selected for display. The frequencies of these roots are found to depend strongly on both the axial position and on the propagation angle. A three-dimensional rendering of the frequency versus propagation angle and axial position is shown in Fig. 6(a). The corresponding growth rate and electron density amplitude are shown in Figs. 6(b) and 6(c). It is apparent from the figure that the disturbances at higher frequencies favor longitudinal propagation, whereas azimuthal propagation is largely associated with frequencies below 20 kHz, in qualitative agreement with what is seen experimentally. An examination of the amplitudes and growth rate also indicate that the disturbances are concentrated between the axial locations $x = -20$ and $x = 10$ mm, also in agreement with the experimentally measured plasma density fluctuations as seen in Fig. 2. A projection of all of the low frequency points on the frequency-axial position plane (see Fig. 7), shows that the lower frequency azimuthal waves extend throughout a greater region of the channel, whereas the higher frequency waves are concentrated mostly in the region between $x = -10$ mm and $x = 0$.

We find that the gradients in the background plasma properties have a significant influence on the resulting mode behavior. In the numerical calculation, we can selectively consider the gradients of certain properties, to see the influence that these gradients have on the resulting dynamical system. The results of turning off all of the gradients in the calculation are shown in Figs. 8 and 9. Although the qualitative appearance of the plots remain the same, a detailed inspection reveals that the axial gradients in properties, all of which are positive between $x = -20$ and $x = -5$ mm, promote low and high frequency activity in this region, whereas in the region beyond this (between $x = -5$ mm and $x = 10$ mm), there seems to be suppressed activity. In this region, the plasma density and magnetic field have negative axial gradients, but the ion velocity is strong and positive in its gradient.

To further understand how gradients influence the development of these instabilities, the calculations were repeated

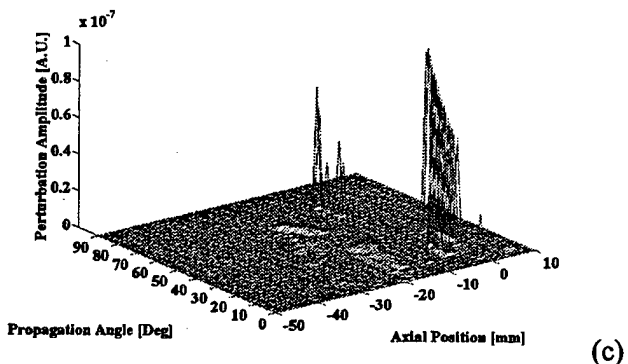
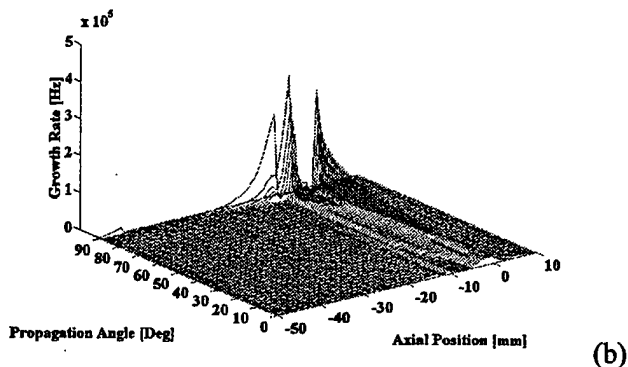
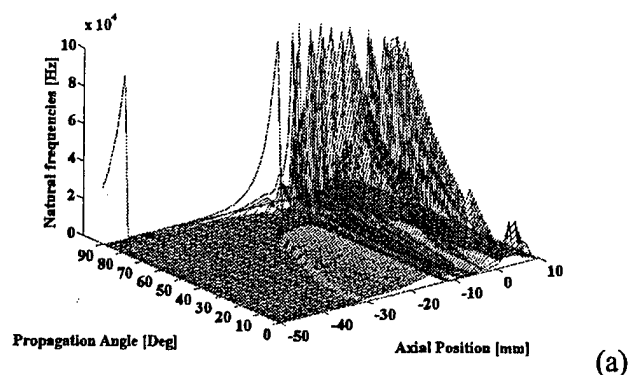


FIG. 6. Three-dimensional renderings of the results of the linear stability analysis for the low voltage (100 V) discharge conditions: (a) computed frequencies, (b) initial linear growth rates, and (c) electron density amplitude.

with only the plasma density and magnetic field gradients turned on. The frequencies are shown in Fig. 10 as projections onto the frequency-axial position plane for direct comparison to Figs. 7 and 9. It is quite apparent that the plasma density and magnetic field gradients promote the growth of the instabilities upstream of the location of the peak in the magnetic field, where these gradients have a positive value. On the other hand, they seem to have little, if any effect on the frequencies downstream of the peak in the magnetic field. It is noteworthy that turning on just the ion velocity gradient, which is strong in the region between $x = -10$ mm and $x = 10$ mm, seems to result in much reduced activity overall, and is most likely the cause of the absence of high frequencies seen beyond the exit plane ($x=0$) in Fig. 7.

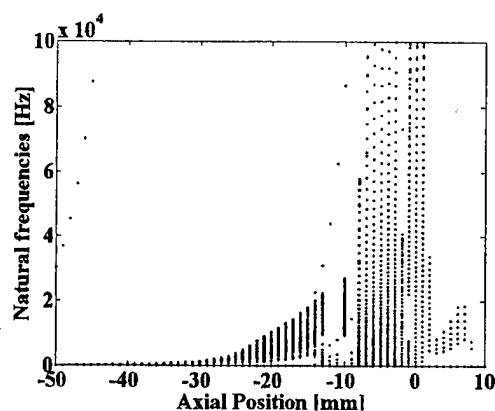


FIG. 7. Projection of the frequencies from Fig. 6(a) onto the frequency-axial position plane.

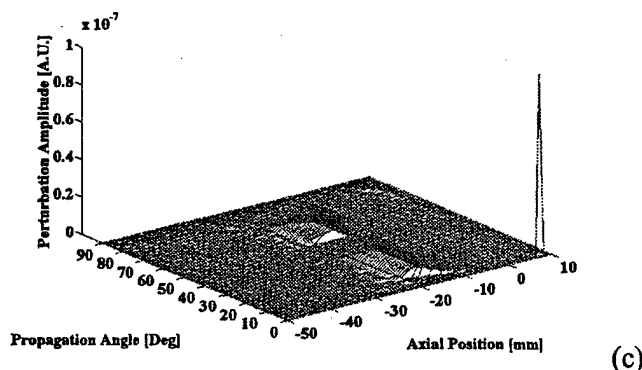
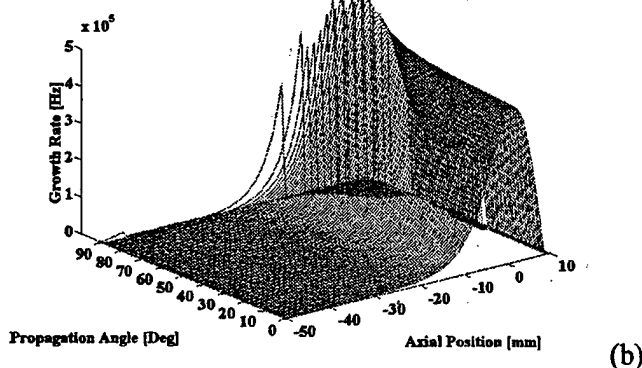
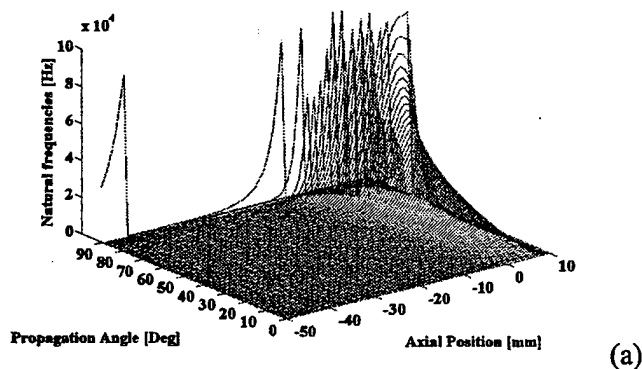


FIG. 8. Three-dimensional renderings as in Fig. 6, but with all of the axial plasma property gradients turned off.

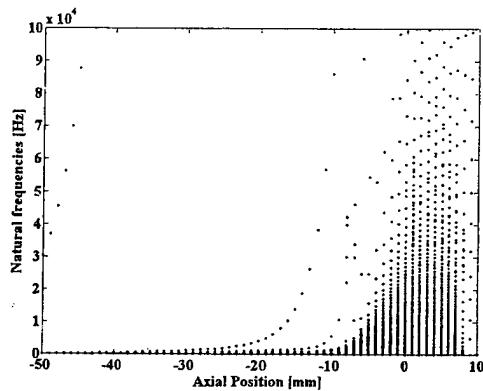


FIG. 9. Projection of the frequencies from Fig. 8 onto the frequency-axial position plane. All of the gradients in plasma properties have been turned off.

Finally, to identify the source of these instabilities, we examined the sensitivity of the computed frequencies, amplitudes, and growth rates to the volume ionization and wall loss source terms. The computed results for the case where all of the gradients are turned on, but with the ionization process turned off, are shown in Fig. 11. It is apparent from the figure that the instabilities nearly all but disappear, indicating that these instabilities are largely ionization waves driven in part by the axial inhomogeneities in the density and magnetic field.

While this analysis does not provide an analytical solution for the dispersion of these ionization instabilities, it provides the first clear indication of the importance of electrothermal processes such as ionization, in the dynamical behavior of these discharges, at least for the low voltage operation examined here. It confirms the conjecture that the low frequency azimuthally propagating “spokes” are ionization waves, as first suggested by Janes and Lowder.² It also supports the conjecture that the higher frequency longitudinally propagating disturbances (as denoted by the $m=0$ mode assignments in Fig. 3) are longitudinal ionization waves. The coupling between these longitudinal disturbances and the azimuthal asymmetry in plasma properties imposed by the location of the magnetic solenoids is yet to be resolved. Future theoretical analyses will concentrate on devel-

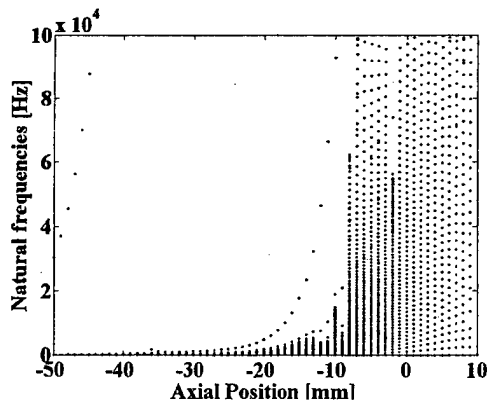
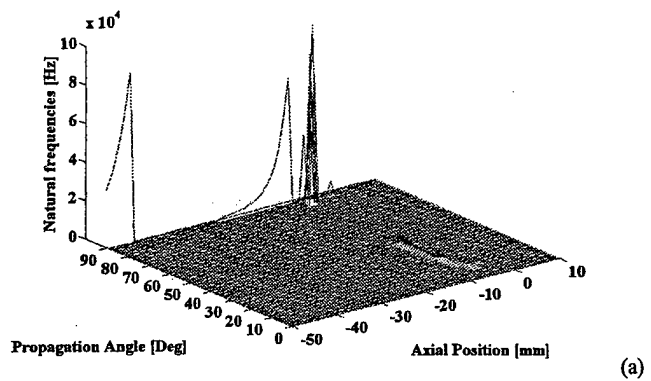
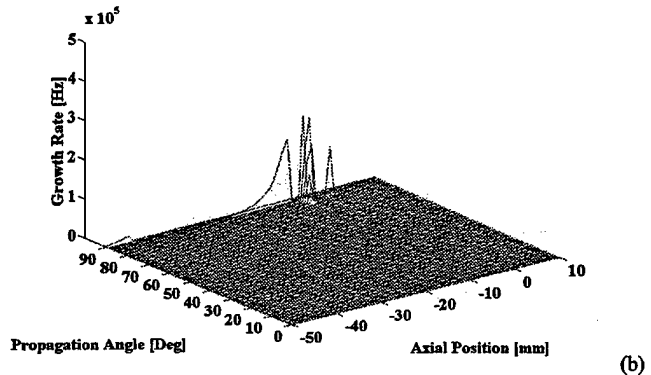


FIG. 10. Projection of the calculated frequencies onto the frequency-axial position plane. Only gradients in the radial magnetic field and plasma density have been turned on.



(a)



(b)

FIG. 11. Three-dimensional renderings of: (a) computed frequencies and (b) growth rate, with all of the axial plasma property gradients turned on but with the electron and ion source term (ionization and wall loss) turned off.

oping a simple analytical understanding of these ionization instabilities now that possible sources, which influence their dynamical behavior, have been partially clarified.

VI. SUMMARY

The availability of experimental data on the background (time-averaged) plasma properties within a Hall discharge has permitted a study of the response of this plasma to linear perturbations in its properties. A two-dimensional multifluid description accounting for electron heating is used as the basis for the unsteady analysis. The disturbances are constrained such that only the $m=1$ azimuthal mode is excited. The growth rate and frequencies of predominantly axial and azimuthally propagating plasma disturbances are obtained by numerical solution of the resulting eigenvalue problem under a quasiuniform plasma condition, along the entire discharge channel. The results identify the persistence of a low frequency instability that is associated with the ionization process, concentrated largely in the vicinity of the exit plane, where the magnetic field is at its maximum value, consistent with experimental observations for the relatively low operating voltages (~ 100 V) considered in this study.

ACKNOWLEDGMENTS

This work is supported by the Air Force Office of Scientific Research. Support for N.M. was provided by the National Defense Science and Engineering Graduate (NDSEG) fellowship. Additional support for E.C. was provided by the

Politecnico di Torino, Italy, and by the Ecole Centrale Paris, France. The authors are grateful for the many stimulating discussions with E. Fernandez.

- ¹E. A. Pinsley, C. O. Brown, and C. M. Banas, *J. Spacecr. Rockets* **1**, 525 (1964).
- ²G. S. Janes and R. S. Lowder, *Phys. Fluids* **9**, 1115 (1966).
- ³E. Y. Choueiri, 30th AIAA Joint Propulsion Conference, Indianapolis, 1994, Paper AIAA-94-3013.
- ⁴G. N. Tilinin, *Sov. Phys. Tech. Phys.* **22**, 974 (1977).
- ⁵A. I. Morozov, Y. V. Esipchuk, A. M. Kapulkin, V. A. Nevrovskii, and V. A. Smirnov, *Sov. Phys. Tech. Phys.* **17**, 482 (1972).
- ⁶Y. V. Esipchuk and G. N. Tilinin, *Sov. Phys. Tech. Phys.* **21**, 417 (1976).
- ⁷Y. V. Esipchuk, A. I. Morozov, G. N. Tilinin, and A. V. Trofimov, *Sov. Phys. Tech. Phys.* **18**, 339 (1973).
- ⁸D. P. Schmidt, N. B. Meezan, and M. A. Cappelli, 30th AIAA Plasma Dynamics and Lasers Conference, Norfolk, VA, 1999, Paper AIAA 99-3437.
- ⁹M. A. Cappelli, W. A. Hargus, Jr., and N. B. Meezan, *IEEE Trans. Plasma Sci.* **27**, 96 (1999).
- ¹⁰N. Gascon, C. Perot, G. Bonhomme, X. Caron, S. Bechu, P. Lasgorceix, B. Izrar, and M. Dudeck, 35th AIAA Joint Propulsion Conference, Los Angeles, CA, 1999, Paper AIAA-99-2427.
- ¹¹E. Chesta, C. Lam, N. B. Meezan, D. P. Schmidt, and M. A. Cappelli, *IEEE Trans. Plasma Sci.* (submitted).
- ¹²J. M. Fife, M. Martinez-Sanchez, and J. J. Szabo, 33rd AIAA Joint Propulsion Conference, Seattle, WA, 1997, Paper AIAA-97-3052.
- ¹³J. P. Boeuf and L. Garrigues, *J. Appl. Phys.* **84**, 3541 (1998).
- ¹⁴N. B. Meezan, W. A. Hargus, Jr., and M. A. Cappelli, *Phys. Rev. E* (submitted).
- ¹⁵N. B. Meezan, W. A. Hargus, Jr., and M. A. Cappelli, 34th Joint Propulsion Conference, Cleveland, OH, 1998, AIAA Paper 98-3502.
- ¹⁶W. A. Hargus, Jr. and M. A. Cappelli, 34th Joint Propulsion Conference, Cleveland, OH, 1998, AIAA 98-3645.
- ¹⁷N. B. Meezan and M. A. Cappelli, 35th AIAA Joint Propulsion Conference, Los Angeles, CA, 1999, Paper 99-2284.
- ¹⁸CPAT and Kinema Software, www.csn.net/siglo (1998).
- ¹⁹F. F. Chen, *Plasma Physics and Controlled Fusion*, 2nd ed. (Plenum, New York, 1985), p. 352.

Appendix V

A Low-Power, Linear-Geometry Hall Plasma Source with an Open Electron-Drift

D.P. Schmidt, N.B. Meezan, W.A. Hargus, Jr., and M.A. Cappelli

Plasma Sources Sci. Technol. **9**, 68-76, 2000

A low-power, linear-geometry Hall plasma source with an open electron-drift

D P Schmidt, N B Meezan, W A Hargus Jr and M A Cappelli†

Mechanical Engineering Department, Thermosciences Division, Stanford University, Stanford, CA 94305-3032, USA

Received 30 July 1999, in final form 6 December 1999

Abstract. This paper presents a discussion of the physics of modern Hall plasma thrusters and its impact on the design of new plasma thrusters of varying geometry and power. A particular emphasis is placed on the design and development of a linear-geometry (non-coaxial) source with an open electron-drift current. The operating characteristics of a linear-geometry Hall discharge scaled to operate in the 50 to 100 W power range are presented. Two thruster acceleration channels were fabricated—one of alumina and one of boron nitride. Differences in operation with the two channel materials are attributable to differences in the secondary electron emission properties. In either case, however, operation is achieved despite the lack of a closed electron current drift in the Hall direction, suggesting that there is an anomalous axial electron mobility, due to either plasma fluctuations or collisions with the channel wall. Strong low-frequency oscillations in the discharge current, associated with the depletion of propellant within the discharge, are seen to appear and vary with changes in the applied magnetic field strength. The frequency of this oscillatory mode is higher than that seen in larger (and higher power) discharges, due to the decreased residence time of the propellant within the channel.

1. Introduction

Hall discharge plasma accelerators have been considered for use in satellite propulsion since the early 1960s [1, 2]. In a Hall plasma source, a low-pressure discharge is sustained within a bounded dielectric channel in crossed electric and magnetic fields. Electrons emitted from a cathode external to the channel, or created by the ionization processes, drift along the channel towards the anode located at the channel base. The anode also serves as the source of neutral propellant (typically xenon). The radial component to the magnetic field is designed to be a maximum near the channel exit, and in this region, the electrons become highly magnetized, as the classical electron Hall parameter is much greater than unity. In typical Hall discharge plasma sources, the geometry is co-axial (figure 1) with an annular channel and surrounding solenoids generate a radial magnetic field. In this co-axial configuration, the electrons are constrained to move in the azimuthal direction of the closed $E \times B$ drift, with cross-field drift providing the necessary electron current to sustain the discharge. As the electron Hall parameter is much greater than unity, the Hall current density can be many orders of magnitude greater than the axial current density. According to classical electron transport theory, electrons can circle the annular channel in the Hall direction many times before being captured at the anode. A co-axial geometry therefore allows for this ‘closed’ electron

drift in the Hall direction, and uninterrupted Hall current. The region of trapped electrons acts as a volumetric zone of ionization that in some devices may occupy a small fraction of the overall channel length. The ions generated in this region, unaffected by the magnetic field because of their large inertia, are accelerated by the electric field resulting from the impeded electron flow, producing thrust. Very high ionization fractions and ion velocities can be generated with these discharges and, due to their high efficiencies and high specific impulse, Hall plasma thrusters in the 1–5 kW power range are being evaluated for use on commercial, military and research spacecraft [3].

A precise theory is lacking for the mechanism of cross-field electron transport in Hall plasma thrusters. Early experiments on Hall plasma sources indicated that classical electron transport theory could not account for the measured ‘anomalous’ axial (cross-field) electron current densities. Janes and Lowder [2] drew attention to the presence of density and electric field fluctuations within the channel of a Hall discharge, and first suggested that these plasma disturbances enhance the axial electron current. Indirect measurements of the ‘effective’ Hall parameter as a result of these fluctuations were in agreement with the anomalous transport coefficient first identified by Bohm *et al* [4], which characterizes the process now widely recognized as ‘anomalous’ Bohm diffusion [5]. The Bohm mechanism predicts an electron mobility that scales inversely with the magnetic field strength (as opposed to the classical B^{-2} scaling), and an effective

† Author to whom correspondence should be sent.

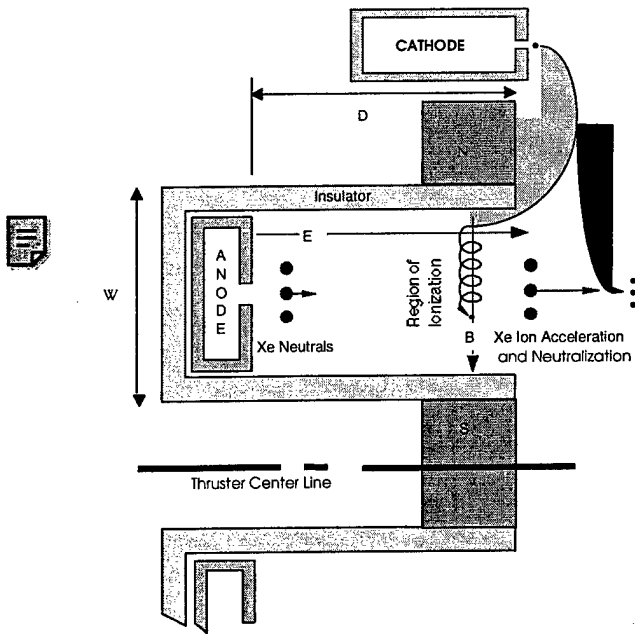


Figure 1. Schematic illustration of a typical co-axial Hall discharge.

electron Hall parameter of about 16. At conditions typical of Hall plasma thrusters near the region where the magnetic field is strongest, the classical Hall parameter is about 500–1000. A value of 16 represents a significant enhancement in the cross-field drift, and indicates that the ratio of Hall current density to axial current density may be much less than that suggested by classical transport theory. While an enhanced electron current due to fluctuations is one possible mechanism for enhanced electron transport, the operation of modern Hall plasma thrusters seems to depend significantly on the properties of the dielectric wall [6]. Previous researchers have proposed the possibility of an enhanced 'near-wall conductivity' due to the 'wall scattering' of electrons. While it seems the precise knowledge of which mechanism is responsible for transport is necessary to properly scale a Hall discharge, we show below that either of these mechanisms exhibits the necessary dependence on discharge parameters to achieve a desired scaling in discharge size or power.

Despite the progress that has been made in the development of co-axial Hall plasma thrusters that operate in the kilowatt power range, a need has developed for low-thrust, high-efficiency propulsion devices to be used for precise orbit control on small, power-limited satellites. A low-power (10–100 W) Hall thruster could fill this need. The proper scaling of a Hall plasma thruster for efficient operation at such low powers requires a renewed examination of the discharge physics that controls thruster performance. Also, alternative geometries that can potentially reduce thruster mass and/or size should be investigated. The scaling of co-axial Hall thrusters to lower powers has been discussed previously in the literature [7, 8]. To our knowledge, however, no one has reported on the operation of a Hall plasma source with a linear geometry and hence an open electron-drift. The

merits of a linear-geometry thruster are appealing, although any discharge model based on either classical or 'Bohm' electron transport indicates that even for moderate aspect ratios (depth to channel length ratio, D/L), such a geometry would interrupt the electron Hall current. A linear geometry allows compact packaging of the thruster in a limited space, making the magnetic circuit amenable to the use of permanent magnets. Also, a multiple array of linear thrusters could be efficiently stacked in order to extend the operating envelope of the propulsion system. This modular approach could be used to maintain operation at maximum efficiencies by simply turning stacked low-power linear thrusters on and off as needed to change the thrust level rather than by changing the operating point of a single thruster.

In this paper, we discuss the design and operation of a low-power linear-geometry Hall plasma thruster based on scaling arguments that we have presented previously [8]. The linear thruster tested here is scaled to operate at a power level that is 10–15% that of co-axial discharges built and tested in our laboratory in previous years [9, 10]. The linear-geometry, non-coaxial Hall plasma thruster has been fabricated and operated at near-design conditions. Operating characteristics are presented for both alumina and boron nitride acceleration channels for a range of peak magnetic field strengths.

2. Review of Hall thruster physics

Modern co-axial Hall plasma thrusters that operate in the 1–5 kW power range have been shown to operate with very high thrust efficiencies—around 50%. These thrusters have acceleration channel diameters ranging from 50 to 280 mm. One feature common to these thrusters is that the channel width (W) is approximately 15% of the outer diameter, which itself is about twice the acceleration channel depth (D). In scaling these discharges to operate at various power ranges, it is often desirable to preserve the geometrical relationship between channel width, diameter, and depth, although the physical basis for the commonly used geometrical parameters is not well understood.

In a typical Hall thruster, the magnetic field near the channel exit is sufficient to trap the electrons in cyclotron motion. The electron orbit radius (Larmor radius) is generally smaller than the electron mean free path λ and the acceleration channel width W . In this way, the electrons are confined to the magnetized portion of the plasma discharge. The Larmor radius, being dependent on particle mass, is much larger for ions, so they are largely unaffected by the magnetic field. The electron Larmor radius, r_e , scales as:

$$r_e \sim \frac{T_e^{1/2}}{B} \quad (1)$$

Here B is the magnetic field strength and T_e is the electron temperature. In the design of a low-power (and hence presumably smaller) discharge, a decrease in W requires a corresponding decrease in r_e . The magnetic field strength can be tailored for proper scaling; however, the electron temperature is not easily adjusted, as it is a consequence of a more complex relationship between geometry and operating conditions. The electron temperature is established

A low-power, linear-geometry Hall plasma source with an open electron-drift

D P Schmidt, N B Meezan, W A Hargus Jr and M A Cappelli†

Mechanical Engineering Department, Thermosciences Division, Stanford University, Stanford, CA 94305-3032, USA

Received 30 July 1999, in final form 6 December 1999

Abstract. This paper presents a discussion of the physics of modern Hall plasma thrusters and its impact on the design of new plasma thrusters of varying geometry and power. A particular emphasis is placed on the design and development of a linear-geometry (non-coaxial) source with an open electron-drift current. The operating characteristics of a linear-geometry Hall discharge scaled to operate in the 50 to 100 W power range are presented. Two thruster acceleration channels were fabricated—one of alumina and one of boron nitride. Differences in operation with the two channel materials are attributable to differences in the secondary electron emission properties. In either case, however, operation is achieved despite the lack of a closed electron current drift in the Hall direction, suggesting that there is an anomalous axial electron mobility, due to either plasma fluctuations or collisions with the channel wall. Strong low-frequency oscillations in the discharge current, associated with the depletion of propellant within the discharge, are seen to appear and vary with changes in the applied magnetic field strength. The frequency of this oscillatory mode is higher than that seen in larger (and higher power) discharges, due to the decreased residence time of the propellant within the channel.

1. Introduction

Hall discharge plasma accelerators have been considered for use in satellite propulsion since the early 1960s [1, 2]. In a Hall plasma source, a low-pressure discharge is sustained within a bounded dielectric channel in crossed electric and magnetic fields. Electrons emitted from a cathode external to the channel, or created by the ionization processes, drift along the channel towards the anode located at the channel base. The anode also serves as the source of neutral propellant (typically xenon). The radial component to the magnetic field is designed to be a maximum near the channel exit, and in this region, the electrons become highly magnetized, as the classical electron Hall parameter is much greater than unity. In typical Hall discharge plasma sources, the geometry is co-axial (figure 1) with an annular channel and surrounding solenoids generate a radial magnetic field. In this co-axial configuration, the electrons are constrained to move in the azimuthal direction of the closed $E \times B$ drift, with cross-field drift providing the necessary electron current to sustain the discharge. As the electron Hall parameter is much greater than unity, the Hall current density can be many orders of magnitude greater than the axial current density. According to classical electron transport theory, electrons can circle the annular channel in the Hall direction many times before being captured at the anode. A co-axial geometry therefore allows for this 'closed' electron

drift in the Hall direction, and uninterrupted Hall current. The region of trapped electrons acts as a volumetric zone of ionization that in some devices may occupy a small fraction of the overall channel length. The ions generated in this region, unaffected by the magnetic field because of their large inertia, are accelerated by the electric field resulting from the impeded electron flow, producing thrust. Very high ionization fractions and ion velocities can be generated with these discharges and, due to their high efficiencies and high specific impulse, Hall plasma thrusters in the 1–5 kW power range are being evaluated for use on commercial, military and research spacecraft [3].

A precise theory is lacking for the mechanism of cross-field electron transport in Hall plasma thrusters. Early experiments on Hall plasma sources indicated that classical electron transport theory could not account for the measured 'anomalous' axial (cross-field) electron current densities. Janes and Lowder [2] drew attention to the presence of density and electric field fluctuations within the channel of a Hall discharge, and first suggested that these plasma disturbances enhance the axial electron current. Indirect measurements of the 'effective' Hall parameter as a result of these fluctuations were in agreement with the anomalous transport coefficient first identified by Bohm *et al* [4], which characterizes the process now widely recognized as 'anomalous' Bohm diffusion [5]. The Bohm mechanism predicts an electron mobility that scales inversely with the magnetic field strength (as opposed to the classical B^{-2} scaling), and an effective

† Author to whom correspondence should be sent.

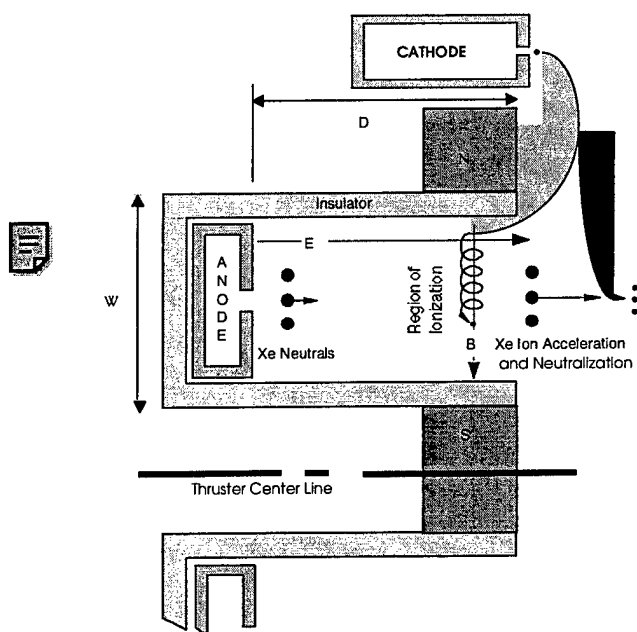


Figure 1. Schematic illustration of a typical co-axial Hall discharge.

electron Hall parameter of about 16. At conditions typical of Hall plasma thrusters near the region where the magnetic field is strongest, the classical Hall parameter is about 500–1000. A value of 16 represents a significant enhancement in the cross-field drift, and indicates that the ratio of Hall current density to axial current density may be much less than that suggested by classical transport theory. While an enhanced electron current due to fluctuations is one possible mechanism for enhanced electron transport, the operation of modern Hall plasma thrusters seems to depend significantly on the properties of the dielectric wall [6]. Previous researchers have proposed the possibility of an enhanced ‘near-wall conductivity’ due to the ‘wall scattering’ of electrons. While it seems the precise knowledge of which mechanism is responsible for transport is necessary to properly scale a Hall discharge, we show below that either of these mechanisms exhibits the necessary dependence on discharge parameters to achieve a desired scaling in discharge size or power.

Despite the progress that has been made in the development of co-axial Hall plasma thrusters that operate in the kilowatt power range, a need has developed for low-thrust, high-efficiency propulsion devices to be used for precise orbit control on small, power-limited satellites. A low-power (10–100 W) Hall thruster could fill this need. The proper scaling of a Hall plasma thruster for efficient operation at such low powers requires a renewed examination of the discharge physics that controls thruster performance. Also, alternative geometries that can potentially reduce thruster mass and/or size should be investigated. The scaling of co-axial Hall thrusters to lower powers has been discussed previously in the literature [7, 8]. To our knowledge, however, no one has reported on the operation of a Hall plasma source with a linear geometry and hence an open electron-drift. The

merits of a linear-geometry thruster are appealing, although any discharge model based on either classical or ‘Bohm’ electron transport indicates that even for moderate aspect ratios (depth to channel length ratio, D/L), such a geometry would interrupt the electron Hall current. A linear geometry allows compact packaging of the thruster in a limited space, making the magnetic circuit amenable to the use of permanent magnets. Also, a multiple array of linear thrusters could be efficiently stacked in order to extend the operating envelope of the propulsion system. This modular approach could be used to maintain operation at maximum efficiencies by simply turning stacked low-power linear thrusters on and off as needed to change the thrust level rather than by changing the operating point of a single thruster.

In this paper, we discuss the design and operation of a low-power linear-geometry Hall plasma thruster based on scaling arguments that we have presented previously [8]. The linear thruster tested here is scaled to operate at a power level that is 10–15% that of co-axial discharges built and tested in our laboratory in previous years [9, 10]. The linear-geometry, non-coaxial Hall plasma thruster has been fabricated and operated at near-design conditions. Operating characteristics are presented for both alumina and boron nitride acceleration channels for a range of peak magnetic field strengths.

2. Review of Hall thruster physics

Modern co-axial Hall plasma thrusters that operate in the 1–5 kW power range have been shown to operate with very high thrust efficiencies—around 50%. These thrusters have acceleration channel diameters ranging from 50 to 280 mm. One feature common to these thrusters is that the channel width (W) is approximately 15% of the outer diameter, which itself is about twice the acceleration channel depth (D). In scaling these discharges to operate at various power ranges, it is often desirable to preserve the geometrical relationship between channel width, diameter, and depth, although the physical basis for the commonly used geometrical parameters is not well understood.

In a typical Hall thruster, the magnetic field near the channel exit is sufficient to trap the electrons in cyclotron motion. The electron orbit radius (Larmor radius) is generally smaller than the electron mean free path λ and the acceleration channel width W . In this way, the electrons are confined to the magnetized portion of the plasma discharge. The Larmor radius, being dependent on particle mass, is much larger for ions, so they are largely unaffected by the magnetic field. The electron Larmor radius, r_e , scales as:

$$r_e \sim \frac{T_e^{1/2}}{B} \quad (1)$$

Here B is the magnetic field strength and T_e is the electron temperature. In the design of a low-power (and hence presumably smaller) discharge, a decrease in W requires a corresponding decrease in r_e . The magnetic field strength can be tailored for proper scaling; however, the electron temperature is not easily adjusted, as it is a consequence of a more complex relationship between geometry and operating conditions. The electron temperature is established

through a balance between ohmic dissipation, electron-particle collisions (including ionization), and electron-wall collisions. It was decided instead to scale the magnetic field strength as necessary and apply reasonable scaling arguments to preserve the mean electron energy from one design to another. It is seen from (1) that if the electron temperature is to be preserved in the scaling to lower powers, reducing the characteristic size of the thruster requires a concomitant increase in the operating magnetic field strength.

In a Hall discharge's use as a propulsion device, it is desirable to efficiently utilize the propellant, by achieving as high an ionization fraction possible. In scaling a higher power Hall discharge to lower powers, it is therefore desirable to preserve the ratio of the characteristic time to ionize the propellant to the residence time of the propellant in the discharge channel. The ionization time can be found from the inverse of the volumetric rate of ionization R_i , which scales linearly as the electron and neutral densities (n_e and n_a):

$$R_i = n_e n_a \alpha_i(T_e). \quad (2)$$

Here, $\alpha_i(T_e)$ is the temperature-dependent electron impact ionization rate coefficient. The characteristic time for ionization is $\tau_i = n_e/R_i$:

$$\tau_i = 1/n_a \alpha_i. \quad (3)$$

The residence time for a neutral atom can be found by dividing the acceleration channel depth D by the velocity of the neutrals, so it is expected to scale as:

$$\tau_R \sim D/T_a^{1/2}. \quad (4)$$

Here, T_a is the neutral xenon temperature, which is assumed to be relatively uniform, and which will largely control the gas dynamic behaviour of the neutrals within the channel. The ratio of these two parameters, the ionization time over the residence time, scales as

$$\frac{\tau_R}{\tau_i} \sim D n_a \quad (5)$$

where we assumed that the neutral xenon temperature (along with the electron temperature) is invariant to scale. As we shall see, this assumption regarding the invariance in T_a may be tenuous, since the xenon temperature will depend on the anode and channel wall temperatures, both of which are likely to be considerably higher for a low-power device because of the geometric scaling conclusions arrived at below. A consequence of (5) is that a geometric reduction in the channel depth requires a corresponding increase in the neutral density to preserve the ratio of time scales. As we shall see from the next section, this density increase is achieved by properly scaling the mass flow rate and the channel area.

The axial variation in the magnetic field is also known to have a large impact on discharge performance. In a modern co-axial Hall thruster, the radial magnetic field is sharply peaked near the exit of the acceleration channel, with a distribution width that is much less than the channel depth. A high magnetic field near the anode can lead to a large anode fall loss as electrons experience resistance to current flow. Since magnetic fields are difficult to shape, especially for co-axial designs, the depth of the channel is often dictated more

by the magnetic field distribution than geometric scaling of the channel length. An advantage of a linear geometry over a co-axial one is the ease at which a desired magnetic field distribution can be achieved with a less complicated magnetic circuit.

3. Thruster scaling implications

Based on the physics presented in the previous section, the scaling of the discharge is relatively straightforward. We treat the desired discharge voltage ϕ_d as a design parameter, as it directly determines the ion velocity (and hence specific impulse of the thruster), which is often dictated by the satellite mission objectives.

We continue with the assumption that the electron temperature can be preserved with proper scaling. This is justified if we can argue that for a reduction of the total power by some factor ζ , the rates of energy loss and thrust power are correspondingly reduced by the same factor. The reduction in discharge power without a reduction in the discharge voltage implies a reduction in the overall discharge current. However, for proper geometric scaling, the area is correspondingly reduced by the factor ζ^2 , so the current densities must be increased by the factor $1/\zeta$. The necessary scaling in the ion current density (and hence thrust power) is achieved if the plasma density is correspondingly increased, since the velocity is unchanged. The necessary scaling in the axial electron current density is achieved if the axial electron drift velocity, V_{ed} , is arguably scale-invariant. As we have discussed previously [8], both the anomalous Bohm transport and wall collisions will give rise to drift velocities that are scale-invariant. The axial drift velocity associated with Bohm transport is determined by the ratio of the electric field strength, E , to the magnetic field strength

$$V_{ed \text{ Bohm}} = \frac{e}{16B} E \sim \frac{E}{B} \quad (6)$$

which will be preserved through a geometric scaling. If the cross-field transport is largely controlled by wall collisions, then, for highly magnetized electrons ($\omega_{ce} = eB/m_e \gg \nu_{wall} = C_e/W$, the wall scattering frequency), the axial electron drift velocity is approximately

$$V_{ed \text{ Wall}} = \frac{eE\nu_{wall}}{m_e\omega_{ce}^2} \sim EW \quad (7)$$

which will also be preserved with the proper geometric scaling since the magnetic field scales as $B \propto 1/W$, as discussed earlier (here, C_e is the mean thermal electron speed, which is preserved if the temperature is preserved, and e and m_e are the charge and mass of the electron, respectively). The increased electron number density (by the factor $1/\zeta$) is achieved because the corresponding decrease in the mass flow rate results in an increase in n_a , since the area is decreased by the factor ζ^2 . This relies on the assumption that the ionization fraction is preserved, which is reasonable if the ratio of time scales presented in (5) is also preserved.

Finally, in order to preserve the electron temperature, we must argue that the electron energy loss rates will also scale in proportion to the decrease in power. It is easily shown that

the necessary scaling is obtained if the dominant energy loss mechanism is through wall collisions. It is noteworthy that volumetric ionization will also satisfy the scaling condition, since the energy loss rate through ionization is

$$E_i = n_e n_a \alpha_i V_c \varepsilon \sim \zeta. \quad (8)$$

Here, V_c is the channel volume and ε_i , the ionization energy of xenon.

One undesirable consequence of the geometric scaling for operation at reduced power levels is an increase in heat flux to the channel walls [7]. Since the power is reduced by the scaling factor ζ and the wall area reduced by ζ^2 , the heat flux to the walls will increase by a factor of $1/\zeta$. This scaling consequence may prove problematic for very low-power (and consequently reduced size) Hall plasma thrusters.

It is noteworthy that the decreased residence time of the neutral xenon in the channel (see (4)) should result in a shift to high frequencies in the characteristic breathing instability often seen in the 7–10 kHz frequency range in higher power devices [11]. While we predicted this shift in an earlier paper [8], the poor performance of the low-power thruster presented in that study precluded such a measurement. We have characterized the current oscillations in the discharge reported on here, and have found the oscillation frequencies to be consistent with the nearly $1/10$ scaling carried out in this study.

In summary, if it is desired to scale the power of a Hall thruster by some arbitrary factor ζ , then the characteristic scale lengths of the thruster and mass flow rates should be scaled by the same factor, ζ . The appropriate adjustment to the magnetic field (preserving its shape) is to increase it by the factor $1/\zeta$. With these scaling laws, according to the arguments presented above, the electron temperature should be preserved, as well as the ratio of electron current to ion current.

4. Linear geometry implications

In a weakly collisional steady-state plasma, where the electron Hall parameter satisfies the condition

$$\omega_{ce} \tau_e \gg 1 \quad (9)$$

the ratio of the cross-field (axial) electron current to the Hall current is

$$\frac{J_{ez}}{J_{eH}} = \frac{1}{\omega_{ce} \tau_e}. \quad (10)$$

Here, τ_e is the time between electron collisions. If we use the classical electron collision time in (9), we would find that for most modern thrusters, the resulting Hall parameter is typically in the range of 100–1000. Note that the current ratio described in (10) is a scale invariant in that the scaling laws introduced here would increase the electron cyclotron frequency in proportion to the decrease in the electron collision time. It is precisely this vast inequality between the axial and Hall currents which prompted the use of a co-axial design in early thrusters since, as mentioned above, a co-axial geometry with a closed electron drift allows the electrons to traverse the annulus many times prior to anode capture.

The presence of an anomalous electron transport mechanism, whether fluctuation or possibly wall-scattering induced, reduces the demand placed on the ratio of the Hall to axial electron current. A value of 16 for the 'effective' Hall parameter, as suggested by the anomalous Bohm mobility, still implies an electron drift direction that is predominantly in the direction of the crossed electric and magnetic field. However, we note that the value of 16 for the Bohm coefficient is strictly speculative, as the effective Hall parameters in modern Hall thrusters have not been accurately characterized, and coefficients within a factor of two or three of this value have been obtained for other plasma devices [5]. It is therefore conceivable that the Bohm coefficient can be less than this value. If so, then the necessity for a closed electron drift is removed, and with an adequate aspect ratio (ratio of channel length to channel depth), a linear Hall thruster with an open electron drift may perform equally well in comparison to closed-drift designs. However, even with an effective Hall parameter of unity, the linear design does impose an asymmetry in the electron flow, giving rise to expected asymmetric current densities within the channel that may impact on discharge performance.

5. Experiment

5.1. Test facility

The Stanford high vacuum test facility has been discussed extensively elsewhere [8–10]. It consists of a non-magnetic stainless steel tank approximately 1 m in diameter and 1.5 m in length. The facility is pumped by two 50 cm diffusion pumps, backed by a 425 l s^{-1} mechanical pump. The base pressure of the facility is approximately 10^{-6} Torr as measured by an ionization gauge uncorrected for mass species. Thruster testing at xenon flow rates of 2–5 sccm results in chamber background pressures in the region of 4×10^{-5} Torr. This indicates that the facility has a xenon gas pumping speed of around 2000 l s^{-1} . Propellant flow to the thruster anode and cathode is controlled by two Unit Instruments 1200 series mass flow controllers factory calibrated for xenon. The propellant used in this study was research grade (99.99%) xenon.

5.2. Linear Hall thruster

The design of the linear Hall thruster studied here is based on the scaling of a co-axial reference thruster recently built by our laboratory and operated at a nominal power of 400–700 W [12]. A scaling factor of $\zeta = 0.1$ was used in accordance with the scaling laws presented in the previous sections, although the performance of the magnetic circuit precluded the use of a channel depth that was one-tenth the depth of the reference coaxial discharge. The channel depth deviated from strict scaling laws in order to reduce the magnetic field strength at the anode, and hence the anode fall losses. A comparison of the coaxial thruster used for scaling and the linear thruster is shown in table 1. A schematic of the linear Hall thruster is shown in figure 2.

The magnetic circuit includes four 90 mm long electromagnet windings consisting of a 9.5 mm diameter core of commercially pure iron with 6 layers of 22 gauge

through a balance between ohmic dissipation, electron-particle collisions (including ionization), and electron-wall collisions. It was decided instead to scale the magnetic field strength as necessary and apply reasonable scaling arguments to preserve the mean electron energy from one design to another. It is seen from (1) that if the electron temperature is to be preserved in the scaling to lower powers, reducing the characteristic size of the thruster requires a concomitant increase in the operating magnetic field strength.

In a Hall discharge's use as a propulsion device, it is desirable to efficiently utilize the propellant, by achieving as high an ionization fraction possible. In scaling a higher power Hall discharge to lower powers, it is therefore desirable to preserve the ratio of the characteristic time to ionize the propellant to the residence time of the propellant in the discharge channel. The ionization time can be found from the inverse of the volumetric rate of ionization R_i , which scales linearly as the electron and neutral densities (n_e and n_a):

$$R_i = n_e n_a \alpha_i(T_e). \quad (2)$$

Here, $\alpha_i(T_e)$ is the temperature-dependent electron impact ionization rate coefficient. The characteristic time for ionization is $\tau_i = n_e/R_i$:

$$\tau_i = 1/n_a \alpha_i. \quad (3)$$

The residence time for a neutral atom can be found by dividing the acceleration channel depth D by the velocity of the neutrals, so it is expected to scale as:

$$\tau_R \sim D/T_a^{1/2}. \quad (4)$$

Here, T_a is the neutral xenon temperature, which is assumed to be relatively uniform, and which will largely control the gas dynamic behaviour of the neutrals within the channel. The ratio of these two parameters, the ionization time over the residence time, scales as

$$\frac{\tau_R}{\tau_i} \sim D n_a \quad (5)$$

where we assumed that the neutral xenon temperature (along with the electron temperature) is invariant to scale. As we shall see, this assumption regarding the invariance in T_a may be tenuous, since the xenon temperature will depend on the anode and channel wall temperatures, both of which are likely to be considerably higher for a low-power device because of the geometric scaling conclusions arrived at below. A consequence of (5) is that a geometric reduction in the channel depth requires a corresponding increase in the neutral density to preserve the ratio of time scales. As we shall see from the next section, this density increase is achieved by properly scaling the mass flow rate and the channel area.

The axial variation in the magnetic field is also known to have a large impact on discharge performance. In a modern co-axial Hall thruster, the radial magnetic field is sharply peaked near the exit of the acceleration channel, with a distribution width that is much less than the channel depth. A high magnetic field near the anode can lead to a large anode fall loss as electrons experience resistance to current flow. Since magnetic fields are difficult to shape, especially for co-axial designs, the depth of the channel is often dictated more

by the magnetic field distribution than geometric scaling of the channel length. An advantage of a linear geometry over a co-axial one is the ease at which a desired magnetic field distribution can be achieved with a less complicated magnetic circuit.

3. Thruster scaling implications

Based on the physics presented in the previous section, the scaling of the discharge is relatively straightforward. We treat the desired discharge voltage ϕ_d as a design parameter, as it directly determines the ion velocity (and hence specific impulse of the thruster), which is often dictated by the satellite mission objectives.

We continue with the assumption that the electron temperature can be preserved with proper scaling. This is justified if we can argue that for a reduction of the total power by some factor ζ , the rates of energy loss and thrust power are correspondingly reduced by the same factor. The reduction in discharge power without a reduction in the discharge voltage implies a reduction in the overall discharge current. However, for proper geometric scaling, the area is correspondingly reduced by the factor ζ^2 , so the current densities must be increased by the factor $1/\zeta$. The necessary scaling in the ion current density (and hence thrust power) is achieved if the plasma density is correspondingly increased, since the velocity is unchanged. The necessary scaling in the axial electron current density is achieved if the axial electron drift velocity, V_{ed} , is arguably scale-invariant. As we have discussed previously [8], both the anomalous Bohm transport and wall collisions will give rise to drift velocities that are scale-invariant. The axial drift velocity associated with Bohm transport is determined by the ratio of the electric field strength, E , to the magnetic field strength

$$V_{ed \text{ Bohm}} = \frac{e}{16B} E \sim \frac{E}{B} \quad (6)$$

which will be preserved through a geometric scaling. If the cross-field transport is largely controlled by wall collisions, then, for highly magnetized electrons ($\omega_{ce} = eB/m_e \gg \nu_{wall} = C_e/W$, the wall scattering frequency), the axial electron drift velocity is approximately

$$V_{ed \text{ Wall}} = \frac{eE\nu_{wall}}{m_e\omega_{ce}^2} \sim EW \quad (7)$$

which will also be preserved with the proper geometric scaling since the magnetic field scales as $B \propto 1/W$, as discussed earlier (here, C_e is the mean thermal electron speed, which is preserved if the temperature is preserved, and e and m_e are the charge and mass of the electron, respectively). The increased electron number density (by the factor $1/\zeta$) is achieved because the corresponding decrease in the mass flow rate results in an increase in n_a , since the area is decreased by the factor ζ^2 . This relies on the assumption that the ionization fraction is preserved, which is reasonable if the ratio of time scales presented in (5) is also preserved.

Finally, in order to preserve the electron temperature, we must argue that the electron energy loss rates will also scale in proportion to the decrease in power. It is easily shown that

the necessary scaling is obtained if the dominant energy loss mechanism is through wall collisions. It is noteworthy that volumetric ionization will also satisfy the scaling condition, since the energy loss rate through ionization is

$$E_i = n_e n_a \alpha_i V_c \varepsilon \sim \zeta. \quad (8)$$

Here, V_c is the channel volume and ε_i , the ionization energy of xenon.

One undesirable consequence of the geometric scaling for operation at reduced power levels is an increase in heat flux to the channel walls [7]. Since the power is reduced by the scaling factor ζ and the wall area reduced by ζ^2 , the heat flux to the walls will increase by a factor of $1/\zeta$. This scaling consequence may prove problematic for very low-power (and consequently reduced size) Hall plasma thrusters.

It is noteworthy that the decreased residence time of the neutral xenon in the channel (see (4)) should result in a shift to high frequencies in the characteristic breathing instability often seen in the 7–10 kHz frequency range in higher power devices [11]. While we predicted this shift in an earlier paper [8], the poor performance of the low-power thruster presented in that study precluded such a measurement. We have characterized the current oscillations in the discharge reported on here, and have found the oscillation frequencies to be consistent with the nearly $1/10$ scaling carried out in this study.

In summary, if it is desired to scale the power of a Hall thruster by some arbitrary factor ζ , then the characteristic scale lengths of the thruster and mass flow rates should be scaled by the same factor, ζ . The appropriate adjustment to the magnetic field (preserving its shape) is to increase it by the factor $1/\zeta$. With these scaling laws, according to the arguments presented above, the electron temperature should be preserved, as well as the ratio of electron current to ion current.

4. Linear geometry implications

In a weakly collisional steady-state plasma, where the electron Hall parameter satisfies the condition

$$\omega_{ce} \tau_e \gg 1 \quad (9)$$

the ratio of the cross-field (axial) electron current to the Hall current is

$$\frac{J_{ez}}{J_{eH}} = \frac{1}{\omega_{ce} \tau_e}. \quad (10)$$

Here, τ_e is the time between electron collisions. If we use the classical electron collision time in (9), we would find that for most modern thrusters, the resulting Hall parameter is typically in the range of 100–1000. Note that the current ratio described in (10) is a scale invariant in that the scaling laws introduced here would increase the electron cyclotron frequency in proportion to the decrease in the electron collision time. It is precisely this vast inequality between the axial and Hall currents which prompted the use of a co-axial design in early thrusters since, as mentioned above, a co-axial geometry with a closed electron drift allows the electrons to traverse the annulus many times prior to anode capture.

The presence of an anomalous electron transport mechanism, whether fluctuation or possibly wall-scattering induced, reduces the demand placed on the ratio of the Hall to axial electron current. A value of 16 for the 'effective' Hall parameter, as suggested by the anomalous Bohm mobility, still implies an electron drift direction that is predominantly in the direction of the crossed electric and magnetic field. However, we note that the value of 16 for the Bohm coefficient is strictly speculative, as the effective Hall parameters in modern Hall thrusters have not been accurately characterized, and coefficients within a factor of two or three of this value have been obtained for other plasma devices [5]. It is therefore conceivable that the Bohm coefficient can be less than this value. If so, then the necessity for a closed electron drift is removed, and with an adequate aspect ratio (ratio of channel length to channel depth), a linear Hall thruster with an open electron drift may perform equally well in comparison to closed-drift designs. However, even with an effective Hall parameter of unity, the linear design does impose an asymmetry in the electron flow, giving rise to expected asymmetric current densities within the channel that may impact on discharge performance.

5. Experiment

5.1. Test facility

The Stanford high vacuum test facility has been discussed extensively elsewhere [8–10]. It consists of a non-magnetic stainless steel tank approximately 1 m in diameter and 1.5 m in length. The facility is pumped by two 50 cm diffusion pumps, backed by a 425 l s^{-1} mechanical pump. The base pressure of the facility is approximately 10^{-6} Torr as measured by an ionization gauge uncorrected for mass species. Thruster testing at xenon flow rates of 2–5 sccm results in chamber background pressures in the region of 4×10^{-5} Torr. This indicates that the facility has a xenon gas pumping speed of around 2000 l s^{-1} . Propellant flow to the thruster anode and cathode is controlled by two Unit Instruments 1200 series mass flow controllers factory calibrated for xenon. The propellant used in this study was research grade (99.99%) xenon.

5.2. Linear Hall thruster

The design of the linear Hall thruster studied here is based on the scaling of a co-axial reference thruster recently built by our laboratory and operated at a nominal power of 400–700 W [12]. A scaling factor of $\zeta = 0.1$ was used in accordance with the scaling laws presented in the previous sections, although the performance of the magnetic circuit precluded the use of a channel depth that was one-tenth the depth of the reference coaxial discharge. The channel depth deviated from strict scaling laws in order to reduce the magnetic field strength at the anode, and hence the anode fall losses. A comparison of the coaxial thruster used for scaling and the linear thruster is shown in table 1. A schematic of the linear Hall thruster is shown in figure 2.

The magnetic circuit includes four 90 mm long electromagnet windings consisting of a 9.5 mm diameter core of commercially pure iron with 6 layers of 22 gauge

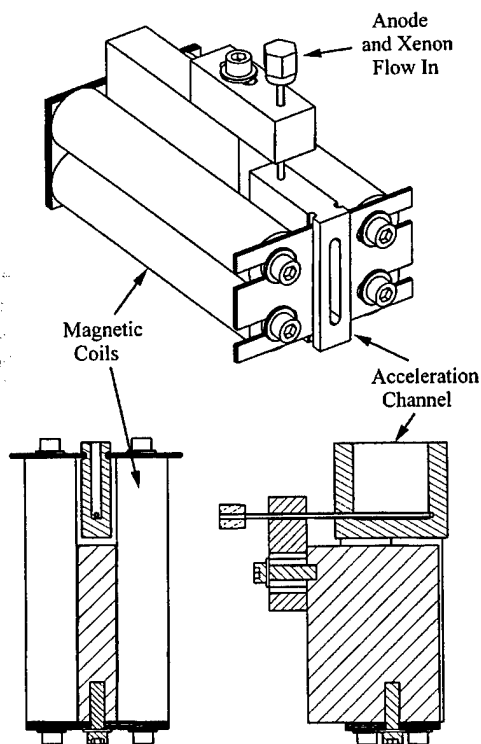


Figure 2. Schematic of the linear-geometry open electron-drift Hall discharge.

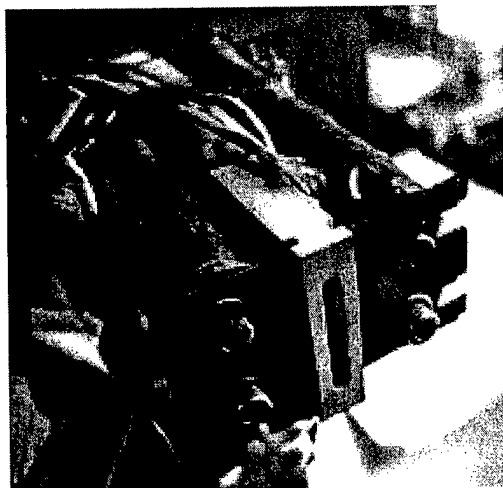


Figure 3. Photograph of the linear-geometry open electron-drift Hall discharge.

insulated copper magnet wire. The magnetic bottom plate is 3 mm thick silicon steel, whereas the magnetic top plate is 1.5 mm thick silicon steel. The discharge channel was fabricated in two versions, one constructed of high-purity alumina ceramic and the other of boron nitride. The anode is a 1.6 mm diameter stainless steel tube with 14 propellant holes, 0.2 mm in diameter spaced by 1.6 mm. A photograph of the thruster is shown in figure 3.

Linear-geometry Hall plasma source with an open electron-drift

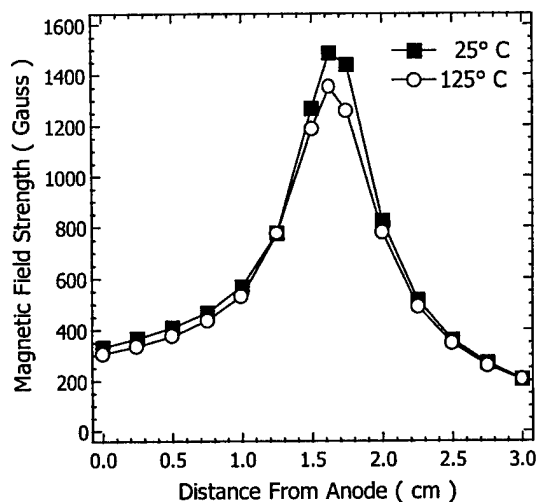


Figure 4. Transverse magnetic field strength variation with axial position. In both cases, the winding current is 1.25 A.

Measurements of the transverse component of the magnetic field show that the magnetic field near the anode is 23% of the peak value, which is located about 2 mm upstream of the channel exit. The measured field distribution for a winding current of 1.25 A is shown in figure 4 for two different temperatures. These measurements were obtained *ex situ*, by heating the entire thruster unit in an oven at ambient conditions while measuring the magnetic field strength. It can be seen that the peak value of 1500 G at room temperature drops to less than 1400 G with a 100 °C temperature rise. This is significant in that the temperature of the acceleration channel has been measured to be as high as 440 °C by embedded thermocouples during operation in the thruster fabricated out of boron nitride.

The cathode used to neutralize the ion beam and support the necessary electric field is an Ion Tech. Inc. HCN-252 hollow cathode. It is capable of supplying a maximum current of 5 A at xenon flow rates of 0.1 to 0.5 mg s⁻¹. It is mounted in front of the thruster such that the hollow cathode exit is 1 cm above the exit of the channel. The cathode is the exact same unit used in the higher power thrusters, and the flow rate used here is comparable to the flow rate through the thruster itself (2 sccm). We expect that the near exit plane xenon density due to the cathode flow will have a negative effect on the discharge performance. However, because the neutral gas density in this low power discharge is about a factor of 5–10 times that in the higher power prototype, the effect is expected to be no greater here than in the higher power version. No attempt at designing and fabricating an appropriately scaled cathode has been made, although the future development of low-power (< 50 W) Hall thrusters will rely on such a development.

The anode of the discharge is powered by a Sorensen SCR600-1.7 laboratory power supply capable of providing 600 V and 1.7 A. The anode also has a 4 Ω resistor in the power line to serve as ballast during initial start of the discharge. The cathode heating element is powered by a low voltage direct-current (DC) power supply capable of providing the 8.5 A required to heat the cathode for startup

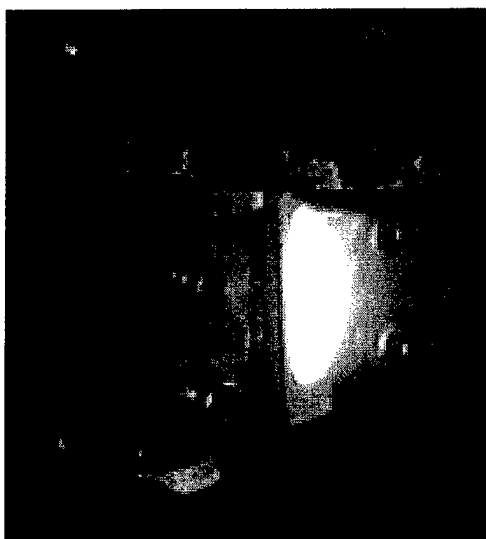


Figure 5. Photograph of the linear-geometry open electron-drift Hall discharge while operating.

and 4.0 A after start. The cathode flow rate of xenon was 2 sccm, a typical value used during operation of our higher power co-axial discharges. The cathode keeper uses a Sorensen SCR300-6 laboratory power supply to provide 250 V for initial cathode start and approximately 10 V and 250 mA during thruster operation. The power required for the magnetic circuit solenoids is provided by a Tektronix PS281 DC power supply operating in current limited mode.

The voltage and current of the thruster were recorded by acquiring data through a National Instruments PCI-5102 data acquisition card plugged into a desktop computer. A voltage divider was used so that the 5 V maximum voltage limit to the card was not exceeded while testing the thruster up to 250 V. The current was monitored by measuring the voltage drop across the 4 Ω ballast resistor.

6. Results and analysis

The thruster described was run at near-design conditions. To start the thruster, a glow discharge was initiated with the magnetic field turned off. With the power supply under current limit control and an upper limit set on the voltage, the magnetic field was increased. The discharge intensity greatly increased and changed colour from dull pink to a bright bluish emission as the magnetic field was increased, which is also typical of coaxial designs. A picture of the thruster running at design conditions is shown in figure 5. The voltage gradually increased until it reached the voltage limit setting. The power supply subsequently switched into voltage control, where most of the data reported was taken.

During operation at magnetic fields above 600 G, it was noted that the discharge was slightly asymmetric, being more intense near the side end of the channel in direction of the $E \times B$ electron drift. It was especially apparent during operation of the alumina thruster that this end wall became extremely hot and glowed intensely. This glow was contrasted to the bulk of the thruster channel, which did not show this intense

heating. On one occasion, after a few minutes of running the alumina thruster, the acceleration channel cracked along the edge of the glowing area. This failure was probably due to a high thermal stress caused by extreme temperature gradients in this region of the channel wall. Operation with the boron nitride thruster did not result in such a non-uniform temperature field on the insulating wall. This difference between the boron nitride and alumina insulators is attributed to the difference in the thermal conductivity values of the materials. The boron nitride channel end wall in the direction of the electron drift was instrumented with four embedded J-type thermocouples distributed along its length. During nominal operation at 1500 G and 0.7 A, the thermocouples registered temperatures in excess of 400 °C across the entire channel, with the side wall at around 440 °C.

Figure 6 shows the voltage (V)–current (I) characteristics recorded for both the boron nitride and alumina thruster channel for a range of magnetic field strengths and at a xenon flow rate of 2 sccm. The V – I characteristics for the boron nitride channel are somewhat typical of Hall discharges, with an ‘ionization branch’ at low currents and low magnetic field strengths, and a relatively steep ‘current saturation branch’ at high operating magnetic field strengths and high discharge current. However, these features are less distinct in the case of the alumina channel. In fact, the V – I characteristics do not show an obvious current saturation regime in this latter case. At relatively low magnetic field strengths, the V – I characteristics of the thruster with the alumina channel wall are nearly indistinguishable from that of the same thruster with a boron nitride wall. This is also the case for all magnetic field strengths investigated, at currents below about 0.5 A. Above these current levels, the V – I characteristics for the alumina channel thruster flatten out (note the apparent ‘knee’ in the figure), whereas the boron nitride channel thruster voltage rises sharply.

We speculate that secondary electron emission from the alumina channel is partly responsible for the interesting shape of the V – I characteristics. The possible influence of secondary electron emission in establishing the electron transport in Hall thrusters has been discussed in the prior literature [6, 11]. Alumina has a higher secondary electron emission coefficient than boron nitride [13] and, in addition, we expect that the secondary electron emission is sensitive to wall temperature. It was apparent that during thruster operation with the alumina walls, the wall temperature may have been sufficiently high to significantly enhance secondary electron emission. The higher secondary electron emission for the case of the alumina insulator wall would aid electron transport across the magnetic field. As a result, the thruster could not support as high a voltage as that supported by the thruster with the boron nitride wall. This conjecture would imply that there is a high electron flux (current) along the side wall opposite the direction of the electron Hall current, an argument that is consistent with the observation that the side wall of the boron nitride thruster is found to experience significant erosion. In a recent study by Raitses *et al* [6], it was noted that there were significant differences in the V – I characteristics of a thruster operating with a machinable glass channel and a boron nitride channel. In that study, enhanced axial transport in the thruster with

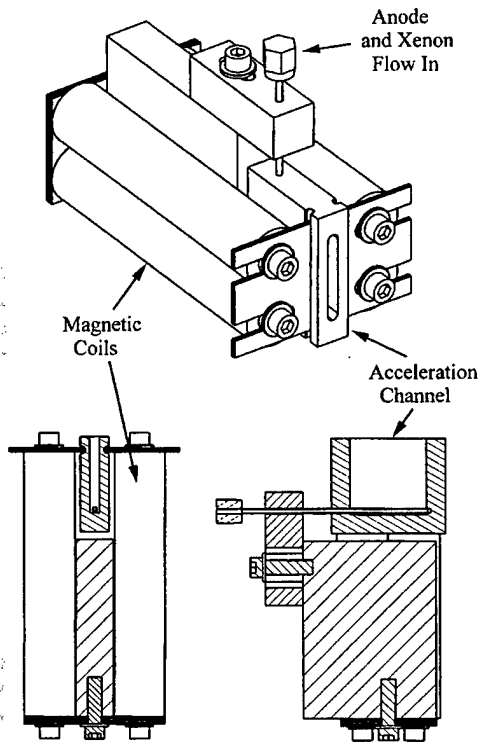


Figure 2. Schematic of the linear-geometry open electron-drift Hall discharge.

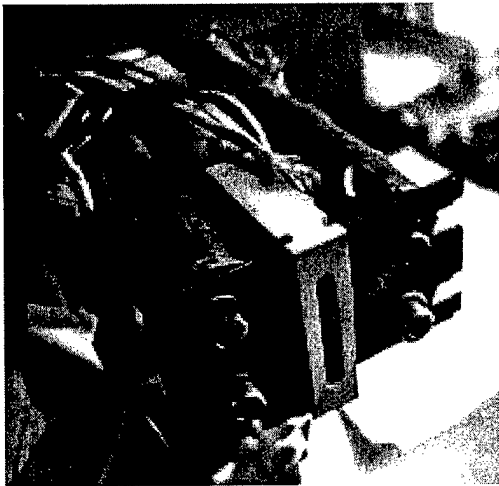


Figure 3. Photograph of the linear-geometry open electron-drift Hall discharge.

insulated copper magnet wire. The magnetic bottom plate is 3 mm thick silicon steel, whereas the magnetic top plate is 1.5 mm thick silicon steel. The discharge channel was fabricated in two versions, one constructed of high-purity alumina ceramic and the other of boron nitride. The anode is a 1.6 mm diameter stainless steel tube with 14 propellant holes, 0.2 mm in diameter spaced by 1.6 mm. A photograph of the thruster is shown in figure 3.

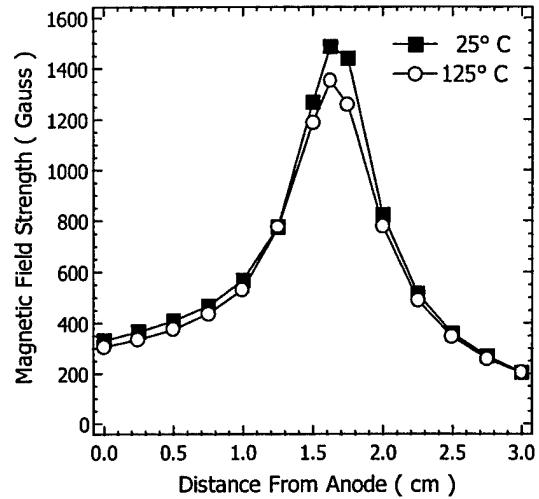


Figure 4. Transverse magnetic field strength variation with axial position. In both cases, the winding current is 1.25 A.

Measurements of the transverse component of the magnetic field show that the magnetic field near the anode is 23% of the peak value, which is located about 2 mm upstream of the channel exit. The measured field distribution for a winding current of 1.25 A is shown in figure 4 for two different temperatures. These measurements were obtained *ex situ*, by heating the entire thruster unit in an oven at ambient conditions while measuring the magnetic field strength. It can be seen that the peak value of 1500 G at room temperature drops to less than 1400 G with a 100 °C temperature rise. This is significant in that the temperature of the acceleration channel has been measured to be as high as 440 °C by embedded thermocouples during operation in the thruster fabricated out of boron nitride.

The cathode used to neutralize the ion beam and support the necessary electric field is an Ion Tech. Inc. HCN-252 hollow cathode. It is capable of supplying a maximum current of 5 A at xenon flow rates of 0.1 to 0.5 mg s⁻¹. It is mounted in front of the thruster such that the hollow cathode exit is 1 cm above the exit of the channel. The cathode is the exact same unit used in the higher power thrusters, and the flow rate used here is comparable to the flow rate through the thruster itself (2 sccm). We expect that the near exit plane xenon density due to the cathode flow will have a negative effect on the discharge performance. However, because the neutral gas density in this low power discharge is about a factor of 5–10 times that in the higher power prototype, the effect is expected to be no greater here than in the higher power version. No attempt at designing and fabricating an appropriately scaled cathode has been made, although the future development of low-power (< 50 W) Hall thrusters will rely on such a development.

The anode of the discharge is powered by a Sorensen SCR600-1.7 laboratory power supply capable of providing 600 V and 1.7 A. The anode also has a 4 Ω resistor in the power line to serve as ballast during initial start of the discharge. The cathode heating element is powered by a low voltage direct-current (DC) power supply capable of providing the 8.5 A required to heat the cathode for startup

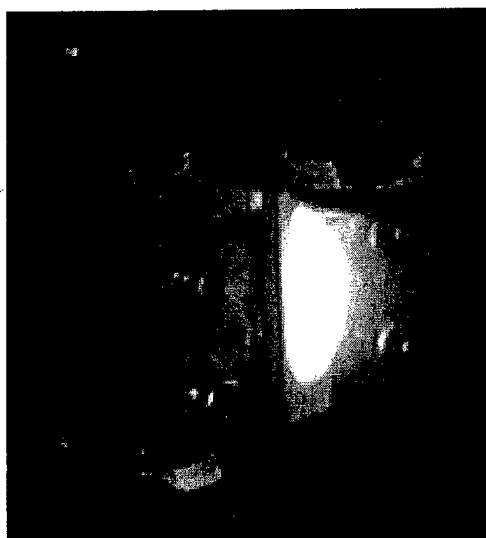


Figure 5. Photograph of the linear-geometry open electron-drift Hall discharge while operating.

and 4.0 A after start. The cathode flow rate of xenon was 2 sccm, a typical value used during operation of our higher power co-axial discharges. The cathode keeper uses a Sorensen SCR300-6 laboratory power supply to provide 250 V for initial cathode start and approximately 10 V and 250 mA during thruster operation. The power required for the magnetic circuit solenoids is provided by a Tektronix PS281 DC power supply operating in current limited mode.

The voltage and current of the thruster were recorded by acquiring data through a National Instruments PCI-5102 data acquisition card plugged into a desktop computer. A voltage divider was used so that the 5 V maximum voltage limit to the card was not exceeded while testing the thruster up to 250 V. The current was monitored by measuring the voltage drop across the 4 Ω ballast resistor.

6. Results and analysis

The thruster described was run at near-design conditions. To start the thruster, a glow discharge was initiated with the magnetic field turned off. With the power supply under current limit control and an upper limit set on the voltage, the magnetic field was increased. The discharge intensity greatly increased and changed colour from dull pink to a bright bluish emission as the magnetic field was increased, which is also typical of coaxial designs. A picture of the thruster running at design conditions is shown in figure 5. The voltage gradually increased until it reached the voltage limit setting. The power supply subsequently switched into voltage control, where most of the data reported was taken.

During operation at magnetic fields above 600 G, it was noted that the discharge was slightly asymmetric, being more intense near the side end of the channel in direction of the $E \times B$ electron drift. It was especially apparent during operation of the alumina thruster that this end wall became extremely hot and glowed intensely. This glow was contrasted to the bulk of the thruster channel, which did not show this intense

heating. On one occasion, after a few minutes of running the alumina thruster, the acceleration channel cracked along the edge of the glowing area. This failure was probably due to a high thermal stress caused by extreme temperature gradients in this region of the channel wall. Operation with the boron nitride thruster did not result in such a non-uniform temperature field on the insulating wall. This difference between the boron nitride and alumina insulators is attributed to the difference in the thermal conductivity values of the materials. The boron nitride channel end wall in the direction of the electron drift was instrumented with four embedded J-type thermocouples distributed along its length. During nominal operation at 1500 G and 0.7 A, the thermocouples registered temperatures in excess of 400 °C across the entire channel, with the side wall at around 440 °C.

Figure 6 shows the voltage (V)–current (I) characteristics recorded for both the boron nitride and alumina thruster channel for a range of magnetic field strengths and at a xenon flow rate of 2 sccm. The V – I characteristics for the boron nitride channel are somewhat typical of Hall discharges, with an ‘ionization branch’ at low currents and low magnetic field strengths, and a relatively steep ‘current saturation branch’ at high operating magnetic field strengths and high discharge current. However, these features are less distinct in the case of the alumina channel. In fact, the V – I characteristics do not show an obvious current saturation regime in this latter case. At relatively low magnetic field strengths, the V – I characteristics of the thruster with the alumina channel wall are nearly indistinguishable from that of the same thruster with a boron nitride wall. This is also the case for all magnetic field strengths investigated, at currents below about 0.5 A. Above these current levels, the V – I characteristics for the alumina channel thruster flatten out (note the apparent ‘knee’ in the figure), whereas the boron nitride channel thruster voltage rises sharply.

We speculate that secondary electron emission from the alumina channel is partly responsible for the interesting shape of the V – I characteristics. The possible influence of secondary electron emission in establishing the electron transport in Hall thrusters has been discussed in the prior literature [6, 11]. Alumina has a higher secondary electron emission coefficient than boron nitride [13] and, in addition, we expect that the secondary electron emission is sensitive to wall temperature. It was apparent that during thruster operation with the alumina walls, the wall temperature may have been sufficiently high to significantly enhance secondary electron emission. The higher secondary electron emission for the case of the alumina insulator wall would aid electron transport across the magnetic field. As a result, the thruster could not support as high a voltage as that supported by the thruster with the boron nitride wall. This conjecture would imply that there is a high electron flux (current) along the side wall opposite the direction of the electron Hall current, an argument that is consistent with the observation that the side wall of the boron nitride thruster is found to experience significant erosion. In a recent study by Raitses *et al* [6], it was noted that there were significant differences in the V – I characteristics of a thruster operating with a machinable glass channel and a boron nitride channel. In that study, enhanced axial transport in the thruster with

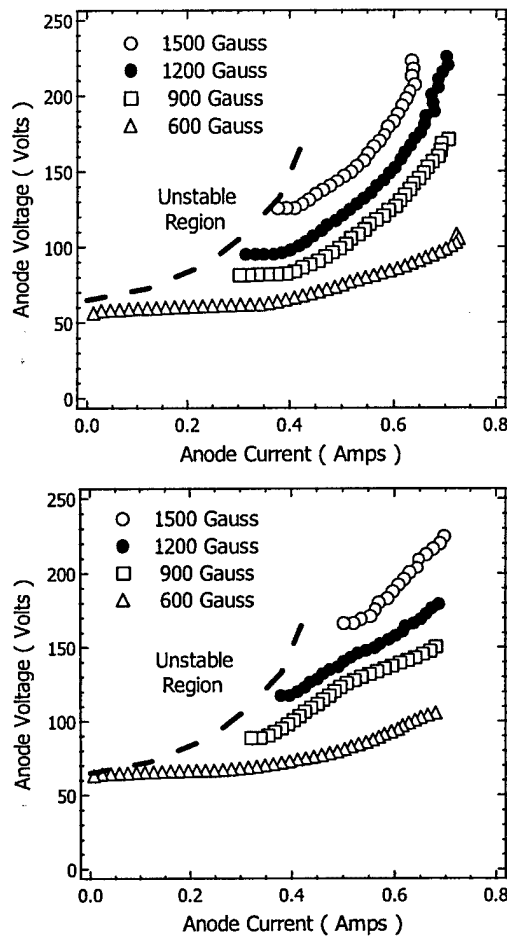


Figure 6. Discharge voltage-current characteristics of the linear-geometry Hall discharge (top) boron nitride channel, (bottom) alumina channel.

the machinable glass channel was attributed to wall effects, decreasing the thruster efficiency at high operating voltages. The qualitative findings reported on in this study agree with these past observations. It is also noteworthy that the conjecture that there is an enhanced electron current due to wall collisions is supported by the relatively poor efficiency of this discharge, as an upper limit of the ratio of the ion current to electron current is no more than 30%, based on full utilization (ionization) of the propellant.

In all cases, the thrusters exhibited a region of unstable operation. At all magnetic field strengths except the lowest value shown, the discharge had a low current limit in its operating envelope. Attempts to operate or start the discharge in this region would fail. We speculate that this region of instability is closely tied to the requirement for enhanced electron transport and that, at low currents and high magnetic fields, the anomalous transport process cannot provide the necessary current to maintain the discharge.

The fact that the thruster ran without a mechanism for closing the Hall current confirms the importance of an electron transport process that is due to plasma fluctuations and/or wall effects associated with secondary electron

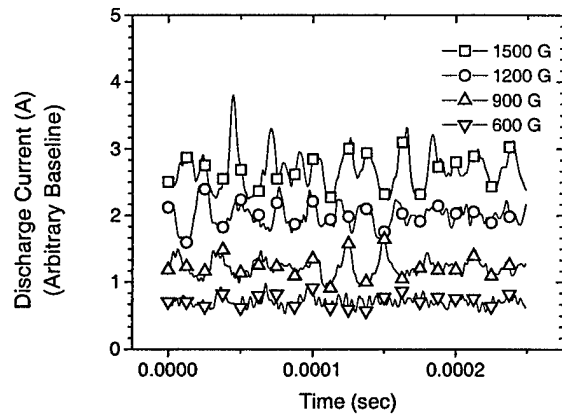


Figure 7. Time-variation in discharge current for the alumina-walled plasma source at a range of peak magnetic field conditions.

emission. As in the higher power co-axial discharges, the linear discharge studied here also exhibited plasma fluctuations, which were detected as fluctuations in the external circuit discharge current.

Figure 7 shows the oscillations in the discharge current of the linear thruster operating with the alumina channel wall for a range of peak magnetic field strengths and at a discharge current of 0.7 A. The fluctuations in the discharge current for the boron nitride wall were qualitatively similar. It is apparent that at low magnetic fields, there is a relatively low frequency oscillation, on which higher frequencies are superimposed. The low frequency oscillation increases in amplitude and in frequency as the magnetic field is increased. These intense low frequencies observed in this linear device are similar to those seen in co-axial devices, and are believed to be the so-called 'breathing' mode of oscillation associated with the neutral xenon transit through the ionization zone [14]. This instability is associated with the disturbance in the balance established between the depletion of neutrals in the channel as a result of ionization, and their replenishment. Since the length of the ionization zone in this low-power Hall discharge is scaled to be some 5–10 times shorter than that of our reference thruster, the frequencies of these disturbances are expected to be at least a factor of five higher than those seen in our higher power co-axial devices.

Figure 8 compares the Fourier analysis of the temporal fluctuations in discharge current of the reference 400 W (200 V, 20 sccm, 160 G, 2 A) co-axial thruster and the low-power linear thruster operating with the alumina channel wall (data shown in figure 7). It is apparent that the low-power thruster has a strong low-frequency mode, similar to that seen in the co-axial high-power devices, at frequencies that are approximately a factor of four times that of the higher power thruster. As the magnetic field is increased the frequency of the fluctuations in the anode current also increase, until a magnetic field strength of 900 G, beyond which it remains constant. This result is seemingly inconsistent with the theoretical predictions of Boeuf and Garrigues [14]. However, a direct comparison to the results in [14] is difficult to make, since in our studies, the current is held constant while the magnetic field is increased (resulting

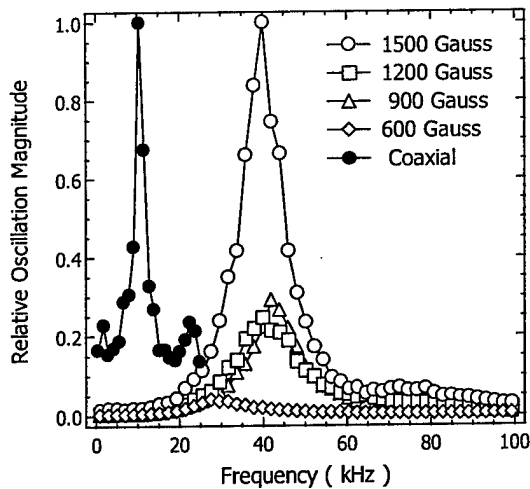


Figure 8. Low-frequency spectral analysis of the temporal fluctuations in the discharge current. Included in the figure is the spectral distribution of the fluctuations seen in the higher power co-axial discharge for comparison.

in increased discharge voltages). In the calculations of Boeuf and Garrigues, the voltage was varied at constant magnetic field (giving rise to varying current) and/or the magnetic field was varied at constant voltage. As discussed in [14], the frequency of this mode is seen to increase dramatically with voltage (at constant magnetic field). The response that we see is therefore likely to be a result of the response in the frequency to changes in both the voltage and the magnetic field.

It is interesting to note that at the highest magnetic field studied, there is a superimposed high-frequency oscillation at about 80 kHz. Through particle simulations, Boeuf and Garrigues [14] also discovered the presence of strong disturbances in the plasma density and electric field upstream near the anode when the magnetic field continues to persist near the anode. The weak intensities seen here at the highest magnetic field studied may be a consequence of these near-anode instabilities, although a precise characterization of these instabilities in a linear geometry must still be performed. In a related study, we have identified the presence of near-anode instabilities in this frequency range (40–100 kHz) in co-axial Hall discharges [15].

7. Summary

An analysis and arguments for the scaling of a Hall plasma thruster to low powers was presented. A linear-geometry version of a thruster operating in the 50–100 W power range has been fabricated and operated at near-design conditions. Preliminary results obtained so far indicate that at the scaled power levels, these low power plasma discharges operate at much higher channel wall temperatures. This increased heat flux may be a major impediment to the extended operation of very low power devices.

The linear Hall plasma thruster reported on here is found to have the characteristic discharge instabilities seen in higher power co-axial versions. Although we have not performed an

extensive analysis of the thruster performance, it does appear that the linear device behaves in many ways similarly to those of a co-axial design with a closed electron drift. Since the linear discharge operates without a closed Hall current, it suggests that there must be an anomalous mechanism for cross-field electron transport.

This device might prove most useful for investigating various materials for use as acceleration channels in Hall thrusters. The linear-geometry design allows easy fabrication from a variety of materials. A study of the operating characteristics of thrusters constructed with insulating walls fabricated from a wide variety of materials would be useful for understanding the effect of secondary electron emission on electron transport.

Acknowledgments

This work was supported by the Air Force Office of Scientific Research, with Dr Mitat Birkan as the contract monitor.

References

- [1] Brown C O and Pinsley E A 1965 *AIAA J.* **3** 853
- [2] Janes G S and Lowder R S 1966 *Phys. Fluids* **9** 1115
- [3] Gulczynski F S and Spores R A 1996 Analysis of Hall-effect thrusters and ion engines for orbit transfer missions *32nd Joint Propulsion Conference (1996, Lake Buena Vista, FL)* AIAA-96-2973
- [4] Bohm D 1949 *The Characteristics of Electrical Discharges in Magnetic Fields* ed A Guthrie and R K Wakerling (New York: McGraw Hill)
- [5] Chen F F 1985 *Plasma Physics and Controlled Fusion* 2nd edn (New York: Plenum) p 193
- [6] Raites Y, Ashkenazy J, Appelbaum G and Guelman M 1997 Experimental investigation of the effect of channel material on Hall thruster characteristics *25th International Electric Propulsion Conference (1997, Cleveland, OH)* IEPC 97-056
- [7] Khayms V and Martinez-Sanchez M 1996 Design of a miniaturized Hall thruster for microsatellites *32nd Joint Propulsion Conference (1996, Lake Buena Vista, FL)* AIAA-96-3291
- [8] Hargus W A Jr and Cappelli M A 1998 Development of a linear Hall thruster *34th Joint Propulsion Conference (1998, Cleveland, OH)* AIAA 98-3336
- [9] Meezan N B, Hargus W A Jr and Cappelli M A 1998 Optical and electrostatic characterization of oscillatory Hall discharge behavior *34th Joint Propulsion Conference (1998, Cleveland, OH)* AIAA-98-3502
- [10] Hargus W A Jr, Meezan N B and Cappelli M A 1997 Transient behavior of a low-power laser Hall thruster *33rd Joint Propulsion Conference (1997, Seattle, WA)* AIAA-97-3050
- [11] Fife J M, Martinez-Sanchez M and Szabo J J 1997 Numerical study of low frequency discharge oscillations in Hall thrusters *33rd Joint Propulsion Conference (1997, Seattle, WA)* AIAA-97-3052
- [12] Hargus W A Jr and Cappelli M A 1998 Laser induced fluorescence measurements on a laboratory Hall thruster *34th Joint Propulsion Conference (1998, Cleveland, OH)* AIAA 98-3645
- [13] Dawson P H 1978 *J. Appl. Phys.* **37** 3644
- [14] Boeuf J P and Garrigues L 1999 *J. Appl. Phys.* **84** 3541
- [15] Meezan N B and Cappelli M A 1999 Optical emission study of anomalous electron transport in a laboratory Hall thruster *35th Joint Propulsion Conference (1999, Los Angeles, CA)* AIAA 99-2284

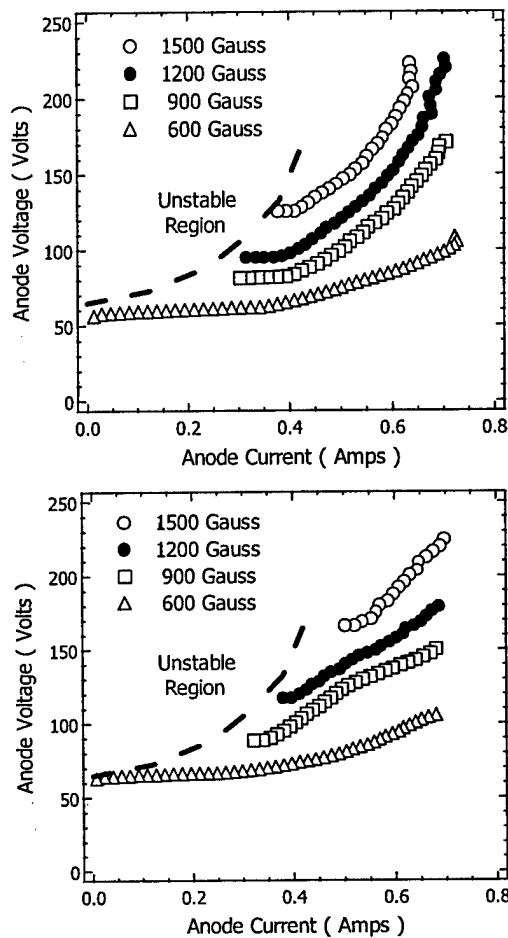


Figure 6. Discharge voltage-current characteristics of the linear-geometry Hall discharge (top) boron nitride channel, (bottom) alumina channel.

the machinable glass channel was attributed to wall effects, decreasing the thruster efficiency at high operating voltages. The qualitative findings reported on in this study agree with these past observations. It is also noteworthy that the conjecture that there is an enhanced electron current due to wall collisions is supported by the relatively poor efficiency of this discharge, as an upper limit of the ratio of the ion current to electron current is no more than 30%, based on full utilization (ionization) of the propellant.

In all cases, the thrusters exhibited a region of unstable operation. At all magnetic field strengths except the lowest value shown, the discharge had a low current limit in its operating envelope. Attempts to operate or start the discharge in this region would fail. We speculate that this region of instability is closely tied to the requirement for enhanced electron transport and that, at low currents and high magnetic fields, the anomalous transport process cannot provide the necessary current to maintain the discharge.

The fact that the thruster ran without a mechanism for closing the Hall current confirms the importance of an electron transport process that is due to plasma fluctuations and/or wall effects associated with secondary electron

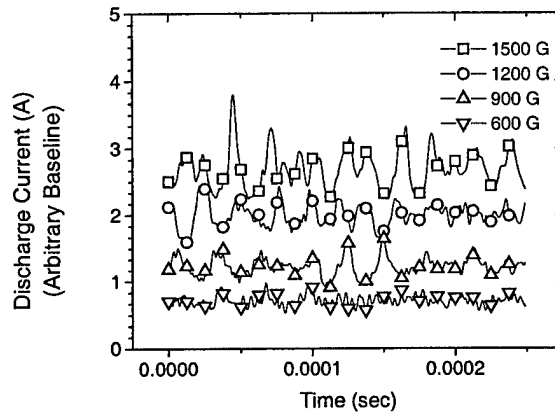


Figure 7. Time-variation in discharge current for the alumina-walled plasma source at a range of peak magnetic field conditions.

emission. As in the higher power co-axial discharges, the linear discharge studied here also exhibited plasma fluctuations, which were detected as fluctuations in the external circuit discharge current.

Figure 7 shows the oscillations in the discharge current of the linear thruster operating with the alumina channel wall for a range of peak magnetic field strengths and at a discharge current of 0.7 A. The fluctuations in the discharge current for the boron nitride wall were qualitatively similar. It is apparent that at low magnetic fields, there is a relatively low frequency oscillation, on which higher frequencies are superimposed. The low frequency oscillation increases in amplitude and frequency as the magnetic field is increased. These intense low frequencies observed in this linear device are similar to those seen in co-axial devices, and are believed to be the so-called 'breathing' mode of oscillation associated with the neutral xenon transit through the ionization zone [14]. This instability is associated with the disturbance in the balance established between the depletion of neutrals in the channel as a result of ionization, and their replenishment. Since the length of the ionization zone in this low-power Hall discharge is scaled to be some 5–10 times shorter than that of our reference thruster, the frequencies of these disturbances are expected to be at least a factor of five higher than those seen in our higher power co-axial devices.

Figure 8 compares the Fourier analysis of the temporal fluctuations in discharge current of the reference 400 W (200 V, 20 sccm, 160 G, 2 A) co-axial thruster and the low-power linear thruster operating with the alumina channel wall (data shown in figure 7). It is apparent that the low-power thruster has a strong low-frequency mode, similar to that seen in the co-axial high-power devices, at frequencies that are approximately a factor of four times that of the higher power thruster. As the magnetic field is increased the frequency of the fluctuations in the anode current also increase, until a magnetic field strength of 900 G, beyond which it remains constant. This result is seemingly inconsistent with the theoretical predictions of Boeuf and Garrigues [14]. However, a direct comparison to the results in [14] is difficult to make, since in our studies, the current is held constant while the magnetic field is increased (resulting

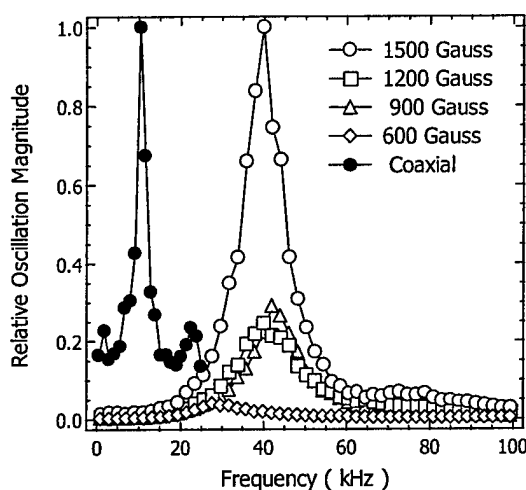


Figure 8. Low-frequency spectral analysis of the temporal fluctuations in the discharge current. Included in the figure is the spectral distribution of the fluctuations seen in the higher power co-axial discharge for comparison.

in increased discharge voltages). In the calculations of Boeuf and Garrigues, the voltage was varied at constant magnetic field (giving rise to varying current) and/or the magnetic field was varied at constant voltage. As discussed in [14], the frequency of this mode is seen to increase dramatically with voltage (at constant magnetic field). The response that we see is therefore likely to be a result of the response in the frequency to changes in both the voltage and the magnetic field.

It is interesting to note that at the highest magnetic field studied, there is a superimposed high-frequency oscillation at about 80 kHz. Through particle simulations, Boeuf and Garrigues [14] also discovered the presence of strong disturbances in the plasma density and electric field upstream near the anode when the magnetic field continues to persist near the anode. The weak intensities seen here at the highest magnetic field studied may be a consequence of these near-anode instabilities, although a precise characterization of these instabilities in a linear geometry must still be performed. In a related study, we have identified the presence of near-anode instabilities in this frequency range (40–100 kHz) in co-axial Hall discharges [15].

7. Summary

An analysis and arguments for the scaling of a Hall plasma thruster to low powers was presented. A linear-geometry version of a thruster operating in the 50–100 W power range has been fabricated and operated at near-design conditions. Preliminary results obtained so far indicate that at the scaled power levels, these low power plasma discharges operate at much higher channel wall temperatures. This increased heat flux may be a major impediment to the extended operation of very low power devices.

The linear Hall plasma thruster reported on here is found to have the characteristic discharge instabilities seen in higher power co-axial versions. Although we have not performed an

extensive analysis of the thruster performance, it does appear that the linear device behaves in many ways similarly to those of a co-axial design with a closed electron drift. Since the linear discharge operates without a closed Hall current, it suggests that there must be an anomalous mechanism for cross-field electron transport.

This device might prove most useful for investigating various materials for use as acceleration channels in Hall thrusters. The linear-geometry design allows easy fabrication from a variety of materials. A study of the operating characteristics of thrusters constructed with insulating walls fabricated from a wide variety of materials would be useful for understanding the effect of secondary electron emission on electron transport.

Acknowledgments

This work was supported by the Air Force Office of Scientific Research, with Dr Mitat Birkan as the contract monitor.

References

- [1] Brown C O and Pinsley E A 1965 *AIAA J.* **3** 853
- [2] Janes G S and Lowder R S 1966 *Phys. Fluids* **9** 1115
- [3] Gulczynski F S and Spores R A 1996 Analysis of Hall-effect thrusters and ion engines for orbit transfer missions 32nd Joint Propulsion Conference (1996, Lake Buena Vista, FL) AIAA-96-2973
- [4] Bohm D 1949 *The Characteristics of Electrical Discharges in Magnetic Fields* ed A Guthrie and R K Wakerling (New York: McGraw Hill)
- [5] Chen F F 1985 *Plasma Physics and Controlled Fusion* 2nd edn (New York: Plenum) p 193
- [6] Raitses Y, Ashkenazy J, Appelbaum G and Guelman M 1997 Experimental investigation of the effect of channel material on Hall thruster characteristics 25th International Electric Propulsion Conference (1997, Cleveland, OH) IEPC 97-056
- [7] Khayms V and Martinez-Sanchez M 1996 Design of a miniaturized Hall thruster for microsatellites 32nd Joint Propulsion Conference (1996, Lake Buena Vista, FL) AIAA-96-3291
- [8] Hargus W A Jr and Cappelli M A 1998 Development of a linear Hall thruster 34th Joint Propulsion Conference (1998, Cleveland, OH) AIAA 98-3336
- [9] Meezan N B, Hargus W A Jr and Cappelli M A 1998 Optical and electrostatic characterization of oscillatory Hall discharge behavior 34th Joint Propulsion Conference (1998, Cleveland, OH) AIAA-98-3502
- [10] Hargus W A Jr, Meezan N B and Cappelli M A 1997 Transient behavior of a low-power laser Hall thruster 33rd Joint Propulsion Conference (1997, Seattle, WA) AIAA-97-3050
- [11] Fife J M, Martinez-Sanchez M and Szabo J J 1997 Numerical study of low frequency discharge oscillations in Hall thrusters 33rd Joint Propulsion Conference (1997, Seattle, WA) AIAA-97-3052
- [12] Hargus W A Jr and Cappelli M A 1998 Laser induced fluorescence measurements on a laboratory Hall thruster 34th Joint Propulsion Conference (1998, Cleveland, OH) AIAA 98-3645
- [13] Dawson P H 1978 *J. Appl. Phys.* **37** 3644
- [14] Boeuf J P and Garrigues L 1999 *J. Appl. Phys.* **84** 3541
- [15] Meezan N B and Cappelli M A 1999 Optical emission study of anomalous electron transport in a laboratory Hall thruster 35th Joint Propulsion Conference (1999, Los Angeles, CA) AIAA 99-2284